POLITECNICO DI TORINO

Master's Degree in Biomedical Engineering

Master's Degree Thesis

Spatio-Temporal Analysis During Running Using Magneto-Inertial Sensors: Optimization of Foot Orientation Estimation

Supervisors

Prof. Ing. Andrea CEREATTI

Ing. Rachele ROSSANIGO

Ing. Marco CARUSO

Candidate

Alessia MACHETTI

March 2025

A Edo. Ti porto con me ogni giorno.

Acknowledgements

Alla fine di questo intenso e stimolante percorso, desidero esprimere la mia sincera gratitudine al Professor Andrea Cereatti per avermi dato l'opportunità di intraprendere questo progetto di tesi e per avermi trasmesso la passione per i sensori inerziali applicati all'analisi del movimento.
Un ringraziamento speciale va all'Ing. Rachele Rossanigo, il cui supporto costante in questi undici mesi è stato fondamentale per il raggiungimento di questo importante traguardo.
Desidero inoltre ringraziare l'Ing. Marco Caruso per le preziose conoscenze condivise lungo il percorso.
Un pensiero ai colleghi conosciuti durante questo progetto: la vostra compagnia ha reso questa esperienza ancora più piacevole.

Infine, desidero dedicare qualche parola a tutte le persone che mi sono state vicine in questi anni. Chi mi conosce bene sa quanto io sia scarsa nel dimostrare affetto, quindi non aspettatevi nulla di che.
Un pensiero speciale va a Mamma e Papà, che non solo mi hanno permesso di vivere questa straordinaria esperienza, ma soprattutto mi hanno sempre spronata a non arrendermi e a dare il massimo, anche nei momenti più difficili, quando tutto sembrava insormontabile.
Ad Alessandra, che ogni giorno mi dimostra che non serve un legame di sangue per sentire il significato di famiglia.
Ai miei Amici di sempre, ai miei Nonni, ai Merenderos e a tutte le persone che ho conosciuto grazie alla montagna, ai miei amici del Poli, ai ragazzi conosciuti in collegio e alle mie coinquiline, grazie di tutto, non potrei essere più felice di avervi tutti insieme nella mia vita.
In ultimo, vorrei cogliere l'occasione per ringraziare Gabri, per tutto quello che ha fatto per me in questi due anni di magistrale. Qualunque strada prenderanno le nostre vite, non potrei essere più felice di averti accanto.

Abstract

Running is a widely practiced activity providing significant health benefits but also potential injury risks. A thorough biomechanical analysis is essential for optimizing performance and preventing running-related injuries. In running characterization, stride length (SL) and stride velocity (SV) are key running spatio-temporal parameters quantifying foot displacement and velocity within a stride. These parameters can be assessed in indoor and outdoor conditions by wearable magneto-inertial measurement units (MIMUs) through the adoption of ad-hoc algorithms. The most direct approach to estimate spatial-related parameters is to double integrate foot accelerations after gravity removal. Effective gravity removal requires to accurately estimate the foot orientation which can be determined through a sensor fusion algorithm (SFA) using (magneto-)inertial signals. However, to work well, these algorithms require extensive fine-tuning of different parameters and often lack robustness to variations in highly dynamic movements like running.

In this thesis, a comprehensive analysis of four different SFAs was conducted to assess their impact on SL and SV estimation and their robustness to changes in their main parameters and in running speed. Then, a novel framework for the automatic stride-by-stride setting of SFA parameters was proposed to handle different running conditions and speeds. The proposed method minimized a cost function based on errors on SL and SV estimates with respect to an available reference, imposing biomechanical constraints and measurement consistency.

A total of 20 participants were enrolled to build two datasets at different speeds. The first dataset included both treadmill and overground running at 8-10 km/h with pressure insoles used as reference, while the second one included treadmill running at 14km/h with a stereo-photogrammetric system used as reference.

The parameter setting of each SFA was speed-dependent. Thus, each SFA was fine-tuned to select a fixed optimal value of its parameter(s) minimizing SL errors across speeds. The best performance was achieved by the SFA proposed by Madgwick et

al. (2011), which resulted in SL errors of 1.6% and 2.5%, and SV errors of 3.5% and 2.6% at 8-10 km/h and 14 km/h, respectively. The proposed framework for stride-by-stride selection of Madgwick's parameter provided better or comparable results with the previous approach using a fixed Madgwick's parameter (SL error of 0.9% and 1.5%, and SV error of 0.3% and 0.2% at 8-10 km/h and 14 km/h, respectively). This study demonstrated that using a SFA with a fixed optimized parameter can provide accurate SL and SV estimates. However, the setting of SFA parameters can be speed-dependent and usually influenced by the specific characteristics of the used inertial sensors. Conversely, the proposed framework is a promising solution to automatically adjust SFA parameters regardless of speed, hardware, and running conditions, being suitable for running analysis in different and variable scenarios.

Contents

List of Figures

List of Tables

Nomenclature

Acronyms / Abbreviations

AP Antero-Posterior

ARW Angle Random Walk

CF Complementary Filter

DCM Direction Cosine Matrix

DRI Direct Reverse Integration

EKF Extended Kalman Filter

FC Final Contact

GCS Global Coordinate System

GRF Ground Reaction Force

GUO Guo Kalman Filter

HPF High Pass Filter

IC Initial Contact

KF Kalman Filter

LCS Local Coordinate System

LKF Linear Kalman Filter

LPF Low Pass Filter

MAD Madgwick Complementary Filter

MEMS Micro-Electro-Mechanical System

MIMU Magneto-Inertial Measurement Unit

ML Medio-Lateral

MS Mid-Stance

PA Physical Activity

PI Pressure Insoles

SEL Seel Complementary Filter

SFA Sensor Fusion Algorithm

SL Stride Length

SP Stereophotogrammetry

SQP Sequential Quadratic Programming

SV Stride Velocity

TB Templete-Based

VAC Valenti Complementary Filter

V Vertical

ZUPT Zero Velocity Update

Chapter 1

Introduction

1.1 Relevance and General Introduction

Running is a widely practiced sport across different levels, with many people today choosing it as a leisure-time physical activity (PA). This popularity stems from several factors, such as the perceived simplicity of the technical movement and the relatively low initial financial investment it requires. Running offers numerous health benefits for its practitioners [20]:

- it aids in the prevention of chronic illnesses, including type II diabetes, osteoarthritis, obesity, respiratory diseases and certain cancers.
- it can enhance the quality of life for individuals suffering from depression, anxiety and dementia.
- it promotes better sleep quality and helps to alleviate stress.

Although often hailed as a "cost-effective lifestyle medicine from a public health perspective" [20], it is important to note that this PA is not without risks [21].
Furthermore, running is not solely an independent athletic discipline; it also serves as a core component of various dynamic sports, such as soccer, basketball, volleyball, softball, baseball, and rugby [22].
The biomechanical characterization of running is crucial for preventing sport-specific injuries and enhancing performance not only for elite and amateur runners but also for athletes in other sports where running plays a central role.

1.1.1 Biomechanical Analysis of Running

Running is characterized by a cyclic nature and differs from walking because it involves higher velocities, higher Ground Reaction Forces (GRFs) and a "flight phase", in which both feet are off the ground [23]. While running, our bodies combine different actions, both articular and muscular; most of running biomechanics, in fact, is dictated by lower limb anatomy [1]. Pronation and supination are essential triplanar movements that involve the foot and ankle, resulting in obligate motion. Pronation is a combination of ankle dorsiflexion, subtalar eversion, and forefoot abduction, while supination refers to the coordination of the following joint movements: ankle plantarflexion, subtalar inversion, and forefoot adduction. Figure 1.1 illustrates the anatomy and rotations involved in these movements. The ligaments of the foot provide passive stability, while the muscles of the lower leg and foot work both in a concentric and eccentric fashion. An eccentric contraction happens when the fibers lengthen, a concentric one happens when fibers are shortening.

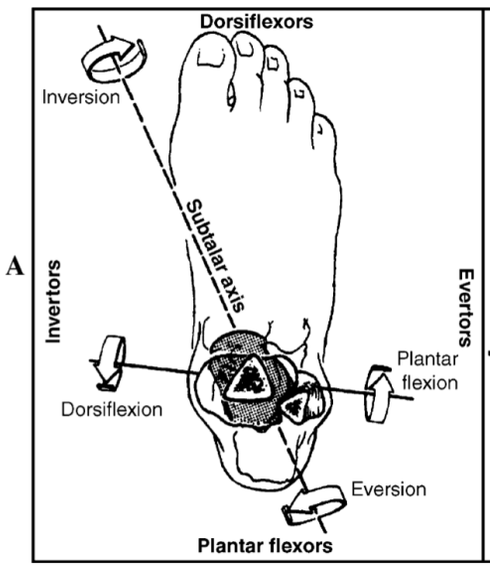

Fig. 1.1 Ankle and subtalar joint axes rotation, from [1].

The running gait can be divided into two main phases (as shown in figure 1.2), each characterized by certain key events:

- **Stance**: this phase determines the 40% of the running cycle and is characterized by an *Initial Contact* (IC), where the relevant foot contacts the ground; a

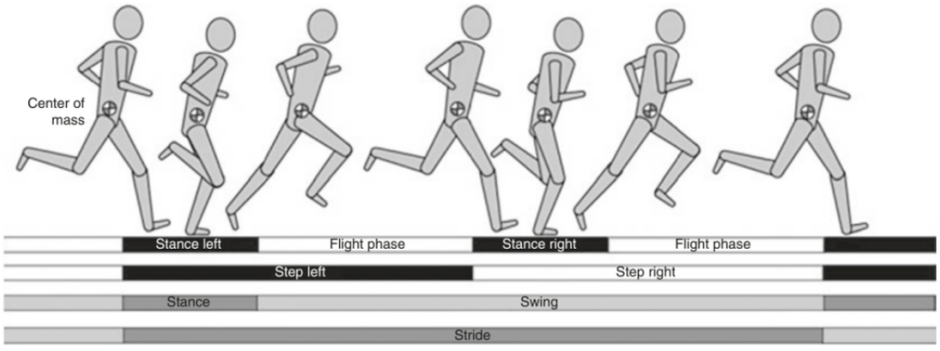

Fig. 1.2 Different phases of running gait cycle, from [2].

Mid Stance (MS); and a *Final Contact* (FC), or propulsion phase, where the body is pushed forward by the hip, knee, and ankle in full extension.

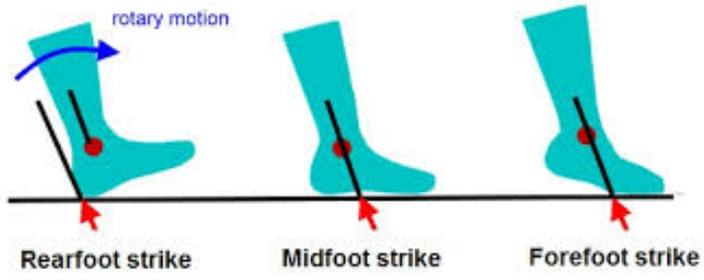

Fig. 1.3 Rear-, mid- and fore-foot strikes expamples, from [3].

- The **IC** represents 15-20% of the stance phase. As the relevant foot strikes the ground in a supinated position [24], the body experiences vertical deceleration. At this point, significant muscular contributions are required to control the effects of the ground reaction forces. The hip and knee begin the stance by extending, while the quadriceps lengthen; meanwhile, the upper limbs counterbalance the movement of the lower limbs, using the arms to rotate.
- **MS**: in this subphase (60 % of the stance), the body moves past the supporting leg. At this point, the ankle and knee reach maximum flexion while the quadriceps continue to lengthen, and the upper body maintains rotational movement. The foot is in maximum pronation, typically transitioning from rearfoot to forefoot support. Statistics indicate that approximately 80 % of long-distance runners are rearfoot strikers, while

the remaining 20 % are forefoot strikers [25]. Furthermore, it's important to note that as speed increases (such as in sprinting), runners tend to adopt a forefoot strike to propel the body forward as quickly as possible. In figure 1.3, different types of foot strikes that can occur during the running movement are shown. A rearfoot strike reduces the load on the Achilles tendon, altering the direction of the Ground Reaction Force (GRF) but increases the load on the anterior tibialis muscle. On the other hand, a forefoot strike reduces the load on the anterior tibialis but increases it on the Achilles tendon and calf.

  - **FC** culminates in propulsion and represents the last 20 % of the stance phase. Here, the hip, knee, and ankle are at maximum extension, in order to push the body forward. The upper body assists in propulsion by moving one arm forward and the other backward, in opposition to the legs.

- **Swing**: it determines 60 % of the running cycle (unlike walking, where the duration of stance and swing phases are opposite) and is characterized by the foot being off the ground. Here, the hip rapidly flexes and swings the leg back to the same position as at the start of the cycle. Meanwhile, the upper body rotates in the opposite direction in preparation for the next contact phase.

To summarize, it is important to emphasize that, as speed increases, the duration of the stance phase decreases even further, reaching a minimum of 22 % in elite sprinters [25]. Furthermore, there are other factors that affect stride and swing durations, such as individual characteristics and the environment in which a runner trains, including terrain type and surface hardness.
There are several metrics that can be used to assess running performance or detect certain patterns that can be corrected to help prevent injuries. These parameters provide insights within either the temporal or spatial domain.
The temporal parameters used are:

- *Stride Duration* [s], which is the time interval between two consecutive ICs of opposite feet.

- *Step Duration* [s], which is the time interval between two consecutive ICs of the same foot.

- *Cadence* [$\frac{\text{steps}}{\text{min}}$], which is the number of steps per unit of time.

While the spatial ones are:

- *Stride Length* [m], which represents the distance between two consecutive ground ICs of the same foot.
- *Step Length* [m], defined as the distance between the IC points of two consecutive steps made by opposite feet.
- *Step Width* [m], also known as base width, is defined as the perpendicular distance from the direction of gait between the IC points of two consecutive steps made by opposite feet. While running, stride width is reduced compared to walking because this is more energetically efficient. A large stride width results in higher energy costs, while a reduced one can increase hip tension; therefore, a physiological compromise should be sought to optimize movement [20].

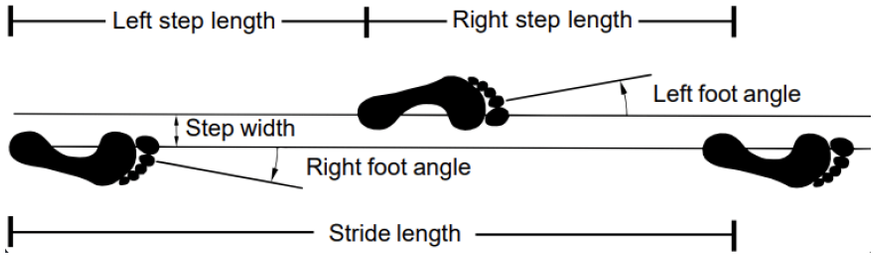

Fig. 1.4 Diagram showing the spatial parameters of interest, from [4].

All the aforementioned spatial parameters are described in figure 1.4.

1.1.2 Instrumentation for Running Analysis

The biomechanical analysis of the running gait can be performed using various technologies, depending on the needs and the means available for data acquisition. Generally, this gesture is often analyzed through clinical observations or with the help of specific rating scales, which provide objective information but may not be sensitive to changes in a subject's running performance due to injury or improvements from training. Some of these evaluation scales include the "High-Level Mobility" and

"Assessment Tool" [26]. Another method used for quantitative analysis of running involves two-dimensional cameras, which allow for determining specific patterns of the subject but remain highly dependent on the clinician analyzing the video [26]. However, to obtain and analyze more complex and objective metrics, such as spatio-temporal, kinematic, and kinetic parameters, it is necessary to rely on more advanced and expensive tools, often exclusively intended for laboratory use. The most popular instrumentation used is **Optoelectronic Motion Capture Systems**, **Force Plates** and **Instrumented Treadmills**.

Optoelectronic Motion Capture Systems

Human motion capture refers to the ability to record human movements [27]. In this field, optoelectronic systems represent the gold standard due to their high accuracy in motion estimation. These systems rely on calibrated cameras that record the movements of interest and allow for the collection of data that, when processed, provide valuable insights into specific spatio-temporal parameters of human motion. Optoelectronic motion capture is inherently **marker-based**, as it relies on the detection of markers placed on the subject's body. These markers can be either active (equipped with LEDs that emit light) or passive (made of reflective material). Their presence enhances contrast in the camera-captured images, enabling specific algorithms to precisely determine their spatial position and subsequently derive the subject's kinematics. A marker-based optoelectronic system is commonly referred to as optical stereophotogrammetry (SP) in the field of human motion analysis [28].

Markerless Motion Capture Systems

Alternatively, there are systems that enable motion analysis using cameras without requiring markers on the subject. **markerless** methods are often based on normal video recordings and on deep-learning techniques (such as pose estimation algorithms) to determine the subject orientation in space. These tools are promising because they do not need markers, reducing the time required for experimental setup, and facilitating their application both indoors and outdoors.

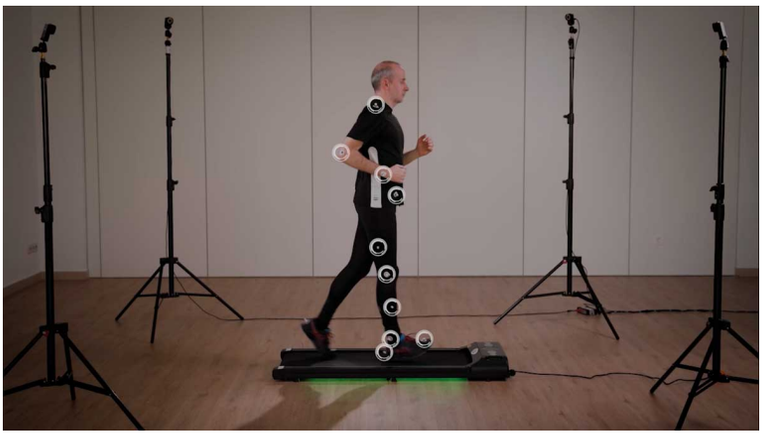

Fig. 1.5 Example of a marker-based optoelectronical motion capture system, from [5].

Force Plates

Force platforms are mechanical sensing systems, used to measure GRFs and moments. These instruments are useful to characterize biomechanical processes, such as walking, running or jumping [6]. Force plates are equipped with load cells, which can contain strain gauge, piezoelectric elements or beam load cells. The working principle is simple: when a force is applied, the sensor undergoes mechanical deformation, followed by a polarization, proportional to the applied force. Several sensors can be placed in different orientations, enabling to obtain a tri-axial force plate: this configuration allow for determining the centre of pressure, centre of force and the moments around the vertical, horizontal and transverse axes.

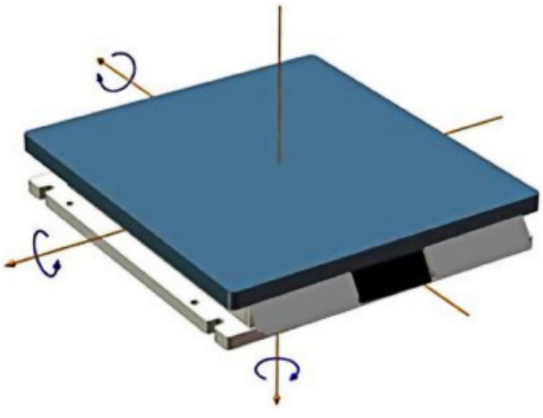

Fig. 1.6 Representative tri-axial force plate system, from [6].

Instrumented Treadmills

Instrumented mats are increasingly common in clinical gait and running analysis, as they enable repeatable measurements of gait cycles in confined spaces. These measurements are achieved through integrated force plates and various sensors, which allow the collection of a wide range of data on individuals' running gait patterns [29]. Such data include spatio-temporal parameters, information about foot rotation, pronation, supination and gait symmetry, and vertical forces.
Although these instruments are commonly used in the study of running and walking indoors, both for rehabilitative purposes and performance improvement, it is important to highlight that they have some limitations. A study by Alton et al. demonstrated that walking on an instrumented treadmill can affect stride length, reduce the range of motion of joint movements, and cause changes in EMG activation [30]. Figure 1.7 shows an example of instrumented treadmill used in laboratory.

Fig. 1.7 Instrumented treadmill, from [7].

All the aforementioned instruments, although highly accurate, have some limitations: their use in laboratory settings does not allow for representing running in real-world scenarios but only in standardized environments. Consequently, metrics related to an athlete's performance are not evaluated, focusing solely on objective measurements of their capabilities [31]. In this context, the development of wearable sensors (such as accelerometers, gyroscopes, magnetometers and pressure insoles) helps to overcome these limitations, providing objective and realistic evaluations of athletes' performance, as well as valuable insights into injury risk mechanisms.

Magneto-Inerzial Measurement Units (MIMUs)

The development of Magneto-Inertial Measurement Units (**MIMUs**) based on Micro-Electro-Mechanical Systems (MEMS) has promoted the use of these technologies in biomedicine, particularly in the field of human motion analysis. The use of miniaturized sensors enables the non-invasive study of human movements and frees from the need to visit a laboratory. Their affordability and low energy consumption further contribute to make these sensors a promising technology. MIMUs are generally equipped with three different orthogonally-mounted tri-axial sensors: an accelerometer (which measures linear and gravitational accelerations), a gyroscope (which measures the body angular rate) and a magnetometer (which measures the magnetic field). All these sensors perform measurements in the local reference frame, which must subsequently be used to estimate the orientation of the sensor (and therefore of the subject) in space. Only after estimating the orientation the collected data can be used to determine the sensor's position in space and perform a spatio-temporal analysis of the athletic gesture [22]. Figure 1.8 shows an example of MIMUs' attachment on different body parts, as it's generally used for running analysis.
It should be noted that the data collected by each sensor are affected by noise and biases. This noise introduces errors in the orientation estimates, which, if not properly handled, can lead to significant inaccuracies. To integrate the information from each sensor and mitigate noise sources, specific sensor fusion algorithms are employed, as discussed in 2.2.

In the following list, the aforementioned sensors are described and analyzed.

- **Accelerometer**
  An accelerometer measures the **proper linear acceleration**, a_p, that indicates the difference between the sensed acceleration (a_s) and the gravitional force g. The accelerometer presents one, two or three sensing axes, which define the reference system of the sensor and the sensing directions.

$$a_p = a_s - g \tag{1.1}$$

  An accelerometer can be modeled as a second order mass-spring-dumper system [10], as depicted in figure 1.9.
  When an acceleration (a) is applied to a proof mass (m), then the applied force

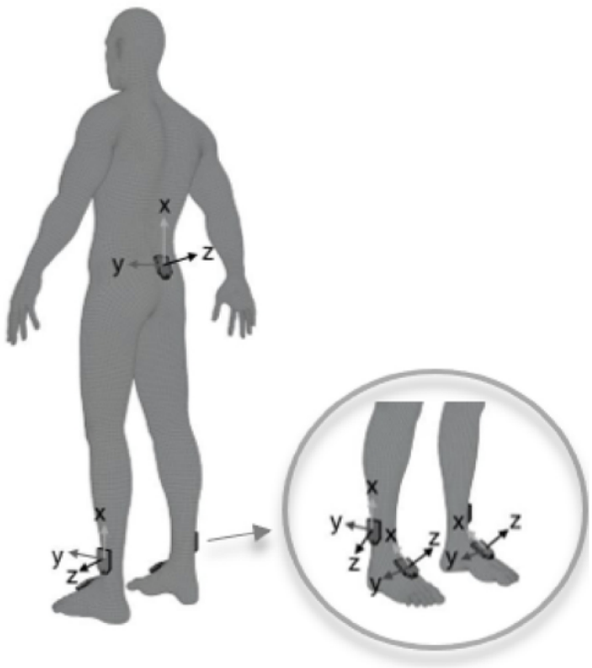

Fig. 1.8 Example of attachment of MIMUs on different body parts with their local reference systems, from [8].

(F_{applied}) on the proof mass is defined as:

$$F_{\text{applied}} = ma \tag{1.2}$$

Moreover, the damping, defined by a constant (b), and the spring (k) act on the proof mass:

$$F_{\text{spring}} = kx \tag{1.3}$$

$$F_{\text{damping}} = b\dot{x} \tag{1.4}$$

It's then possible to apply Newton's second law, according to which the algebraic sum of all applied forces must be equal to the inertial force acting on the proof mass :

$$F_{\text{applied}} - F_{\text{spring}} - F_{\text{damping}} = m\ddot{x} \tag{1.5}$$

$$m\ddot{x} + b\dot{x} + kx = F_{\text{applied}} = ma \tag{1.6}$$

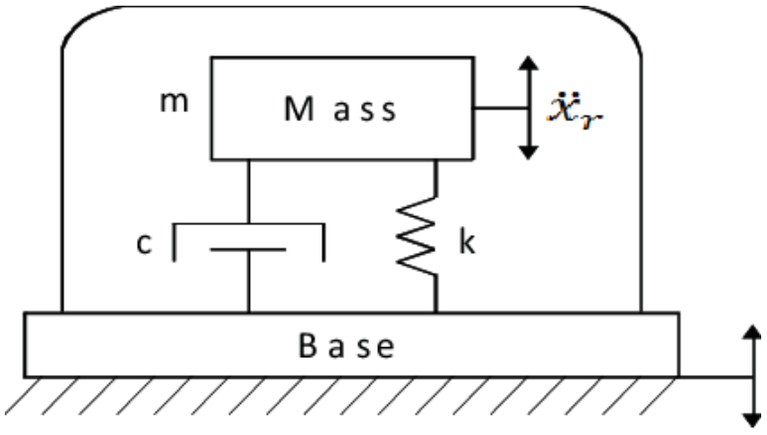

Fig. 1.9 Mechanical model of an accelerometer, from [9].

The latter equation must be solved in the Laplace domain. The transfer function of the non-homogeneous second order differential equation is:

$$ms^2x(s) + bsx(s) + kx(s) = F(s) = ma(s) \tag{1.7}$$

$$s^2x(s) + \frac{b}{m}sx(s) + \frac{k}{m}x(s) = \frac{F(s)}{m} = a(s) \tag{1.8}$$

$$H(s) = \frac{x(s)}{a(s)} = \frac{1}{s^2 + \frac{b}{m}s + \frac{k}{m}} = \frac{1}{s^2 + \frac{\omega_0}{Q}s + \omega_0^2} \tag{1.9}$$

Where, ω refers to the resonance frequency and Q_0 to the quality factor.

$$\omega_0 = \sqrt{\frac{k}{m}} \tag{1.10}$$

$$Q_0 = \frac{m\omega_0}{b} \tag{1.11}$$

When selecting an accelerometer, several factors must be considered. Ideally, the largest possible bandwidth should be achieved, which translates into a higher resonance frequency. A high ω corresponds to a small proof mass and/or a high spring stiffness. However, these parameters cannot be increased indefinitely, as a reduction in the proof mass leads to a degradation of the instrument's sensitivity [10]. Sensitivity is defined as the minimum detectable output variation corresponding to a given input change.

Furthermore, it is important to note that different types of accelerometers

exist, based on how the displacement of the proof mass due to acceleration is converted into a measurable signal. These include capacitive, piezoelectric, piezoresistive, resonant, tunneling, thermal, and optical accelerometers. Among these, capacitive accelerometers are the most commonly used in motion analysis applications. In these devices, the displacement of the proof mass is converted into a proportional change in capacitance, which is then processed and amplified into a voltage signal.
Figure 1.10 shows other accelerometers listed with pro and cons.

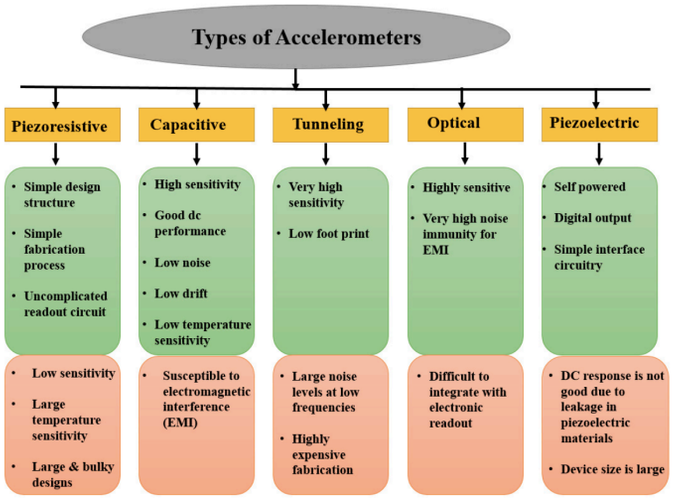

Fig. 1.10 Pro and cons of different accelerometers' transduction scheme, from [10].

- **Gyroscope**
  Gyroscopes are devices able to detect any change of position when a rotation occurs around their sensing axis. There are different classes of gyroscopes, depending on the principle of functioning and the technology used; some examples include: mechanical, optical and MEMS gyroscopes [12]. When choosing a device, it's important to focus on the specifications needed for the application you are interested in. The scale-factor represents the sensitivity of the gyroscope, and minimum scale-factor stability allows for little errors, but requires better instrumentation with higher accuracy, that leads to higher costs of the system. For biomechanical gait analysis, where both accelerometer and angular rate data are needed with reduced space requirements, MEMS gyroscopes are typically used.
  Gyroscopes can have one, two or three sensing axes and, therefore, three different angular rate measurements can be done:

- Roll: horizontal rotation of the body with a front facing perspective.
- Pitch: vertical rotation of the body with a front facing perspective.
- Yaw: horizontal rotation of the body with a top-down perspective.

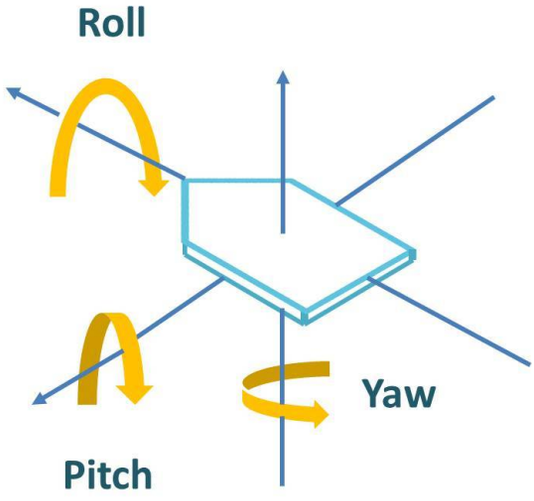

Fig. 1.11 Schematic representation of roll, pitch and yaw rotations, from [11].

A MEMS gyroscope is characterized by two principles of functioning: a **driving** and a **sensing mode**. The former refers to the vibration of the proof mass along the driving axis, while the latter refers to the detection of the movements of vibrations [32]. All MEMS gyroscopes with vibrating elements rely on the energy transfer between two vibration modes caused by the acceleration of Coriolis.
If we consider a disk rotating with a constant angular velocity (Ω) and a particle moving with a transverse velocity (v), then an observer fixed to the disk reference frame would observe that the moving particle deviates from the expected trajectory. This deviation is caused by an apparent force, defined force of Coriolis, proportional to the angular velocity. This principle is used in the MEMS gyroscopes, where the two sensitive axes along which the mass can move are orthogonal (z, y) and can be modeled as spring-mass-damping systems, as depicted in figure 1.12.

Let k_y and k_z be the stiffness parameters, while c_y and c_z the damping coefficients. Then the motion of the proof mass will be governed by Newton's second law:

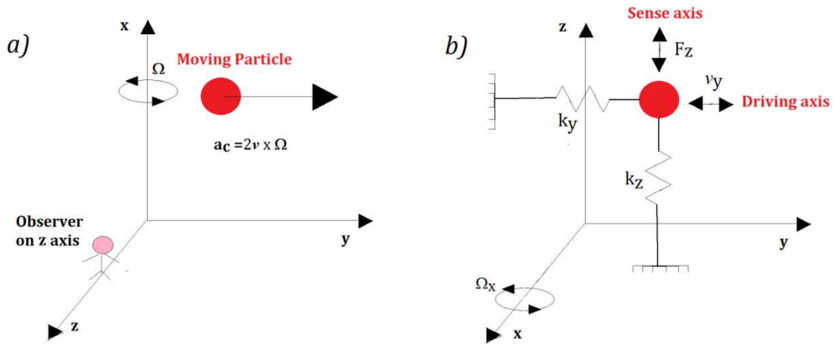

Fig. 1.12 a) Schematic representation of a Coriolis acceleration acting on a generic moving particle; b) Schematic representation of a model of MEMS gyroscope, from [12].

$$m\ddot{y} = -k_y y - c_y \dot{y} + F_{\text{drive}} \tag{1.12}$$

$$m\ddot{z} = -k_z z - c_z \dot{z} + F_{\text{sense}} \tag{1.13}$$

The F_{sense} corresponds to the Coriolis' force, defined as:

$$F_{\text{sense}} = F_{\text{Coriolis}} = |2m\Omega \times v| \tag{1.14}$$

Orthogonal to the constant angular velocity (along x) and the transverse velocity (along y). The displacement of the proof mass along the z axis can be defined as:

$$\Delta z = \frac{2\Omega_x F_{\text{coriolis}}}{m} \frac{Q_y}{\omega_y} \frac{1}{\sqrt{\left(\omega_y^2 + \omega_z^2\right) + \left(\frac{\omega_y \omega_z}{Q_z}\right)^2}} \tag{1.15}$$

The measurable displacement of the proof mass is proportional to the angular velocity Ω_x , which is, indeed, the quantity of interest..

- **Magnetometer**
  A magnetometer is an instrument that measures the magnetic field. A tri-axial magnetometer allows for a univocal definition of the magnetic field where the measurement occurs. Several devices exist, but the ones used for MIMUs are those based on Hall effect.

A Hall probe is defined as a plate of conductive material through which an electric current flows. Any external magnetic field exerts a force on any moving electric charge, known as the Lorentz force:

$$\mathbf{F_L} = q(\mathbf{v} \times \mathbf{B}) \tag{1.16}$$

Due to the Hall effect, a voltage proportional to the component of the magnetic field perpendicular to the plate is generated at the edges of the plate.

Pressure Insoles

Pressure insoles are measuring devices that detect the changes in pressure under the foot sole [33]. They consist of a matrix of sensing elements inserted between foot and sole, connected to a data acquisition system that allows for analysis of the gait pressure patterns. The system is low-cost and portable, which allows for a huge variety of studies both indoor and outdoor [34].

1.2 Thesis Outline

The aim of this work is to contribute to the biomechanical characterization of running by defining a method for estimating running-specific spatio-temporal parameters through signals acquired from MIMUs, which can be applied both to the analysis of level and constant-speed running, as well as to running in other sports contexts.
An in-depth analysis of the literature has revealed that several studies have attempted to characterize spatio-temporal parameters related to running and various sports gestures, using MIMUs placed on the subject's body [22]. The most widely used method involves several steps, starting with the definition of the initial and final ground contact instants, followed by the correct definition of the integration instants, estimation of the sensor orientation, removal of gravity from the accelerometric signal, and concluding with the double integration of the signal to obtain velocity and displacement over time.
The foot orientation estimation is particularly critical; in the present work, the estimation of foot orientation was optimized for running analysis. The parameter settings of different inertial-based algorithms for orientation estimation were fine-

tuned and an automatic framework for the selection of the sub-optimal parameters was proposed, with the ultimate goal of defining a method capable of providing reliable results in terms of stride length despite the running speed and condition.
The thesis project is structured as follow:

- **Chapter 1**: provides an overview of the thesis topic and explains the main aim of the project. This introductory chapter also discusses the biomechanics behind the gesture and provides an explanation of the main instrumentation used for running analysis.
- **Chapter 2**: explains each step of the proposed pipeline, accompanied by an analysis of the state of the art.
- **Chapter 3**: provides explanations of the methods implemented, the data used, and the methodologies employed to carry out the work.
- **Chapter 4**: presents the results obtained.
- **Chapter 5**: presents the discussion over the results obtained and presented in chapter 4.
- **Chapter 6**: provides conclusions and considerations on the work.

Chapter 2

Computation of Level Running Spatio-Temporal Parameters

2.1 Pipeline for Stride Length and Stride Velocity Estimation using foot-mounted MIMUs

The estimation of spatio-temporal parameters from magneto inertial measurement units is typically performed through a double integration of the accelerometric signal. The first integration yields the velocity vector in the three principal directions, while the second integration provides the displacement over time.

To correctly integrate the accelerometric signal, however, it is necessary to perform several steps, as illustrated in the block diagram in 2.1. First of all, to correctly integrate the accelerometric signal, it is necessary to remove the gravitational component. This operation is performed after rotating the signal collected from the sensor and making a necessary estimation of its orientation (section 2.2). Subsequently, the signal cannot be fully integrated, as it is subject to drift caused by thermomechanical and electronic noise, which tends to worsen over time [35]. Therefore, it is essential to divide the signal into segments that allow for leveraging the cyclic nature of the stride during running under known integration conditions (section 2.3). In the following sections, these aspects will be analyzed and explained in detail.

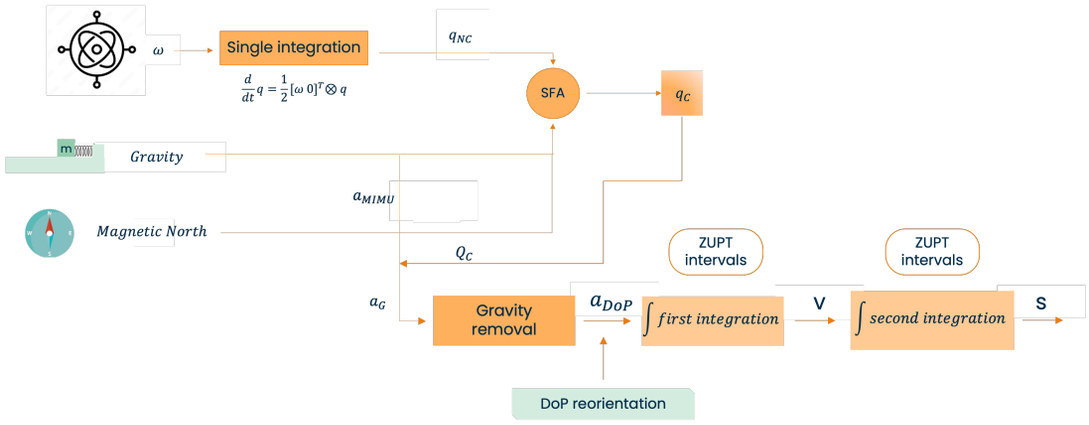

Fig. 2.1 Block diagram of the used pipeline. At the top of the figure, the signals acquired from the magneto-inertial units are shown: acceleration, magnetic field and quaternion derivative obtained from the gyroscope signal. These signals are used by the sensor fusion algorithm (SFA) to obtain a compensated quaternion (q_c) , which is then employed to rotate the accelerometric signal (acc_{MIMU}) into the global reference frame (a_g). Subsequently, the gravitational component is removed from this acceleration, and the resulting signal is integrated twice to obtain the displacement. "ZUPT" interval blocks refer to the selected integration intervals.

2.2 Orientation estimation and gravity removal

An accurate estimation of the sensor orientation is a crucial component within the proposed pipeline for estimating spatio-temporal parameters in running analysis. Properly determining the attitude of the MIMU with respect to the Earth's coordinate system is vital because it enables precise alignment of the sensor's local coordinate system (LCS) with the global coordinate system (GCS). This alignment is essential for correctly removing the gravitational component from the accelerometer data. Even minor errors in the orientation estimation can lead to significant inaccuracies in this alignment, which, in turn, can cause substantial errors in the calculated parameters [36].
Therefore, ensuring high precision in orientation estimation is critical to maintain the overall accuracy of the parameter estimates.

Orientation Estimation

Among all the mathematical tools that can be used to represent the orientation of a sensor in space, quaternions are often preferred. Euler angles, for instance, can suffer from gimbal lock, a phenomenon that causes the loss of one degree of freedom, leading to erroneous readings. On the other hand, the Direction Cosine Matrix (DCM), while detailed, is less commonly used because it requires nine parameters, making its implementation complex and computationally expensive. Quaternions, however, provide an efficient and robust way to represent three-dimensional rotations without encountering the issues associated with the other two methods [37].
A quaternion q is a complex number that can be used to represent the orientation of a rigid body in three-dimensional space [38]. The orientation of the local frame (L) relative to the global frame (G) can be achieved through a rotation around an axis defined in the global frame ($^{G}\hat{n}$), as it is presented in figure 2.2. The notation used in this work for the quaternion is defined as [16]:

$$ {}^{G}_{L}q = \begin{bmatrix} q_0 & q_1 & q_2 & q_3 \end{bmatrix}^T \tag{2.1} $$

where:

$$ q0 = \cos(\frac{\theta}{2}) \tag{2.2} $$

$$ q1 = n_x \sin(\frac{\theta}{2}) \tag{2.3} $$

$$ q2 = n_y \sin(\frac{\theta}{2}) \tag{2.4} $$

$$ q3 = n_z \sin(\frac{\theta}{2}) \tag{2.5} $$

Here, n_x, n_y and n_z denote the components of the rotation axis in G, while θ is referred to the rotation angle.

In the realm of quaternion algebra, the operation known as the quaternion product, symbolized by $\otimes$, is essential for representing combined orientations. If we consider two orientations described by the quaternions $\hat{q}^A B$ and $\hat{q}^B C$, the resultant quaternion $\hat{q}^A C$, which represents the compounded orientation, can be formulated as:

$$\hat{q}^A C = \hat{q}^B C \otimes \hat{q}^A B \tag{2.6}$$

The quaternion multiplication, defined between two quaternions **a** and **b**, adheres to the Hamiltonian product rule. This rule is expressed in the equation:

$$\mathbf{a} \otimes \mathbf{b} = \begin{bmatrix} a_1 & a_2 & a_3 & a_4 \end{bmatrix} \otimes \begin{bmatrix} b_1 \; b_2 \; b_3 \; b_4 \end{bmatrix}^T \tag{2.7}$$

Expanding this, we obtain:

$$\mathbf{a} \otimes \mathbf{b} = \begin{bmatrix} a_1 b_1 - a_2 b_2 - a_3 b_3 - a_4 b_4 \\ a_1 b_2 + a_2 b_1 + a_3 b_4 - a_4 b_3 \\ a_1 b_3 - a_2 b_4 + a_3 b_1 + a_4 b_2 \\ a_1 b_4 + a_2 b_3 - a_3 b_2 + a_4 b_1 \end{bmatrix} \tag{2.8}$$

To rotate a three-dimensional vector using a quaternion, we apply the following transformation:

$$\mathbf{v}^B = \hat{q}^A B \otimes \mathbf{v}^A \otimes \hat{q}^{A*} B \tag{2.9}$$

The rotation matrix corresponding to the orientation $\hat{q}^A B$, denoted as ${}^A_B\mathbf{R}$, is given by:

$${}^A_B\mathbf{R} = \begin{bmatrix} 2q_2^2 - 1 + 2q_1^2 & 2(q_2 q_3 + q_1 q_4) & 2(q_2 q_4 - q_1 q_3) \\ 2(q_2 q_3 - q_1 q_4) & 2q_1^2 - 1 + 2q_3^2 & 2(q_3 q_4 + q_1 q_2) \\ 2(q_2 q_4 + q_1 q_3) & 2(q_3 q_4 - q_1 q_2) & 2q_1^2 - 1 + 2q_4^2 \end{bmatrix} \tag{2.10}$$

Quaternions provide a compact and robust representation of orientation in three-dimensional space, avoiding issues like gimbal lock that can occur with Euler angles. However, Euler angles are often more intuitive for visualizing the orientation of a rigid body because they describe it through successive rotations around the coordinate axes. Thus, converting quaternions to Euler angles can be helpful for gaining a more intuitive understanding of an object's orientation.

The Euler angles ψ, θ, and ϕ correspond to rotations around the z_B, y_B, and x_B axes, respectively, of a body-fixed coordinate system.

Given a quaternion $\mathbf{q} = (q_1, q_2, q_3, q_4)$, where q_1 is the scalar part and q_2, q_3, q_4 are the vector components, the Euler angles can be computed using the following formulas [39]:

$$\psi = \text{atan2}(2(q_2q_3 - q_1q_4), 2q_1^2 + 2q_2^2 - 1) \tag{2.11}$$

$$\theta = -\sin^{-1}(2(q_2q_4 + q_1q_3)) \tag{2.12}$$

$$\phi = \text{atan2}(2(q_3q_4 - q_1q_2), 2q_1^2 + 2q_4^2 - 1) \tag{2.13}$$

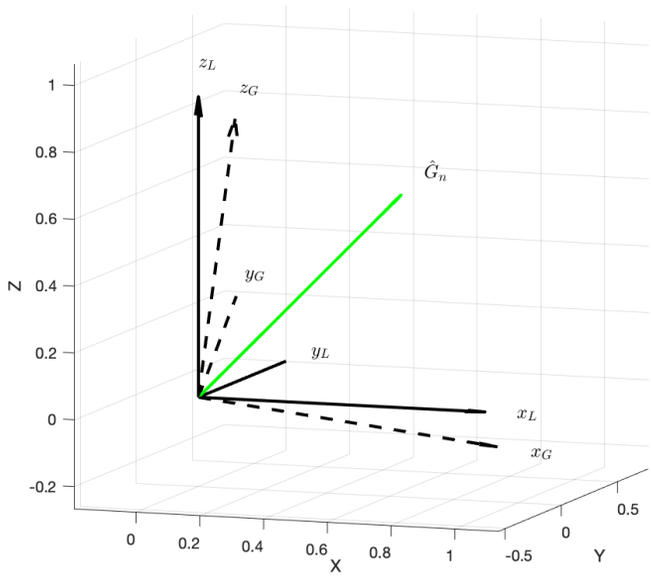

Fig. 2.2 Earth's coordinate system (G), local coordinate system (L) and axis of rotation.

Once the mathematical tools for optimal orientation representation have been introduced, quaternions are presented as the preferred method for defining three-dimensional orientation in space. In the following paragraph, I will elaborate on how this orientation is practically determined by integrating data from accelerometers, gyroscopes, and magnetometers.

By integrating the angular velocities measured by the gyroscope, it would be possible to estimate the sensor's orientation, but only relative to the LCS. Furthermore, gyroscope measurements are subject to biases [40], leading to drift in the estimates with errors increasing linearly over time, and white noise. The latter is a stochastic

component of disturbance whose influence can be measured with the angle random walk (ARW), which quantifies the accumulation of random errors over time, leading to an increasing deviation in orientation estimates as the integration time grows [41]. To overcome these limitations, it's therefore common to use all the information given by the MIMU to improve the accuracy in the estimates. In particular, the accelerometer can be used to correct the tilt error (referred to roll and pitch) thanks to the gravitational information while the magnetometer can be used to correct the heading (referred to yaw). Both sensors present issues that must be considered:

- **Accelerometer**: its main limitation is that it cannot distinguish between gravitational and external acceleration applied to the body. This means that accelerometer data can only be used to determine the sensor's inclination when the body is either in a static condition or moving at a constant velocity. Furthermore, the axis pointing in the direction of the earth's center cannot detect any changes in its measurements, thus making it impossible to estimate the yaw angle [13].
- **Magnetometer**: its sensitiveness to ferromagnetic and electric disturbances can affect the correction, causing an addition of unreliable information. To prevent this issue, it is essential to ensure that no such disturbances are present before relying on the collected data.

The orientation of the MIMU with respect to the GCS is generally estimated using **Sensor Fusion Algorithms** (SFAs), which are capable of integrating complementary data from the accelerometer, gyroscope, and magnetometer to overcome the aforementioned limitations. It is important to note that the orientation of the MIMU can only be computed using an SFA if the MIMU's coordinate system coincides with the LCS; otherwise, the relative positioning of the two reference systems must be known.
SFAs are based on the integration of accelerometer and magnetometer data, appropriately weighted, to enhance the integration of the gyroscope signal (as it's shown in Figure 2.3). There are two main families of algorithms that fuse this information in different ways: **Complementary Filters**, which are based on a deterministic approach, and **Kalman Filters**, which rely on a stochastic approach. Both types are detailed below.

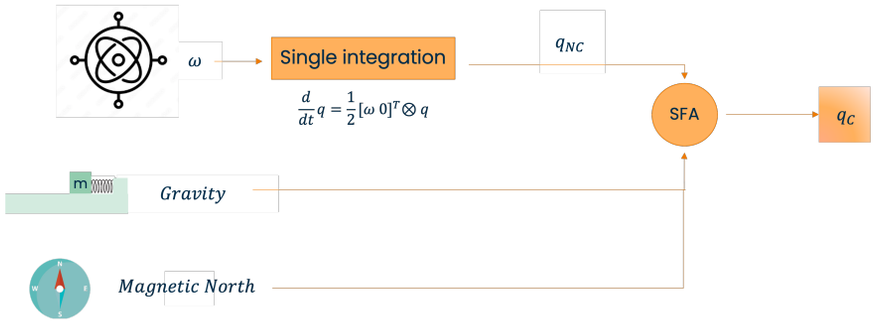

Fig. 2.3 General pipeline for orientation estimation. Q_{nc} refers to the orientation estimate based on gyroscope only, while Q_c refers to the compensate, final quaternion.

2.2.1 Complementary filters

As mentioned before, a **Complementary Filter** (CF) is based on a deterministic approach. This means that it relies on models and equations where the output depends solely on the input and its initial conditions. MIMUs' integrated sensors have a complementary nature: the gyroscope has a good response at high frequencies but is affected by low-frequency disturbances. In contrast, magnetometer and accelerometer are sensitive to high-frequency disturbances but perform well at low frequencies [13].
CFs leverage these specific characteristics by applying a **high-pass filter** (HPF) to the gyroscope data and a **low-pass filter** (LPF) to the accelerometer and magnetometer data, as shown in Figure 2.4. The key is using the same cutoff frequency for both filters, which ensures that the entire signal bandwidth is preserved, preventing the loss of any significant information, as shown in Figure 2.5.

Different CFs vary in the way they weight and use the information taken from accelerometer and magnetometer. In general, this type of methods for orientation estimation is chosen for the ease of understanding of the algorithm itself and the low computational cost. In fact, they do not require any prior knowledge of the system or a complex model of the system, as is the case with Kalman filters (KFs), presented in section 2.2.2.

2.2.2 Kalman filters

Kalman filters (KFs) can be effective alternatives for sensor fusion, utilizing a stochastic approach to address some limitations of CFs. Unlike CFs, which rely

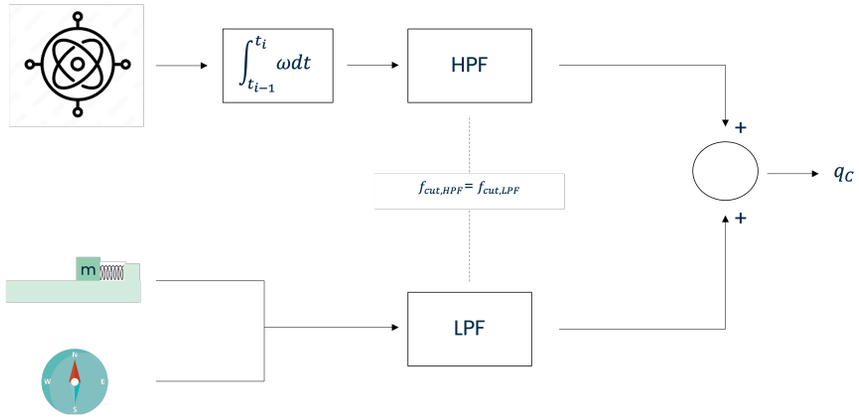

Fig. 2.4 General Complementary Filter block diagram.

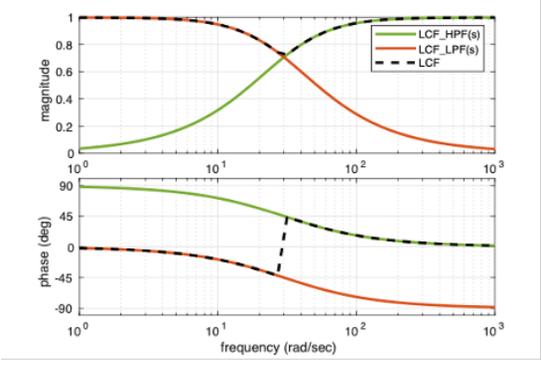

Fig. 2.5 Amplitude and Phase for a CF [13].

on simple mathematical models, KFs are better equipped to capture the complexities of the real world. This category of filters was introduced in 1960 by Rudolf Emil Kalman [42], when an innovative sensor fusion method based on a stochastic approach was proposed for the first time. The goal was to replace deterministic variables with probability distribution functions.

The KF works by continuously correlating the current states of the system with the predicted ones, as shown in Figure 2.6. To use this type of filter, it is necessary for the process we are measuring to be approximable to a linear system and represented by the following linear equations [43]:

$$x_{k+1} = Ax_k + Bu_k + w_k \tag{2.14}$$

$$y_k = Cx_k + z_k \tag{2.15}$$

Where 2.14 represents the state equation, which cannot be measured, and equation 2.15 is a measurable output dependent on x but corrupted by process noise z_k. The matrices A, B and C represent the system parameters; k is the time index; x represents the state of the system; and u is the known input.
We want to use y to obtain an estimate of x. It's at this point that the Kalman filter is introduced, based on two crucial requirements:

- The average value of the estimate is the same as the average value of the system state.
- State estimates that present the smallest deviation to the real state.

Furthermore, the main requirements of the filter dictate that the mean values of the process and measurement noise must be zero, and there should be no correlation between them.
It's then possible to introduce one formulation of the filter, which depends on three main equations:

$$K_k = AP_kC^T \left(CP_kC^T + S_x\right)^{-1} \tag{2.16}$$

$$\hat{x}_{k+1} = (Ax_k + Bu_k) + K_k \left(y_{k+1} - Cx_k\right) \tag{2.17}$$

$$P_{k+1} = AP_kA^T + S_w - AP_kC^T S_z^{-1} CP_kA^T \tag{2.18}$$

Where S_w and S_z are the process noise and the measurement noise covariances , respectively; P is the estimation error covariance matrix; and K is the Kalman gain, which weights the credibility of the measurement (y) through the error covariances and regulates whether to incorporate that information into the state estimates $\hat{x}_{k+1}$. If the measurement error is high, the state estimation depends solely on the input and the previous state x. Concurrently, as the measurement error decreases, the weight K increases, thereby placing greater emphasis on the measurement.

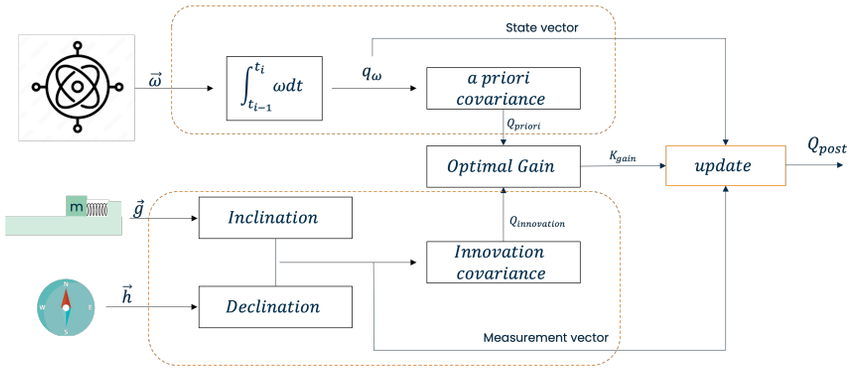

Fig. 2.6 Kalman Filter workflow.

KFs can also be applied to systems that are not strictly linear, as is often the case with real-world systems. In these cases, they are referred to as Extended Kalman Filters (EKFs). The EKF approach involves linearizing the nonlinear function to approximate the dynamic state of the system, achieved by taking into account the mean and covariance of the current state, typically through a Taylor series expansion.[44].
Figure 2.7 shows the working principle of a general Kalman filter.

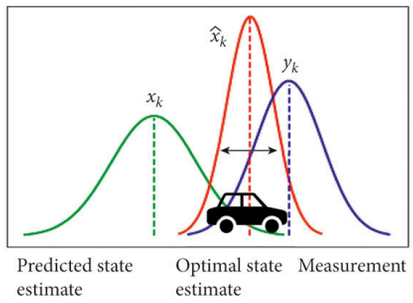

Fig. 2.7 Working principle of a Kalman Filter [14].

Between the two categories of filters presented in the previous sections, there are substantial differences that must be considered when choosing the method to use [45].
A complementary filter primarily offers two advantages: it allows for faster operation due to its low computational cost and generally requires fewer parameters to be set compared to Kalman filters. On the other hand, Kalman filters provide greater flexibility, allowing the filter to be modeled in a manner more suitable to the specific

problem at hand. Moreover, the greater comprehensibility of the functioning of complementary filters constitutes a fundamental criterion that, along with the low computational cost, tends to favor the use of complementary filters.

Gravity Removal

Once the sensor orientation is estimated using the most appropriate method, the sensor data in the LCS can be transformed into the GCS. This transformation is achieved using a rotation matrix ($^{LCS}_{GCS}R$), derived from the quaternion estimates. This step is crucial, as switching the reference frame allows for the removal of the gravity vector component ($\vec{g}$), which in the GCS acts only along the vertical axis with a known magnitude (9.81 m/s^2) and direction. Proper removal of the gravity component isolates the linear acceleration associated with the dynamic movement of interest, enabling a precise analysis of the sports gesture.

$$\mathbf{a_G} = \mathbf{a_G^{raw}} - [0\ 0\ 9.81]\ \text{m/s}^2 \tag{2.19}$$

Where $\mathbf{a_G^{raw}}$ is the acceleration rotated in the GCS before the gravity component removal and $\mathbf{a_G}$ is the GCS acceleration with gravity removed.

2.3 Definition of the Integration Instants

Signals acquired from MIMUs exhibit a fundamental limitation: they are affected by artifacts that introduce an error in the displacement, known as tilt error, which is proportional to the cube of time. To mitigate this undesired effect, the signal is segmented and integrated over smaller temporal windows of only a few seconds. These windows are not randomly selected but are defined based on specific constraints derived from the knowledge of the dynamic system under study.
In running analysis, similarly to gait analysis, the assumption of foot stationarity during the mid-stance phase, characterized by zero velocity and displacement, is often employed. This specific technique, known as **Zero Velocity Update** (ZUPT) [46], has proven effective in reducing errors in stride length and stride velocity estimations during walking [47]. However, its applicability in running has been questioned [48], due to the increased execution speed of movement, which may negate the presence

of a stationary phase. The effectiveness of this technique for estimating integration instants in level running trials at various speeds has been demonstrated in the master's thesis work proposed by Utzeri et al. [49]. The approach used in their study, and followed in the present work, involves setting position and velocity to zero while initializing roll, pitch, and yaw to their initial values. This technique is known as 'hard' ZUPT.

2.4 Double Integration and Drift Removal

Once the integration instants (ZUPT instants) are correctly identified, it should be feasible to proceed with the double integration to define the functions of interest according to the following equations:

$$v(t) = \int_{t_1}^{t_2} a(t)\,dt + v_0 \tag{2.20}$$

$$x(t) = \int_{t_1}^{t_2} v(t)\,dt + x_0 \tag{2.21}$$

where *t1* and *t2* represent two consecutive ZUPT integration instants.
However, it should be noted that there is a drift, caused by electrical and thermo-mechanical noise, which degrades the performance of the double integration. For this reason, it is necessary to introduce techniques that enhance the accuracy of the estimations. In the context of this study, there are primarily two techniques that are commonly used:

- **Linear De-drifting Techniques** [50]: These techniques are based on the estimation of velocity drift, which increases linearly over time, assuming a constant bias on the accelerations.
- **Direct and Reverse Integration (DRI)** [51]: This technique, divided into three phases, initially involves the double integration of the accelerometer signal, accompanied by initial conditions defined by the ZUPT, to obtain a differential d(t). Subsequently, the output signal from the previous step is integrated again, using as initial integration conditions the final conditions obtained from the previous step; this determines r(t). Finally, a time-dependent

function w(t), varying between 0 and 1, is used to weight the sum of the two differentials mentioned above. Through this method, the displacement is defined as:

$$DRI(t) = r(t)w(t) + d(t)(1 - w(t)) \tag{2.22}$$

The weighting function, on the other hand, is defined as follows:

$$w(t) = \frac{s(t) - s(t_1)}{s(t_2) - s(t_1)} \tag{2.23}$$

where s(t) is defined as a function that balances the contributions of r(t) and d(t). A “s-shaped" function is chosen for this purpose to enhance the reliability of the calculation by symmetrically distributing the weight and reducing errors in the original integration.

$$s(t) = \tan\left(\frac{1}{\beta}\frac{2t - t_2}{2t_2}\right) \tag{2.24}$$

here the β factor controls the steepness of the "s-shaped" curve. The value β=0.1 was suggested by the author.

Once the displacement is estimated from the gravity-free accelerometer signal in the global reference frame, the final signal is obtained by reorienting it in the running direction. This is achieved by applying a rotation that maximizes the antero-posterior component [52].

2.5 Estimation of Stride Length and Stride Velocity

Once velocity and displacement have been obtained from the appropriately integrated accelerometer signal (as presented in the previous section), it is possible to calculate the parameters of interest, specifically **Stride Velocity** (SV) and **Stride Length** (SL). SV is defined as the norm of the anteroposterior (AP) and mediolateral (ML) components of velocity, obtained by integrating acceleration between two mid-stance moments, as follows:

$$SV_i = \sum_{n_i} \sqrt{(v_{AP}(n))^2 + (v_{ML}(n))^2} \tag{2.25}$$

where n represents the number of samples in the *i-th* stride considered.
SL, on the other hand, is defined as the norm of the AP and ML components of displacement between two mid-stance moments, as follows:

$$SL_i = \sqrt{d_{AP,end}^2 + d_{ML,end}^2} \tag{2.26}$$

Chapter 3

Materials and Methods

3.1 Datasets

For the implementation of the methods described below, no data acquisition campaign was conducted; instead, two pre-existing datasets at different speeds were used.

3.1.1 Slow running speed dataset - 8/10 km/h

This dataset consists of data recorded from INDIP system [53], made of a 3D accelerometer ($\pm 16g$), a 3D gyroscope ($\pm 2000/s$) and a 3D magnetometer ($\pm 50 Gauss$) sampling at 100 Hz (mod. MITCH, 221e S.r.l., Italy;), placed on the dorsum of each shoe, as shown in Figure 3.1. The gold standard used as reference for the temporal events is a pressure insoles (PI) system (mod. YETI, 221e S.r.l., Padua, Italy; 16 sensing elements; element area = 310 mm^2; fs = 100 Hz; ground reaction force threshold = 5 N [15]). Ten recreational runners (5 males, 5 females, age: 21 ± 1.3 years, height: $167 \pm 7.1 cm$, mass: $63 \pm 8.6 kg$) familiar with the treadmill system were enrolled to run different at 8 and 10 km/h both indoor and outdoor on track in different days. For outdoor trials, speed was kept constant by a running pacer.

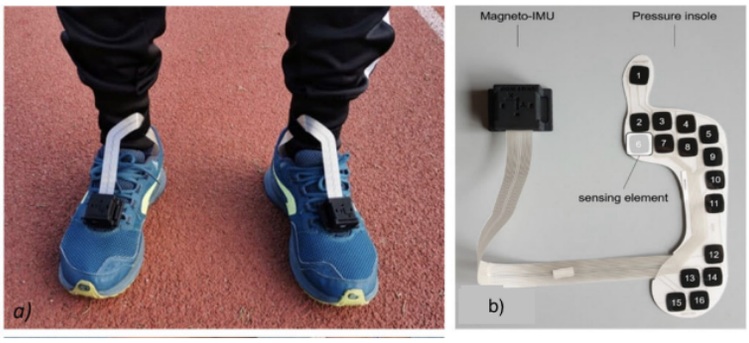

Fig. 3.1 Subject wearing the MIMUs on the shoes (a) and pressure insoles (b) [15].

3.1.2 Moderate speed dataset - 14 km/h

This dataset consists of data recorded from MIMUs, sampling at 200 Hz, placed on the dorsum of shoes and secured with a strap (Opal v2, APDM, Portland, USA; technical specifications: accelerometer range of ±16 g, gyroscope range up to ±2000°/s, magnetometer range of ±8 Gauss) [54]. Furthermore, SP (motion-capture via (9)-camera Vero system, Vicon, Oxford, UK; fs = 200 Hz) was used as gold standard, and retro-reflective markers were applied to the dorsum of the shoes. In the same dataset, MIMUs and markers were placed on the lower leg, thigh, trunk, and pelvis.

Ten male runners (age 32.2 ± 9.9 years, height: 172.5 ± 4.3 cm, weight: 69.4 ± 4.9 kg) were enrolled to run on a treadmill for multiple 90-second trials at a constant speed of 14 km/h while wearing different shoes. The inclusion criteria were: being between 18 and 55 years old, being recreational rearfoot strikers with no injuries in the three months prior to data collection, being able to run effortlessly for 55 minutes, and being familiar with treadmill running. Figure 3.2 shows an example of setup.

Fig. 3.2 Subject wearing MIMUs (under the red tape) together with retro-reflective markers (above the red tape).

3.2 Fine-Tuning of Methods for Orientation Estimation

In this section, the initial phase of the thesis work is detailed. First, an explanation of the state-of-the-art pipeline is provided. Subsequently, the focus shifts to an in-depth analysis of the methods implemented to further enhance the obtained results.
In particular, various sensor fusion algorithms were tested to evaluate whether the **choice of algorithm influences the running analysis**, how it does so, and whether there **exists an algorithm capable of significantly improving the estimates**.
Each step of the general pipeline presented in Chapter 2 used to estimate SL and SV is fundamental and introduces a non-negligible error. Figure 3.3 shows a schematic overview of the base pipeline used as a starting point.

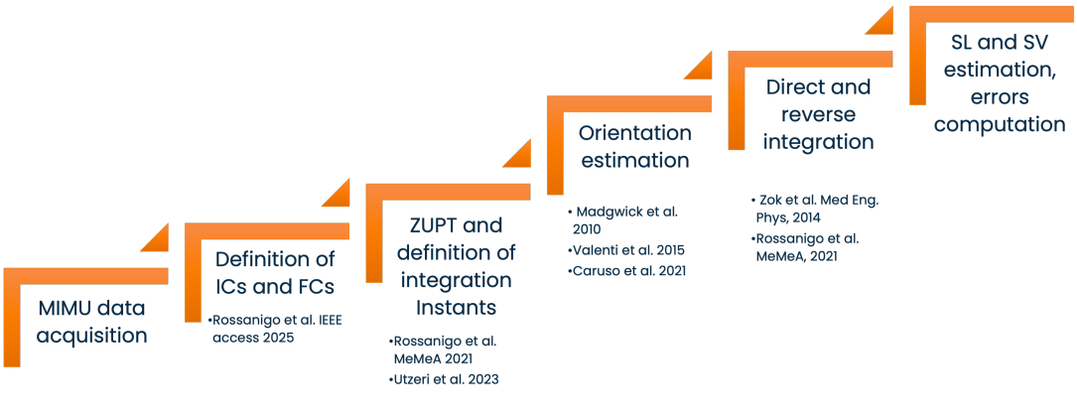

Fig. 3.3 Schematic representation of the pipeline used as basis for this work.

Here, a brief explanation of each step is provided:

- **Definition of ICs and FCs**: an automatic template-based method for feet contacts detection (ICs and FCs) proposed by Rossanigo et al. [55] is used.
- **ZUPT and definition of Integration Instants**: The intervals in which the foot can be considered characterized by a null velocity are determined using a parametric method ([56], [57]) while the integration instants are determined as the minimum of the angular rate norm wihtin the ZUPT intervals.
- **Orientation estimation**: Orientation estimates are determined using Madgwick complementary filter [16] together with Valenti quaternion initialization [17], with a proposed β value of 0.0085 rad/s.
- **Direct and Reverse Integration**: the double integration of the acceleration deprived of gravity is corrected of the residual drift using Direct and Reverse Integration (DRI), proposed by Zok e al. [51].

In the following sections, the methods implemented and optimized in this project are described in detail.

3.2.1 Orientation estimation

Among the ten algorithms proposed by Caruso et al. in 2021 [36] and shown in Table 3.3, three different complementary filters and a Kalman filter were selected for fine-tuning on running trials, after conducting a preliminary analysis of quaternion stability. In fact, stability evaluation served as an inclusion criterion in this study. Furthermore, the number of parameters characterizing each algorithm was an additional factor in determining their suitability. Under the same quaternion stability conditions, algorithms with fewer parameters were preferred, as they are generally easier to fine-tune.

To select a sub-group of the analyzed algorithms for further analysis, a preliminary exploration of the use of those method in running analysis was performed. The chosen metrics to describe orientation stability of ground-level running at constant speed were euler angular differences between successive Initial Contacts (ICs) and the standard deviations of quaternions. Cyclic movements, such as running, although highly dynamic, are expected to produce periodic, stable, and repeatable quaternions. Consequently, the foot angle, estimated from the quaternion, should exhibit similarity between consecutive ICs. Similarly, a low standard deviation is expected throughout the trial in the absence of random fluctuations or drifts. Tables 3.1 and 3.2 summarize the stability metrics obtained for the ten algorithms. Figures 3.4 and 3.5 provide qualitative examples of quaternions for the selected filters and the rejected ones, respectively.

The chosen algorithms were those presenting the lowest stability metrics (Madgwick, Valenti complementary filter, Seel and Guo) and are described below.

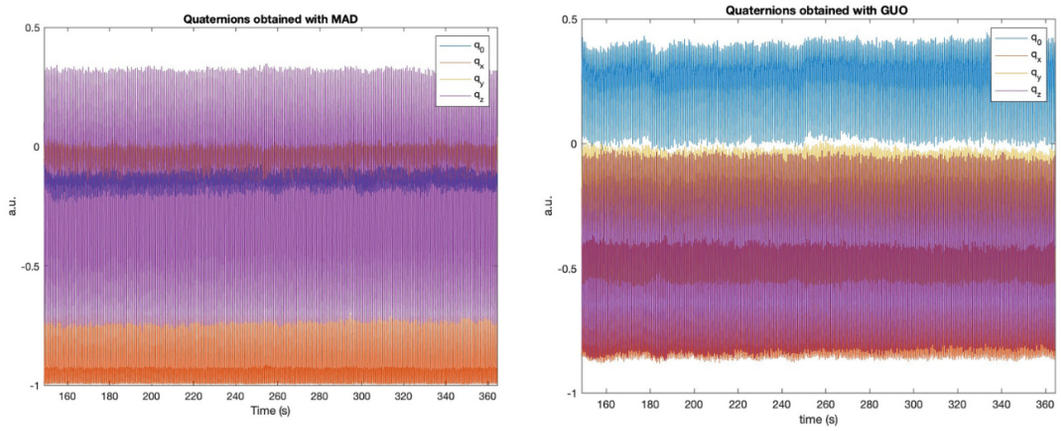

Fig. 3.4 Quaternions obtained from the Madgwick Algorithm (left) and the Guo Algorithm (right) demonstrate high stability, as evidenced by their periodicity and consistent behavior. Both examples visually highlight the absence of random fluctuations or drifts, making these algorithms suitable for further fine-tuning.

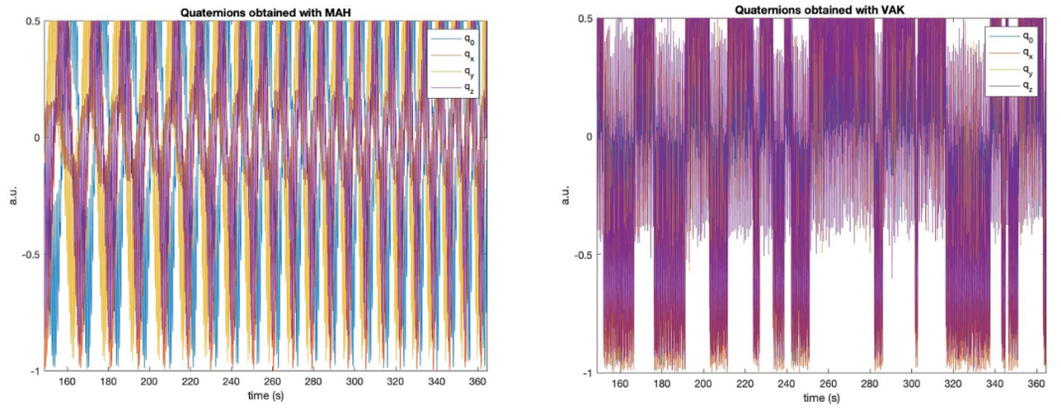

Fig. 3.5 Quaternions obtained from the Mahony Algorithm (left) and the Valenti Algorithm (right) exhibit instability, as evidenced by irregular patterns, random fluctuations, and visible drifts. These characteristics make these algorithms unsuitable for further fine-tuning.

Table 3.1 Stability metrics for each Complementary Filter.

	Madgwick et al. [16]	Valenti et al. [17]	Seel et al. [18]	Mahony et al. [58]	Matlab CF
Mean Angular Differences (°)	-0.0590	-0.0305	0.0037	0.3057	0.1875
Mean Standard Deviation (a.u.)	-0.2058	0.1342	0.2358	0.4954	0.3436

Table 3.2 Stability metrics for each Kalman Filter.

	Guo et al. [59]	Sabatini et al. [60]	Ligorio et al. [61]	Valenti et al. [62]	Matlab KF
Mean Angular Differences (°)	8.5538*10⁻5	-0.321	-0.234	0.0230	-1.2300
Mean Standard Deviation (a.u.)	0.189	0.577	0.546	0.789	0.897

Table 3.3 Parameters for each SFA and brief description.

SFA	Filter type	# Parameters	Tuned parameters	Parameters description
Madgwick et al. [16]	Complementary filter	2	β, rad/s	Gyroscope weighting factor
Valenti et al.[17]	Complementary filter	9	th_{1a}, a.u. th_{2a}, a.u. $gain_{mag}$, a.u. $bias_{alpha}$, a.u.	Lower Threshold for gravity error acceptance Upper Threshold for gravity error acceptance Magnetometer weighting factor Gyroscope bias removal weight
Seel et al. [18]	Complementary filter	4	τ_{mag}, s τ_{acc}, s	Time interval before magnetometer correction Time interval before accelerometer correction
Mahony et al.[58]	Complementary filter	2	k_p, rad/s k_i, rad/s	Inverse gyroscope weighting factor Online bias estimation weighting factor
Matlab Comple-mentary Filter	Complementary filter	2	g_{mag}, a.u.	Magnetometer weighting factor
Guo et al.[59]	Kalman filter	3	σ_{gyr}, rad/s σ_{acc}, m/s^2 σ_{mag}, uT	Gyroscope precision weight Accelerometer precision weight Magnetometer precision weight
Sabatini et al. [47]	Kalman filter	6	σ_{gyr}, rad/s a_{th}, mg	Gyroscope weighting factor Threshold for accelerometer vector selection
Ligorio et al. [61]	Kalman Filter	6	σ_{gyr}, rad/s	Inverse gyroscope weighting factor
Valenti et al. [62]	Kalman filter	3	σ_{gyr}, rad/s σ_{acc}, m/s^2	Inverse gyroscope weighting factor Inverse accelerometer weighting factor
Matlab Kalman Filter	Kalman Filter	8	$(\sigma_{gyr})^2$, $(rad/s)^2$	Inverse gyroscope weighting factor

3.2.2 Madgwick et al.

This complementary filter derivation (MAD)[16] relies on two main components: an orientation estimate derived from gyroscope readings and an estimate based on the accelerometric and magnetometer signals. These sources of information are

integrated using a sensor fusion approach, leveraging the strengths of each sensor type to provide a robust orientation estimate.

- **Orientation from gyroscope readings:** given ${}^{S}\omega$, the vector containing the gyroscope readings, the quaternion derivative ${}^{S}_{E}\dot{\mathbf{q}}$ can be written as:

$$ {}^{S}_{E}\dot{\mathbf{q}} = \frac{1}{2} {}^{S}_{E}\hat{\mathbf{q}} \otimes {}^{S}\omega \tag{3.1} $$

  describing the speed of change in the orientation of the earth frame relative to the sensor frame. The quaternion ${}^{S}_{E}\mathbf{q}$ at time t can be calculated from the derivative by integration:

$$ {}^{S}_{E}\mathbf{q}_{\omega,t} = {}^{S}_{E}\hat{\mathbf{q}}_{\text{est},t-1} + {}^{S}_{E}\dot{\mathbf{q}}_{\omega,t}\Delta t \tag{3.2} $$

  where ${}^{S}_{E}\hat{\mathbf{q}}_{\text{est},t-1}$ is the quaternion estimate at the previous integration instant (*t-1*), ${}^{S}_{E}\dot{\mathbf{q}}_{\omega,t}$ is the quaternion derivative, calculated as the product of the quaternion estimate at the previous instant (*t-1*) and the gyroscope signal at time t, and Δt is the time interval between two measurements. This equation updates the current quaternion using the information about the rate of change in the orientation, as provided by the quaternion derivative.

- **Orientation from accelerometer and magnetometer readings:** For orientation estimates, it can be assumed that accelerometers measure only gravity and magnetometers measure only earth's magnetic field, thus simplifying the derivation of quaternion from these readings. The orientation, in this case, can be achieved by resolving an optimization problem, based on the minimization of an objective function. Here, the right orientation of the sensor (${}^{S}_{E}\hat{\mathbf{q}}$) is the one which alings to a reference direction of the field in the global coordinate system (${}^{E}\hat{\mathbf{d}}$) with the measured field in the local coordinate system (${}^{S}\hat{\mathbf{s}}$).

$$ \min_{{}^{S}_{E}\hat{\mathbf{q}} \in \mathbb{R}^4} f({}^{S}_{E}\hat{\mathbf{q}}, {}^{E}\hat{\mathbf{d}}, \hat{\mathbf{s}}) \tag{3.3} $$

$$ f({}^{S}_{E}\hat{\mathbf{q}}, {}^{E}\hat{\mathbf{d}}, {}^{S}\hat{\mathbf{s}}) = {}^{S}_{E}\hat{\mathbf{q}}^{*} \otimes {}^{E}\hat{\mathbf{d}} \otimes {}^{S}_{E}\hat{\mathbf{q}} - {}^{S}\hat{\mathbf{s}} \tag{3.4} $$

$$ {}^{S}_{E}\hat{\mathbf{q}} = \begin{bmatrix} q_1 & q_2 & q_3 & q_4 \end{bmatrix} \tag{3.5} $$

$$^{E}\hat{\mathbf{d}} = \begin{bmatrix} 0 & d_x & d_y & d_z \end{bmatrix} \tag{3.6}$$

$$^{S}\hat{\mathbf{s}} = \begin{bmatrix} 0 & s_x & s_y & s_z \end{bmatrix} \tag{3.7}$$

Here, Equation 3.3 refers to the minimization problem to solve and Equation 3.4 to the objective function to minimize.

Between all the existing optimization algorithms, the easiest to compute and to understand is the **gradient descent algorithm** presented by Madgwick himself in [16].

Equation 3.8 describes orientation updates using gradient descent algorithm for n iterations with a step size μ. The first iteration is based on an initial quaternion ($^{S}_{E}\hat{\mathbf{q}}_0$), which can be an initial guess, such as $^{S}_{E}\hat{\mathbf{q}}_0 = \begin{bmatrix} 1 & 0 & 0 & 0 \end{bmatrix}$, or defined using sensors specific information, as presented by Valenti et al. in [17]. Equation 3.9 desribes the gradient, defined by the objective function (Equation 3.10) and its Jacobian (Equation 3.11). These equations describe the general form of the gradient descent algorithm for orientation estimation, without making any assumptions about the direction of the specific fields components.

$$^{S}_{E}\hat{\mathbf{q}}_{k+1} = ^{S}_{E}\hat{\mathbf{q}}_k - \mu \frac{\nabla f(^{S}_{E}\hat{\mathbf{q}}_k, ^{E}\hat{\mathbf{d}}, ^{S}\hat{\mathbf{s}})}{\|\nabla f(^{S}_{E}\hat{\mathbf{q}}_k, ^{E}\hat{\mathbf{d}}, ^{S}\hat{\mathbf{s}})\|}, \quad k = 0, 1, 2, \ldots, n \tag{3.8}$$

$$\nabla f(^{S}_{E}\hat{\mathbf{q}}, ^{E}\hat{\mathbf{d}}, ^{S}\hat{\mathbf{s}}) = J^T(^{S}_{E}\hat{\mathbf{q}}, ^{E}\hat{\mathbf{d}}) f(^{S}_{E}\hat{\mathbf{q}}, ^{E}\hat{\mathbf{d}}, ^{S}\hat{\mathbf{s}}) \tag{3.9}$$

$$f(^{S}_{E}\hat{\mathbf{q}}, ^{E}\hat{\mathbf{d}}, ^{S}\hat{\mathbf{s}}) = \begin{bmatrix} 2d_x\left(\frac{1}{2} - q_3^2 - q_4^2\right) + 2d_y(q_1q_4 + q_2q_3) + 2d_z(q_2q_4 - q_1q_3) - s_x \\ 2d_x(q_2q_3 - q_1q_4) + 2d_y\left(\frac{1}{2} - q_2^2 - q_4^2\right) + 2d_z(q_1q_2 + q_3q_4) - s_y \\ 2d_x(q_1q_3 + q_2q_4) + 2d_y(q_3q_4 - q_1q_2) + 2d_z\left(\frac{1}{2} - q_2^2 - q_3^2\right) - s_z \end{bmatrix} \tag{3.10}$$

$$J({}^S_E\hat{\mathbf{q}}, {}^E\hat{\mathbf{d}}) = \begin{bmatrix} 2d_yq_4 - 2d_zq_3 & 2d_yq_3 + 2d_zq_4 & -2d_xq_3 - 2d_yq_2 & 2d_xq_2 + 2d_yq_1 \\ -2d_xq_4 + 2d_zq_2 & 2d_xq_3 - 4d_yq_2 & 2d_xq_2 - 4d_yq_4 & -2d_xq_1 - 4d_yq_3 \\ 2d_xq_3 - 2d_yq_2 & 2d_xq_4 - 2d_yq_1 & -4d_xq_3 + 2d_yq_4 & -4d_xq_2 + 2d_yq_1 \end{bmatrix} \tag{3.11}$$

The Jacobian and the objective function must be appropriately calculated for each of the two fields considered, as the use of a single field does not define a unique orientation. In any case, several simplifications can be made by leveraging certain assumptions about the main directions of the components. Gravity, for instance, acts only along the vertical axis (z), while the Earth's magnetic field has its components on only two axes (horizontal and vertical). The two formulations are then combined into a single set of equations (Equation 3.13), with the subscript ∇ indicating the usage of gradient descent algorithm. It can be chosen whether to use both sensors or just the accelerometric information (Equation 3.14), in case the magnetometer is suffering from uncorrectable ferromagnetic disturbances. Lastly, it is important to emphasize that Equation 3.8 should ideally be iterated multiple times for each new quaternion, resulting in high computational costs. However, as specified in [16], a single iteration per time sample is sufficient (Equation 3.12) if the convergence rate, controlled by μ_t (Equation 3.15), is adjusted to be always greater than or equal to the rate of change of orientation.

$${}^S_E\hat{\mathbf{q}}_{\nabla,t} = {}^S_E\hat{\mathbf{q}}_{est,t-1} - \mu_t \frac{\nabla f}{\|\nabla f\|} \tag{3.12}$$

$$\nabla f = J^T_{g,b}({}^S_E\mathbf{q}_{\hat{est},t-1}, {}^E\hat{\mathbf{b}}) f_{g,b}({}^S_E\mathbf{q}_{\hat{est},t-1}, {}^S\hat{\mathbf{a}}, {}^S\hat{\mathbf{m}}, {}^E\hat{\mathbf{b}}) \tag{3.13}$$

$$\nabla f = J^T_g({}^S_E\mathbf{q}_{\hat{est},t-1},) f_g({}^S_E\mathbf{q}_{\hat{est},t-1}, {}^S\hat{\mathbf{a}}_t) \tag{3.14}$$

$$\mu_t = \alpha \|{}^S_E\dot{\mathbf{q}}_{\omega,t}\| \Delta t, \alpha > 1 \tag{3.15}$$

The goal of a SFA is to combine these two orientations computed from gyrsoscope (${}^S_E\hat{\mathbf{q}}_{\omega,t}$) and accelerometer with magnetometer (${}^S_E\hat{\mathbf{q}}_{\nabla,t}$) separately. The fusion

described by Madgwick et al. is described as follows:

$$ {}^{S}_{E}\hat{\mathbf{q}}_{est,t} = \gamma_t {}^{S}_{E}\hat{\mathbf{q}}_{\nabla,t} + (1-\gamma_t) {}^{S}_{E}\hat{\mathbf{q}}_{\omega,t}, 0 < \gamma_t < 1 \tag{3.16} $$

where γ_t is a weight used to define whether the estimate obtained from the gyroscope or from the other two sensors is more reliable. The optimal value of γ_t, as stated by [16], is the one which ensures that the weighted divergence of ${}^{S}_{E}\hat{\mathbf{q}}_{\omega,t}$ is equal to the weighted convergence of ${}^{S}_{E}\hat{\mathbf{q}}_{\nabla,t}$. This parameters is defined by Equation 3.17, where $\frac{\mu}{\Delta t}$ defines the convergence rate of ${}^{S}_{E}\hat{\mathbf{q}}_{\nabla,t}$ while β refers to the divergence rate of the orientation from gyroscope.

$$ \gamma_t = \frac{\beta}{\frac{\mu}{\Delta t} + \beta} \tag{3.17} $$

Considering a high μ_t value allows for certain simplifications, which can be used to derive the final equation for the fusion of the sensor-derived orientations:

$$ {}^{S}_{E}\hat{\mathbf{q}}_{est,t} = {}^{S}_{E}\hat{\mathbf{q}}_{est,t-1} + \Delta t ({}^{S}_{E}\dot{\mathbf{q}}_{\omega,t} + \beta \frac{\nabla f}{\|\nabla f\|}) \tag{3.18} $$

Figure 3.6 shows the block diagram of the complete filter functioning. β is the main tunable parameter in the algorithm, representig the zero mean gyroscope measurements errors. A low value of the parameter β indicates that the correction of predictions based on accelerometer and magnetometer data is given less weight, attributing greater reliability to gyroscope data. Conversely, a high value of β gives more weight to the data collected from the accelerometer and magnetometer.

Furthermore, a ferromagnetic distortion compensation and a gyroscope bias drift compensation were implemented to overcome the limitations of both sensors, as shown in groups 1 and 2 of Figure 3.6. Here, an additional tunable parameter, ζ, is introduced to control the rate of convergence for removing the bias drift.

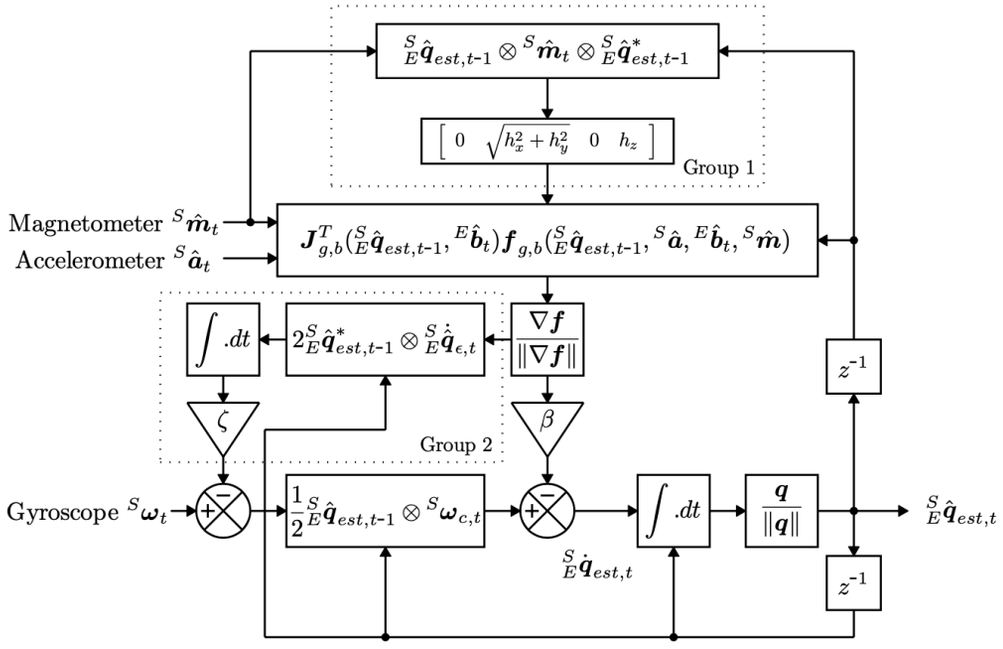

Fig. 3.6 Block diagram of the complete filter, including distortion compensation (group 1) and gyroscope drift compensation (group 2) [16].

3.2.3 Valenti et al.

Valenti et al. (VAC) proposed a complementary filter that can be applied to both IMUs and MIMUs [17]. The algorithm fuses attitude estimation from gyroscope data (prediction step) with accelerometer data (correction step), which provide adjustments for the roll and pitch components only. Additionally, if magnetometer data are available and reliable, they can be used to correct the heading.

The general architecture is shown in Figure 3.7.

- **Prediction**: this step involves the angular rate measured by the tri-axial gyroscope. From the angular velocity described as a quaternion (${}^{S}\omega$) multiplied by the previous state quaternion (${}^{S}_{E}\hat{\mathbf{q}}$) the quaternion derivative is obtained, as presented in Equation 3.19. The orientation of the global frame relative to the local frame can be computed by numerically integrating as described in Equation 3.2.

$$ {}^{S}_{E}\dot{\mathbf{q}}_{est,t} = -\frac{1}{2} {}^{S}\boldsymbol{\omega} \otimes {}^{S}_{E}\hat{\mathbf{q}} \tag{3.19} $$

- **Correction**: this step is based on a multiplicative correction approach. The predicted quaternion is corrected as showed in the following equation:

$$ {}^{S}_{E}\mathbf{q} = {}^{S}_{E}q_{\omega} \otimes \Delta\hat{q}_{acc} \otimes \Delta\hat{q}_{mag} \tag{3.20} $$

Here, the first delta quaternion corrects only the roll and pitch components, while the second corrects the yaw component if magnetometer recordings are provided.

Accelerometer Correction

The inverse predicted quaternion ($^{E}_{S}\mathbf{q}_{\omega}$) can be used to rotate the measured acceleration into the global frame.

$$ \mathbf{R}(^{E}_{S}\mathbf{q}_{\omega})^{S}\mathbf{a} = {}^{E}\mathbf{g}_{p} \tag{3.21} $$

The 'predicted gravity' ($^{E}\mathbf{g}$) will have a deviation from the real gravity vector; therefore, the delta quaternion referred to acceleration used to rotate ($^{E}\mathbf{g}$) into ($^{E}\mathbf{g}_{p}$) is computed, by using:

$$ \mathbf{R}(\Delta q_{\text{acc}}) \begin{bmatrix} 0 \\ 0 \\ 1 \end{bmatrix} = \begin{bmatrix} a_x \\ a_y \\ a_z \end{bmatrix} \tag{3.22} $$

where:

$$ {}^{\mathbf{E}}\mathbf{g} = \begin{bmatrix} 0 & 0 & 1 \end{bmatrix}, {}^{\mathbf{E}}\mathbf{g_p} = \begin{bmatrix} g_x & g_y & g_z \end{bmatrix} \tag{3.23} $$

The solution to the system presented in Equation 3.22 can be obtained by defining an arbitrary yaw ($\Delta q_{3acc} = 0$), thus making the system determined. The solution is:

$$ \Delta q_{\text{acc}} = \begin{bmatrix} \sqrt{\frac{g_x+1}{2}} & -\frac{g_y}{\sqrt{2(g_z+1)}} & \frac{g_x}{\sqrt{2(g_z+1)}} & 0 \end{bmatrix}^{\top} \tag{3.24} $$

As the delta quaternion obtained through 3.24 is still affected by high frequency noise, before applying it, it's necessary to scale it down with an interpolation with the identity quaternion $\mathbf{q_I}$ [17]. Two different approaches are presented,

based on the angle between $\mathbf{q_I}$ and Δq_{acc} (Ω). The angle between the identity and delta quaternions is equal to the Δq_{0acc} component of the same delta quaternion. If $\Delta q_{0acc} > \varepsilon$, a Linear intERPolation (LERP) is used [63]. The governing equations are:

$$\overline{\Delta \mathbf{q}_{\text{acc}}} = (1-\alpha)\mathbf{q}_I + \alpha \Delta \mathbf{q}_{\text{acc}} \tag{3.25}$$

$$\hat{\Delta q_{acc}} = \frac{\overline{\Delta q_{acc}}}{||\overline{\Delta q_{acc}}||} \tag{3.26}$$

Here, ε is the threshold value used to decide wether to apply LERP or the other interpolation method and α is the gain that defines the cut-off frequency of the filter and must be between 0 and 1.

Otherwise, if $\Delta q_{0acc} \leq \varepsilon$, the Spherical Linear IntERPolation (SLERP) is used [63]. This algorithm returs the correct estimate of the average of two points lying on a curve. The governing equation is:

$$\hat{\mathbf{q}_{\text{acc}}} = \frac{sin([1-\alpha]\Omega)}{sin\Omega}\mathbf{q_I} + \frac{sin(\alpha\Omega)}{sin\Omega}\Delta q_{acc} \tag{3.27}$$

The corrected quaternion is computed as follows:

$$\overset{S}{E}\mathbf{q}' = \overset{S}{E}q_{\omega} \otimes \hat{\Delta q_{acc}} \tag{3.28}$$

Magnetometer Correction

If magnetometer recordings are provided, then the yaw correction can be performed the same way by computing the delta quaternion. The measured magnetic field is firstly rotated into the global frame using $\overset{E}{S}\mathbf{q}_{\omega}$, then the magnetic delta quaternion can be computed:

$$\mathbf{R}^T(\Delta q_{\text{mag}}) \begin{bmatrix} l_x \\ l_y \\ l_z \end{bmatrix} = \begin{bmatrix} \sqrt{l_x^2 + l_y^2} \\ 0 \\ l_z \end{bmatrix} \tag{3.29}$$

This delta quaternion rotates the 'predicted global magnetic field' so that it lies on the xz semiplane. This formulation does not affect the roll and pitch components. The solution to the above system is:

$$\Delta q_{\text{mag}} = \left[\frac{\sqrt{s((l_x^2+l_y^2)+l_x\sqrt{(l_x^2+l_y^2)})}}{\sqrt{2(l_x^2+l_y^2))}} \quad 0 \quad 0 \quad \frac{l_y}{\sqrt{s((l_x^2+l_y^2)+l_x\sqrt{(l_x^2+l_y^2)})}} \right]^T \tag{3.30}$$

The delta quaternion is scaled down using the same interpolations used for the accelerometer. The advantage of this double procedure is that it's possible to use two different thresholds, since the delta quaternions are totally independent. The final corrected quaternion formulation is:

$$\overset{S}{E}\mathbf{q} = \overset{S}{E}q' \otimes \Delta\hat{q}_{mag} \tag{3.31}$$

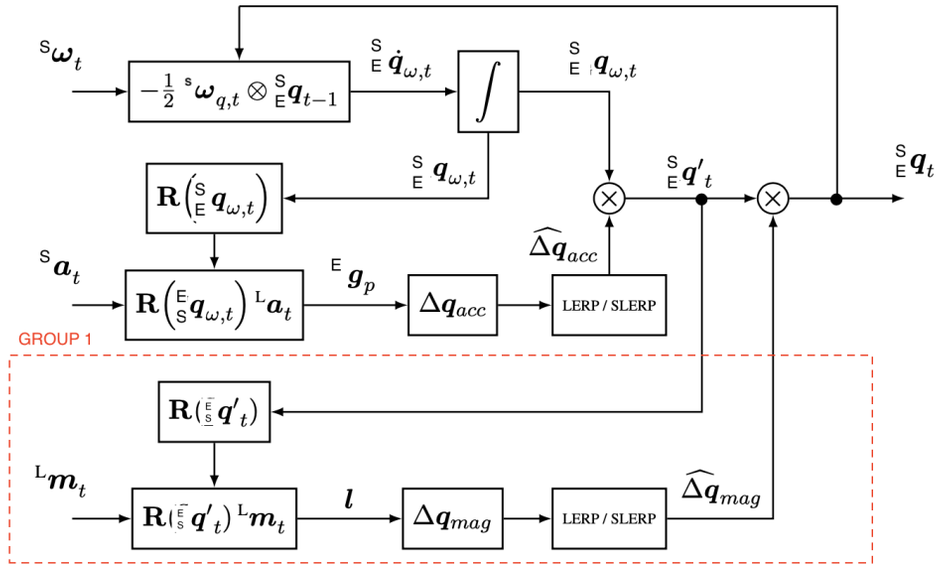

Fig. 3.7 Block diagram of the complementary filter proposed by Valenti et al. [17]. Group 1 describes the optional part of the pipeline that involves the use of magnetometer.

3.2.4 Seel et al.

Seel et al. (SEL) [18] proposed an alternative analytical solution to the minimization problem of the same objective function proposed by Madgwick et al [16], shown in

Equation 3.4. This method, as for the two algorithms described before, provides a prediction step (Equations 3.1 and 3.2) followed by two different corrections, one for the inclination (using the accelerometer) and one for the heading (using the magnetometer).
The minimum of the accelerometric cost function is found by determining the quaternion $q_{as,acc}(t)$, that rotates ${}^{s}r_{acc}(t)$ into ${}^{s}a(t)$, where:

$$\begin{bmatrix} 0 \\ {}^{s}r_{acc} \end{bmatrix} = {}^{S}_{E}\, q_{\omega}(t) \otimes \begin{bmatrix} 0 \\ {}_{E}g \end{bmatrix} \otimes {}^{E}_{S}\, q_{\omega}(t) \tag{3.32}$$

refers to the local sensor coordinate of the vertical unit vector. By determining the angle between both vectors $\alpha_{\text{err,acc}}(t) = \angle({}^{\mathbf{s}}a(t), {}^{\mathbf{s}}\mathrm{r}_{acc}(t))$ and the product we obtain:

$$\mathbf{q}_{\text{as,acc}}(t) = \begin{bmatrix} \cos\left(\frac{1}{2}\alpha_{\text{err,acc}}(t)\right) \\ \sin\left(\frac{1}{2}\alpha_{\text{err,acc}}(t)\right)\mathbf{x}_{\text{corr,acc}}(t) \end{bmatrix} \tag{3.33}$$

and

$$\mathbf{x}_{\text{corr,acc}}(t) = \frac{{}^{\mathbf{s}}a(t) \times {}^{\mathbf{s}}r_{\text{acc}}(t)}{\|{}^{\mathbf{s}}a(t) \times {}^{\mathbf{s}}r_{\text{acc}}(t)\|_2} \tag{3.34}$$

This correction eliminates the differences between ${}^{s}\mathbf{a}$ and ${}^{s}\mathbf{r}_{\text{acc}}$ by using $\mathbf{q}_{\text{as,acc}}(t)$ as a rotation matrix. By using Equation 3.32, it is then possible to conclude that the concatenation of $\mathbf{q}_{\text{as,acc}}(t)$ and ${}^{S}_{E}\mathbf{q}_{\omega}$ minimizes the cost function.
The last step of the accelerometric correction is due to the need to balance drift compensation and disturbance robustness through an adjustable sensor fusion weight, called k_{acc}. This parameter can be tuned between 0 and 1 and regulates the portion of the angle used for the correction.

The overall accelerometric correction quaternion is computed as follows:

$${}^{S}_{E}\mathbf{q}'(t) = {}^{S}_{E}\mathbf{q}_{\omega}(t) \otimes \mathbf{q}_{\text{corr,acc}}(t) \tag{3.35}$$

$$\mathbf{q}_{\text{corr,acc}}(t) = \begin{bmatrix} \cos\left(\frac{1}{2}k_{\text{acc}}\alpha_{\text{err,acc}}(t)\right) \\ \sin\left(\frac{1}{2}k_{\text{acc}}\alpha_{\text{err,acc}}(t)\right)\mathbf{x}_{\text{corr,acc}}(t) \end{bmatrix} \tag{3.36}$$

In order to correct the heading, an additional step for magnetometer-related correction is proposed. ${}^{S}r_{acc}$ is used to project the measured magnetic field vector into the Horizontal plane:

$$ {}^{S}\overline{m}(t) = {}^{S}m(t) - ({}^{S}m(t)^{S}r_{acc})^{S}r_{acc} \tag{3.37} $$

and the governing equation are found by analogy:

$$ {}^{S}_{E}\mathbf{q}(t) = {}^{S}_{E}\mathbf{q}'(t) \otimes \mathbf{q}_{\text{corr,mag}}(t) \tag{3.38} $$

$$ \mathbf{q}_{\text{corr,mag}}(t) = \begin{bmatrix} \cos\left(\frac{1}{2}k_{\text{mag}}\alpha_{\text{err,mag}}(t)\right) \\ \sin\left(\frac{1}{2}k_{\text{mag}}\alpha_{\text{err,mag}}(t)\right)\mathbf{x}_{\text{corr,mag}}(t) \end{bmatrix} \tag{3.39} $$

$$ \alpha_{\text{err,mag}}(t) = \angle\left(\mathbf{m}(t), {}^{s}\mathbf{r}_{\text{mag}}\right) \tag{3.40} $$

$$ \mathbf{x}_{\text{corr,mag}}(t) = \frac{\mathbf{m}(t) \times {}^{s}\mathbf{r}_{\text{mag}}(t)}{\|\mathbf{m}(t) \times {}^{s}\mathbf{r}_{\text{mag}}(t)\|_2} \tag{3.41} $$

The last correction step introduced by Seel et al. consists in a bias compensation, used to reduce the drift and based on both the observed disagreements.

$$ b(t) = b(t - t_s) + k_{bias,acc}\alpha_{err,acc}(t)X_{corr,acc}(t) + k_{bias,mag}\alpha_{err,mag}(t)X_{corr,mag}(t) \tag{3.42} $$

Where $k_{bias,acc}$ and $k_{bias,mag}$ are weighting factors that can be set between 0 and 1, and t_s is the sampling interval. At each sampling interval, the bias is used to estimate the corrected angular rates, which are then integrated to obtain a more accurate gyroscope quaternion prediction (${}^{S}_{E}q_{\omega}$). Finally, this prediction is corrected using Equations 3.35 and 3.38.

The working principle of the method is based on the correct initialization of the four governing parameters. Since this initialization may be rough, a parametrization was proposed, allowing the user to select only the time scale and the level of aggressiveness for the correction. The time scale consists in choosing two time constants (τ_{acc}, τ_{mag}), which represent a measure of the reliability of the correction. The higher the time constant, the less the sensor is considered reliable; therefore, longer time intervals and averaged values are used. The last governing parameter

is the overshoot measure ζ, which takes into account the bias estimation to avoid overcompensations of the disagreements, as shown in Figure 3.8. The same value of ζ must be chosen for both sensors. The relationships between the time constants and the governing parameters shown in the previous dissertation, are given by the following equations:

$$k_i = \frac{t_s}{1.4\tau_i + t_s}, k_{bias_i} = \frac{\zeta^2}{160\tau_i} k_i, \forall i \in (acc, mag) \tag{3.43}$$

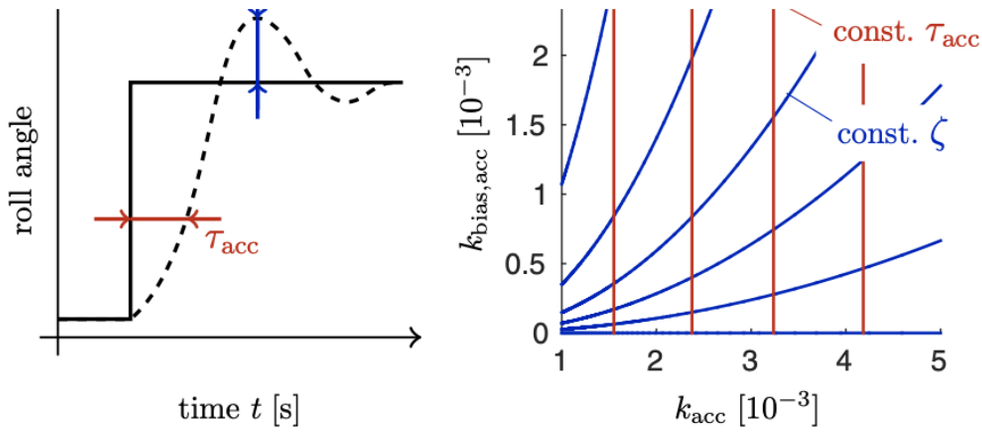

Fig. 3.8 Graphical explanation of accelerometric corrective time constant τ_{acc} and overshoot measure ζ. The same picture could work for magnetometer time constant. Picture from [18].

3.2.5 Guo et al.

The aforementioned algorithms are flexible and easy to understand but have some drawbacks. The main issue concerns the setting of the governing parameters, which may be accurate for a specific application but lead to poor estimates in others. For this reason, a Kalman filter could be a suitable option, providing statistically more accurate estimates.. Guo et al. (GUO) [59] proposed a novel MIMU-based orientation estimation algorithm using a Fast Kalman Filter.

Quaternion derivation from accelerometer and magnetometer readings

This section presents a method for attitude determination using accelerometer and magnetometer data. The relationship between the body frame and the reference frame is modeled using the direction cosine matrix (DCM), which can be expressed in terms of quaternions.
The reference vectors for the accelerometer and magnetometer in the global frame are defined, and it is demonstrated how the DCM can be decomposed into column vectors that depend on the quaternion. The matrices P_1, P_2, P_3, associated with the quaternion, are introduced, and it is demonstrated that their Moore-Penrose pseudoinverses are equal to their transposes.

Next, the magnetometer equation is derived and reformulated as a linear system in terms of the quaternion. This leads to the definition of a matrix W_m that relates magnetometer measurements to the quaternion.
Since this system cannot be directly solved, an iterative approach is proposed, where the quaternion is estimated as the weighted average of the current and previous states.

$$\mathbf{q}_{m,t} = \frac{1}{2}(\mathbf{W}_{m,t} + \mathbf{I}_{4x4})\mathbf{q}_{t-1} \tag{3.44}$$

Where I_{4x4} represents the Identity matrix and q_{t-1} the previous quaternion estimate. Finally, by combining the quaternion estimation from the magnetometer with that from the accelerometer, a novel algorithm for attitude determination is introduced.

$$\mathbf{q}_{a,t} = \frac{1}{2}(\mathbf{W}_{a,t} + \mathbf{I}_{4x4})\mathbf{q}_{t-1} \tag{3.45}$$

$$\mathbf{q}_{t} = \frac{1}{4}(\mathbf{W}_{a,t} + \mathbf{I}_{4x4})(\mathbf{W}_{m,t} + \mathbf{I}_{4x4})\mathbf{q}_{t-1} \tag{3.46}$$

While this provides an initial estimation of the quaternion, it does not account for sensor noise or measurement uncertainties. Therefore, a Kalman Filter is introduced to refine the quaternion estimation by incorporating gyroscope data and modeling the system dynamics.

Kalman Filter design

To improve the attitude estimation, a Kalman Filter is applied, which integrates gyroscope measurements with the previously estimated quaternion. The quaternion

kinematic equation is used as the process model, describing the evolution of the quaternion based on angular velocity:

$$\frac{d\mathbf{q}}{dt} = \frac{1}{2}[\Omega]\mathbf{q} \tag{3.47}$$

where $[\Omega]$ is a skew-symmetric matrix that depends on the angular velocity components $\omega_x, \omega_y, \omega_z$. The discretized system is given by:

$$\mathbf{q}_t = \left[\mathbf{I}_{4x4} + \frac{\Delta t}{2}[\Omega]\right]\mathbf{q}_{t-1} + \xi_t \tag{3.48}$$

where ξ_t represents the process noise, which accounts for uncertainties in gyroscope measurements and model approximations.

To incorporate external sensor information, the measurement model includes the estimated quaternion derived from accelerometer and magnetometer data:

$$\mathbf{q}_{\text{measure},t} = \mathbf{q}_{\text{acc,mag},t} + v_t \tag{3.49}$$

where v_t is the measurement noise, which represents the uncertainties associated with the accelerometer and magnetometer readings. Since these sensors introduce non-linearities, a first-order approximation is used to propagate their uncertainty into the quaternion estimation. This is achieved through the Jacobian matrix J, which maps variations in the accelerometer and magnetometer measurements to variations in the estimated quaternion:

$$\Sigma_v = J\Sigma_{\text{acc,mag}}J^T \tag{3.50}$$

where:

- Σ_v is the covariance of the measurement noise in the quaternion domain;
- J is the Jacobian matrix that describes the sensitivity of the quaternion to measurement variations;
- $\Sigma_{\text{acc,mag}}$ represents the measurement noise covariance of the accelerometer and magnetometer;

This formulation allows the Kalman Filter to optimally fuse gyroscope, accelerometer, and magnetometer data while accounting for their respective uncertainties. The filtering process consists of two main steps: **prediction** and **correction**. The prediction step uses the gyroscope measurements to estimate the next quaternion state, while the correction step refines this estimate using the accelerometer and magnetometer measurements. The Kalman Filter is implemented as follows:

- **State prediction:** Compute the predicted quaternion $\mathbf{q}_t$ based on the process model.
$$\hat{\mathbf{q}}_t = \left[\mathbf{I}_{4x4} + \frac{\Delta t}{2}[\Omega]\right] \mathbf{q}_{t-1} \tag{3.51}$$

- **Covariance prediction:** Update the process uncertainty.
$$\Sigma_{\hat{q},t} = \left[\mathbf{I}_{4x4} + \frac{\Delta t}{2}[\Omega]\right] \Sigma_{q,t-1} \left[\mathbf{I}_{4x4} + \frac{\Delta t}{2}[\Omega]\right]^T + \Sigma_{\xi,t} \tag{3.52}$$

- **Kalman Gain computation:** Calculate the Kalman gain G_k, which determines how much the measurement should influence the state correction:
$$G_k = \Sigma_{\hat{q},t}[\Sigma_{\hat{q},t} + \Sigma_v]^{-1} \tag{3.53}$$

- **State correction:** Update the quaternion estimate by incorporating the measured quaternion.
$$\mathbf{q}_t = \hat{\mathbf{q}}_t + G_k(\mathbf{q}_{\text{measure},t} - \hat{\mathbf{q}}_t) \tag{3.54}$$

- **Covariance update:** Update the state uncertainty.
$$\Sigma_{q,t} = (\mathbf{I}_{4x4} - G_k)\Sigma_{\hat{q},t} \tag{3.55}$$

This iterative process ensures that the final quaternion estimation is more robust to sensor noise and provides a dynamically consistent representation of attitude over time.

For each presented algorithm, the most relevant parameters have been selected for fine-tuning, based on the parameters chosen by Caruso et al. [36]. Table 3.3 presents the selected parameters and provides a brief description.

3.2.6 Quaternion initialization

Each SFA used in this thesis project requires a manual initialization of the quaternion $\mathbf{q}_0$ before proceeding with the update of the quaternion itself and the orientation estimates. As a direct consequence, it is good practice to accurately choose the initial quaternion, using the information provided by the sensors, to ensure that the filter converges rapidly, even when relatively short time intervals are used, as in the running analysis (ZUPT). In this work, the initialization proposed by Valenti et al. [17] is used, which has already been compared to other techniques by [49] and verified as the best approach for running trials analysis.
This method consists in two different algebraic derivations of the orientation quaternion from two independent sensors: accelerometer and magnetometer (if present and reliable). These sensors provide valuable information in static conditions: they should measure gravity and magnetic field relatively. The quaternion can be obtained through the inverse orientation, which results in this overdetermined system:

$$\begin{cases} \mathbf{R}^T({}^S_E\mathbf{q})^L\mathbf{a} =^E \mathbf{g} \\ \mathbf{R}^T({}^S_E\mathbf{q})^L\mathbf{m} =^E \mathbf{h} \end{cases} \tag{3.56}$$

Each equation provides two independent constraints, this causes a lack of unique solution if a disagreement between the sensors readings occurs. So, the system presented in Equation 3.56 can be modified, by reducing one constraint from the second equation:

$$\begin{cases} \mathbf{R}^T({}^S_E\mathbf{q})^L\mathbf{a} =^E \mathbf{g} \\ \mathbf{R}^T({}^S_E\mathbf{q})^L\mathbf{m} \in^E \Pi^+_{zx} \end{cases} \tag{3.57}$$

The constraint requires that all the readings from the magnetometer be confined to the x-z plane, with x being positive.
The total initization quaternion can be seen as:

$${}^S_E\mathbf{q} = \mathbf{q}_{acc} \otimes \mathbf{q}_{mag} \tag{3.58}$$

where $\mathbf{q}_{acc}$ is determined by solving the following system of equations, obtained after observing that gravity has components on the z-axis only and re-writing the first Equation in System 3.57 as follows:

$$R(\mathbf{q}_{acc}) \begin{bmatrix} 0 \\ 0 \\ 1 \end{bmatrix} = \begin{bmatrix} a_x \\ a_y \\ a_z \end{bmatrix} \tag{3.59}$$

Once $\mathbf{q}_{acc}$ is found, it can be used to rotate ${}^{S}\mathbf{m}$ into an intermediate frame, with the z-axis pointing the same as global coordinate frame:

$$\mathbf{R}^{T}(\mathbf{q}_{acc}){}^{L}\mathbf{m} = \mathbf{l} \tag{3.60}$$

where $\mathbf{l}$ is the rotated magnetic field vector. $\mathbf{q}_{mag}$ is the defined as:

$$\mathbf{R}^{\top}(\mathbf{q}_{mag}) \begin{bmatrix} l_x \\ l_y \\ l_z \end{bmatrix} = \begin{bmatrix} \sqrt{\Gamma} \\ 0 \\ l_z \end{bmatrix} \tag{3.61}$$

where:

$$\Gamma = l_x^2 + l_y^2 \tag{3.62}$$

Finally, Equation 3.58 can be used to obtain the initialization quaternion q_0.

3.2.7 Selection of the sub-optimal parameter(s)

For each of the presented algorithms, the selection of sub-optimal set of parameters [19] capable of minimizing errors was performed through various trials on the two datasets. Initially, each parameter was tested at ten discrete values distributed across its full investigation range, chosen based on its specific meaning. Subsequently, by identifying the minima in the error distribution for SL and SV obtained, the search windows were narrowed, and the step size was reduced. This approach allowed for

the identification of the absolute minimum of the distribution.
For algorithms with multiple parameters, the search process was carried out iteratively for each defining parameter in the same manner. All trials were conducted both with and without the magnetometer to verify whether the dataset was affected by ferromagnetic disturbances.

3.3 Implementation of a Framework for the Stride-by-Stride Selection of Parameter(s) in Orientation Estimation Methods

This section introduces the second part of this thesis. In the first part, the optimal selection of the best SFA for running analysis was successfully achieved by tuning either a single parameter or a set of parameters. However, it was shown that this optimization was specific to our datasets and hardware, representing a significant limitation. To overcome this constraint, a more adaptive approach is required, one that defines parameter values stride-by-stride without relying on prior tuning.
The goal of this step is to refine the estimation of SL and SV while maintaining the optimized pipeline described in Section 3.1, with a particular focus on stride-by-stride orientation estimates. To achieve this, the framework was implemented in MATLAB and structured around a central computational module, where spatio-temporal parameters are extracted using the same methodology described in Section 3.1. Additionally, an objective function is introduced to guide the optimization process, alongside a set of constraints that ensure feasible and reliable solutions. Each of these elements is discussed in detail in the following sections.

3.3.1 Sequential Quadratic Programming Algorithm

The optimization framework used is based on the Sequential Quadratic Programming (SQP) algorithm, an iterative method designed for constrained nonlinear problems. This algorithm belongs to the class of quasi-Newton methods, capable of solving a sequence of subproblems by optimizing a quadratic model of the objective function while simultaneously linearizing the constraints. The formulation of each quadratic programming subproblem relies on the quadratic approximation of the Lagrangian

function, with the obtained solution serving as the starting point for the next iteration, thereby progressively improving the optimization.
Consider a general nonlinear optimization problem:

$$\min_x f(x) \tag{3.63}$$

Subject to:

$$h(x) \leq 0, \quad g(x) = 0 \tag{3.64}$$

The associated Lagrangian function is given by:

$$\mathscr{L}(x, \lambda, \sigma) = f(x) - \lambda^T h(x) - \sigma^T g(x) \tag{3.65}$$

where λ and σ are the Lagrange multipliers associated with the inequality and equality constraints, respectively. To find the solution $\nabla\mathscr{L}(x, \lambda, \sigma) = 0$, the SQP algorithm defines an appropriate search direction d_k at each iteration $(x_k, \lambda_k, \sigma_k)$, obtained as the solution of the QP subproblem. In the absence of constraints, the method reduces to Newton's algorithm, which seeks a stationary point where the gradient of the objective function vanishes. A key feature of SQP is its ability to **preserve feasibility within bounded constraints**, ensuring that each iteration remains within admissible limits. The algorithm also exhibits **robustness to numerical inconsistencies**, handling situations where the objective function or constraints return undefined values (e.g., NaN or Inf) by dynamically adjusting the step size.
Additionally, SPQ algorithm employs **advanced feasibility correction strategies** when constraints are violated. These characteristics make SQP a powerful and flexible approach for constrained nonlinear optimization, balancing computational efficiency with solution accuracy ([64],[65]).

3.3.2 Objective Function

Different combinations of objective functions and optimization variables were tested. Initially, a single variable was optimized, specifically the parameter characterizing the chosen SFA (β). This parameter was chosen as the first optimization variable, as the primary focus was to investigate its stride-by-stride variability and its influence

on spatiotemporal parameter estimation and foot trajectory reconstruction.
Subsequently, six additional variables were introduced to assess whether the optimized estimation and the subsequent removal of accelerometer and gyroscope biases could further improve the accuracy of the estimates compared to a priori bias removal based on values obtained from the static calibration of each sensor:

- Residual gyroscope bias along the three axes $(b_{\omega,x}, b_{\omega,y}, b_{\omega,z})$.
- Residual accelerometer bias along the three axes $(b_{a,x}, b_{a,y}, b_{a,z})$.

In this thesis, a lower and an upper limit were defined for each parameter based on the preliminary analysis of the datasets. Specifically, the limits for the parameter β were set to cover the entire possible range (from 0 to 1 rad/s) as a result of various tests, while the limits for the other parameters were determined based on analyses performed on static signals. Furthermore, β was initialized using the results of the previous optimization phase, b_ω was set to the mean value of the static acquisition, and b_a was initialized as a vector of zeros. The maximum number of iterations was set to 1000, while the number of different starting points for each stride was set to 10, the first one defined a priori and the other randomly.
Regarding the objective functions, two different formulations were implemented. The first one was primarily designed to understand the behavior of the optimizer and the underlying algorithm governing the process. It focused on minimizing the errors in stride length and stride velocity with respect to those obtained from the gold standard. This approach provided an optimal reference scenario, allowing both the verification of the method's feasibility and the achievement of the most accurate possible estimates. Figure 3.9 shows the block diagrams of the framework with the gold standard objective function.

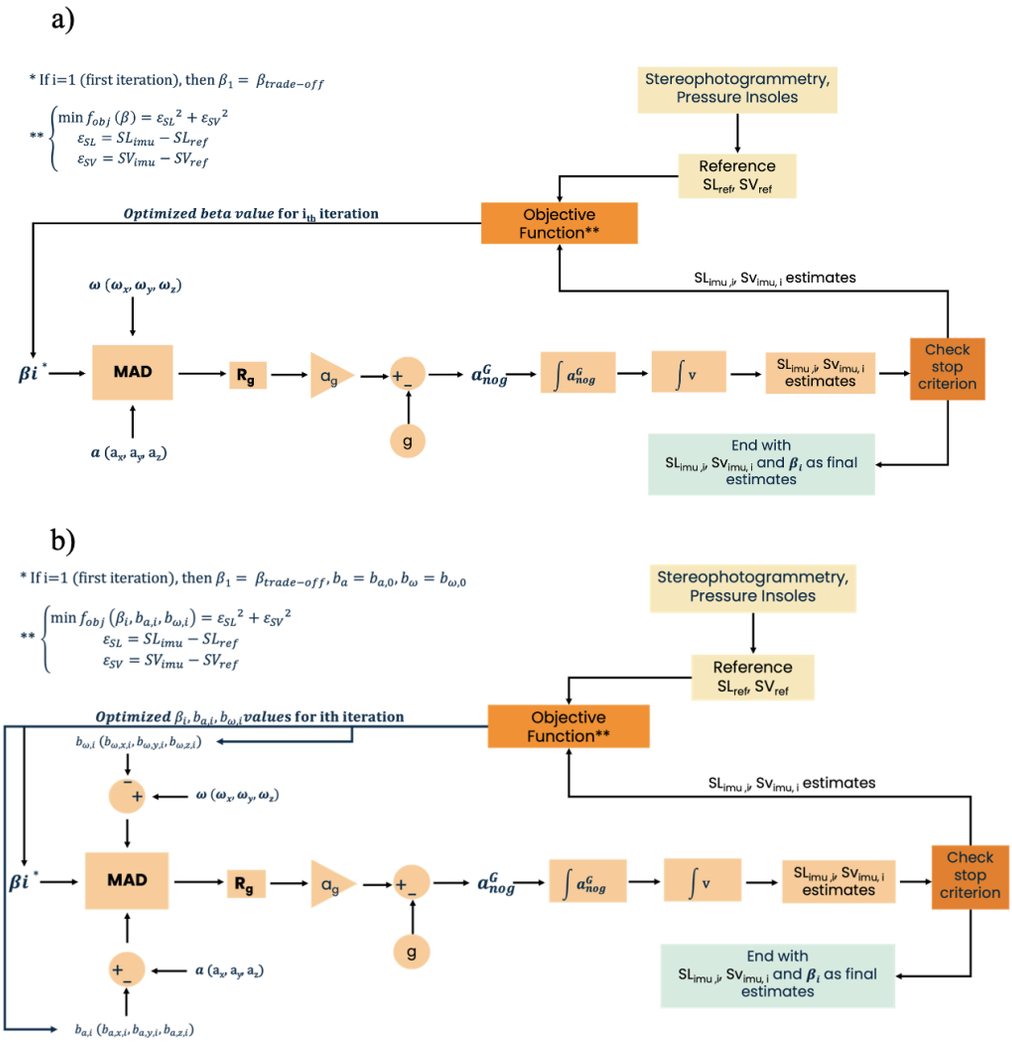

Fig. 3.9 Block diagrams of the framework implementation with a): one optimization variable and b): 7 variables with the objective function that minimizes the errors compared to the reference systems.

Subsequently, the initial objective function was replaced to achieve a formulation independent of reference measurements. Specifically, two systematic and recurrent conditions were exploited at each stride:

- The mean value of the gravity-compensated acceleration must be zero over each integration interval since the integration interval was defined between consecutive zero-velocity instants;

- The vertical displacement between the beginning and the end of the stride must be identical, assuming that the foot returns to the same position during ground-level running;

This transition completely decoupled the optimization framework from reference data, making the method more applicable to real-world scenarios where acquiring reference measurements is neither feasible nor desirable.

a)

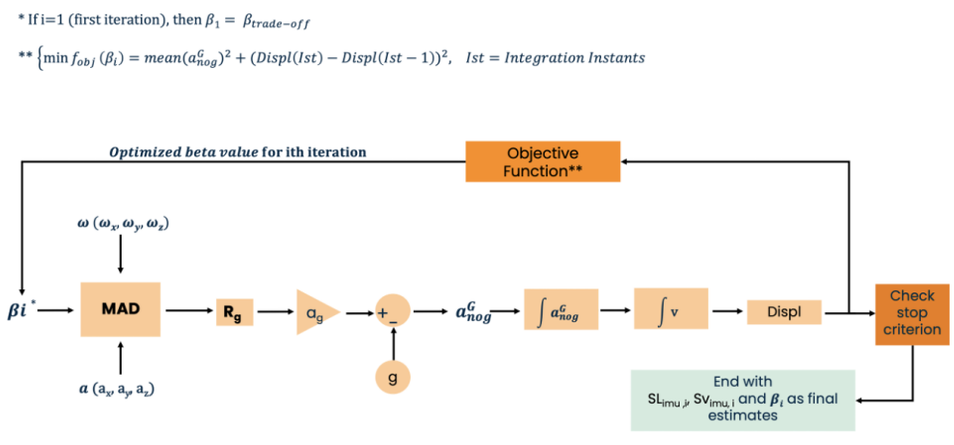

b)

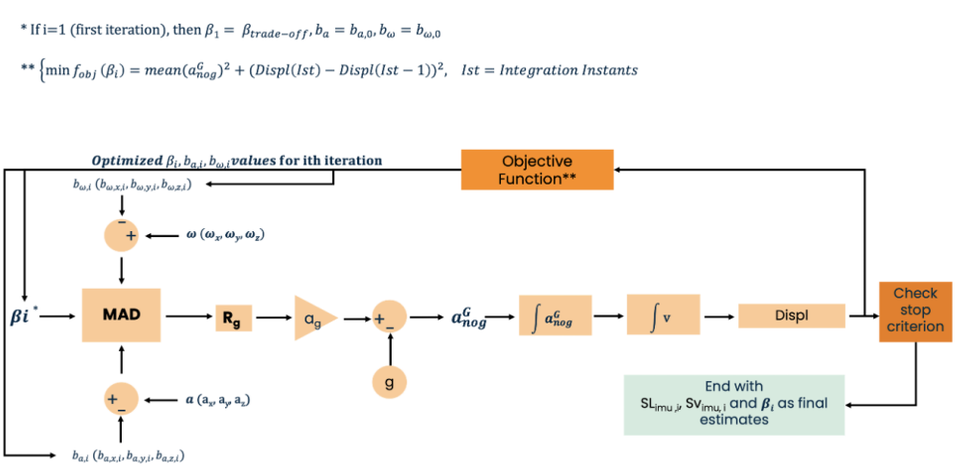

Fig. 3.10 Block diagrams of the framework implementation with a): one optimization variable and b): 7 variables with the objective function that minimizes the errors without the gold standards.

3.3.3 Constraints Definition

Using the objective function without constraints may result in inaccurate SL and SV estimates. A constraint function is introduced to restrict the admissible solution space by incorporating prior knowledge of physical and physiological limitations. Two different constraints function were used, referred to each of the two objective functions detailed above.
For the objective function deprived of references to the gold standard, the imposed constraints are:

- Maximum vertical and medio-lateral displacements were constrained to 50 cm;
- Maximum SL estimate was set to 4 m;
- Minimum SL estimate was set to 1 m;
- The difference between two integration instants in the medio-lateral component was limited to 5 cm;

Meanwhile, for the second objective function, two additional constraints have been introduced in addition to those mentioned above. Specifically, a limitation on the mean value of gravity-free acceleration and on the vertical displacement has been added, as the goal is to minimize the difference between errors without including these two additional elements in the function.

In particular, the mean value of gravity-free acceleration was constrained to 10 $\frac{m}{s^2}$, while the difference in vertical foot displacement between two integration instants was limited to 5 cm.
As shown in Figures 3.9 and 3.10, the estimation of spatio-temporal parameters implemented in the framework follows the same pipeline presented in the first part of this thesis. Specifically, for each considered stride, the orientation of the inertial sensor is estimated by updating the value of the parameter β and the other bias terms. This estimation is used to compute a rotation matrix that allows the acceleration to be transformed into the global reference frame. In this frame, gravity-related acceleration can be removed, enabling the double integration of the gravity-free accelerometer signal. The displacement obtained through DRI [51] is then further reoriented stride-by-stride along the running direction [52].

3.4 Validation Process and Metrics Computation

Slow speed dataset

The reference spatio-temporal parameters of interest (SL and SV) were computed based on the known trial information.
Only an average SL value could be estimated, while the SV value was assumed to be the one imposed by the treadmill or the pacer. Specifically, the average SL was derived from the a priori known information of the distance covered (400 m) and the number of steps taken, provided by the available pressure insoles.

Moderate speed dataset

The reference displacement was computed from the trajectories obtained from SP, incorporating the correction for treadmill motion. For each interval between two consecutive integration instants (ZUPT), the foot trajectory was extracted and corrected by subtracting the initial offset. Finally, the displacement due to treadmill speed was added, yielding the corrected final displacement. Similarly, the reference velocity was computed by computing the first derivative of the marker trajectories obtained through SP.
The reference SL was computed as the norm of the antero-posterior and medio-lateral components of the displacement obtained from markers positioned above the MIMU, as shown in Equation 2.26. Conversely, SV was computed as the norm of the antero-posterior and medio-lateral components of the marker-derived velocity, as shown in Equation 2.25.

At each step of the pipeline, SL and SV errors were computed, using different metrics, in order to decide which orientation algorithm was the best choice. The main metrics are:

- **Mean Error (ME)**: represents the mean of the differences between the observations (y_i) and the associated reference values ($\hat{y}_i$) across all samples.

$$ME = \frac{1}{N}\sum_{i=1}^{N}(y_i - \hat{y}_i) \tag{3.66}$$

- **Mean Absolute Error (MAE)**: represents the mean of the absolute differences between the observations (y_i) and the associated reference values ($\hat{y}_i$) across all samples. This metric is not influenced by the sign of the estimates.

$$MAE = \frac{1}{N}\sum_{i=1}^{N}|y_i - \hat{y}_i| \tag{3.67}$$

- **Mean Absolute Percentage Error (MAPE)**: computes the MAE but expresses the error as a percentage relative to the actual values.

$$MAPE = \frac{1}{N}\sum_{i=1}^{N}\left|\frac{y_i - \hat{y}_i}{\hat{y}_i}\right| \times 100 \tag{3.68}$$

- **Root Mean Square Error (RMSE)**:measures the square root of the mean squared differences between observations and predictions.

$$RMSE = \sqrt{\frac{1}{N}\sum_{i=1}^{N}(y_i - \hat{y}_i)^2} \tag{3.69}$$

Furthermore, for the grid-search optimization, the same constraints used in the optimization framework were introduced to assess whether the SL and SV estimates obtained for a given stride were biomechanically plausible. Specifically, the imposed constraints are:

- Maximum vertical displacement limited to 50 cm;
- Maximum medio-lateral displacement limited to 50 cm;
- Difference in the vertical component between two consecutive stances limited to 5 cm;
- Difference in the medio-lateral component between two consecutive stances limited to 5 cm;
- The absolute mean value of acceleration, after gravity removal, across all three components must be lower than 10 m/s^2.

If any of these constraints are not met, the corresponding stride is considered inaccurate and therefore discarded.

Regarding the implemented framework, if convergence is not achieved, the reference stride is not discarded a priori. Instead, standard parameter values are used, and compliance with the constraints is subsequently verified for that specific configuration.

Chapter 4

Results

This chapter presents the numerical results obtained during the development of this thesis. For each phase of the work, the metrics described in the previous chapter were used to assess the accuracy of the obtained results.

4.1 Stride Length and Stride Velocity Results Using Methods for Orientation Estimation with Fixed Fine-Tuned Parameter(s)

The first analyzed results focus on the influence of SF algorithms on the pipeline currently used for the estimation of spatio-temporal parameters in running. The main steps implemented in the pipeline are detailed in Chapter 2, but are reiterated here for completeness:

- Reorientation of the vertical axis with respect to gravity;
- Identification of initial contacts (ICs) and final contacts (FCs) [55];
- Implementation of the ZUPT detector [49];
- Orientation estimation using the most suitable SFA [66];
- Quaternion initialization through Valenti's algorithm [17];
- Double integration and drift removal using DRI [51];

- Reorientation along the direction of progress;
- SL and SV computation;

4.1.1 Influence of the Orientation Estimation on Stride Length and Stride Velocity Estimates

In this first optimization step, the influence of different SFAs on SL and SV is analyzed. First, for each selected algorithm, fine-tuning was performed by varying all the tuning parameters presented in Table 3.3 within reasonable parameter-specific intervals. The values corresponding to the minimum error obtainable on SL were then selected. As previously done in [66] for the error on velocities, in this case, the focus is on minimizing the error on SL. Tables 4.2 and 4.1 show the minimum errors achievable for each method on each dataset, along with the selected parameters.

Table 4.1 MAPE on SL (%) on both datasets, divided for speed.

SFA	Sub-optimal parameters UNISS	MAPE SL, %		Sub-optimal parameters DIADORA	MAPE SL, %
		8 km/h	10 km/h		14 km/h
MAD	$\beta = 0.076$ rad/s	1.87 ± 1.77	$1.25 \pm 0.0.75$	$\beta = 0.51$ rad/s	2.55 ± 1.77
VAC	$a_{th2} = 1$ a.u., $gain_{mag} = 0.1$ a.u.	5.22 ± 2.44	6.20 ± 3.33	$a_{th2} = 0.7$ a.u., $gain_{mag} = 0.1$ a.u.	15.90 ± 5.65
SEL	$\tau_{acc} = 0.1$ s, $\tau_{mag} = 0.02$ s	3.67 ± 2.10	2.72 ± 2.25	$\tau_{mag} = 0.4$ s , $\tau_{acc} = 0.01$	7.52 ± 1.31
GUO	$\sigma_{gyr} = 0.08$ rad/s, $\sigma_{mag} = 0.2$ uT, $\sigma_{acc} = 0.3$ m/s^2	3.82 ± 2.55	3.90 ± 2.80	$\sigma_{gyr} = 0.1$ rad/s , $\sigma_{mag} = 0.01$ uT, $\sigma_{acc} = 0.3$ m/s^2	3.82 ± 1.27

Table 4.2 MAPE on SV (%) on both datasets, divided for speed.

SFA	Sub-optimal parameters UNISS	MAPE SV, %		Sub-optimal parameters DIADORA	MAPE SV, %
		8 km/h	10 km/h		14 km/h
MAD	$\beta = 0.076$ rad/s	4.12 ± 1.89	2.98 ± 0.92	$\beta = 0.51$ rad/s	2.63 ± 1.52
VAC	$a_{th2} = 1$ a.u., $gain_{mag} = 0.1$ a.u.	7.86 ± 1.45	9.82 ± 2.33	$a_{th2} = 0.7$ a.u., $gain_{mag} = 0.1$ a.u.	15.14 ± 7.73
SEL	$\tau_{acc} = 0.1$ s, $\tau_{mag} = 0.02$ s	10.67 ± 3.47	5.56 ± 1.57	$\tau_{mag} = 0.4$ s, $\tau_{acc} = 0.01$ s	7.24 ± 2.78
GUO	$\sigma_{gyr} = 0.08$ rad/s, $\sigma_{mag} = 0.2$ uT, $\sigma_{acc} = 0.3$ m/s^2	9.81 ± 4.56	9.95 ± 2.67	$\sigma_{gyr} = 0.1$ rad/s , $\sigma_{mag} = 0.01$ uT, $\sigma_{acc} = 0.3$ m/s^2	3.75 ± 1.29

Slow-Speed Dataset

For the slow-speed dataset, the graphical results of the fine-tuning process used to define the sub-optimal parameter(s) for each SFA are shown in Figures from 4.1 to 4.4. Initially, a preliminary tuning was performed over the entire parameter interval. After this step, the search interval and step size were progressively reduced until the sub-optimal parameter value was obtained for the specific algorithm configuration, speed, and hardware. To select the best algorithm for the application, the evaluation was not limited to identifying the one that yielded the lowest SL errors. Instead,

additional criteria were considered, such as the number of parameters required by each algorithm and the extent to which parameter selection influenced the estimation of the variables of interest. To achieve this, after identifying the most influential parameter for each algorithm, its impact on the estimates was assessed through a statistical test (Figures 4.5 and 4.6).

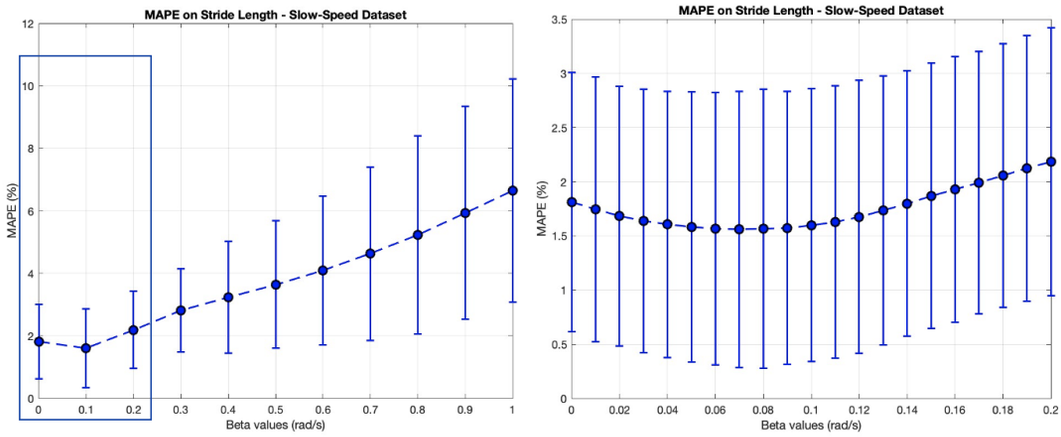

Fig. 4.1 Fine-tuning of the governing parameter of MAD over the Slow-Speed Dataset. The figure on the left shows the overall view of the MAPE across different β values, covering the whole interval. The figure on the right shows the errors varying within a smaller interval. It can be observed that the standard deviation is lower for smaller β values, suggesting that lower β values lead to more stable and reliable estimates.

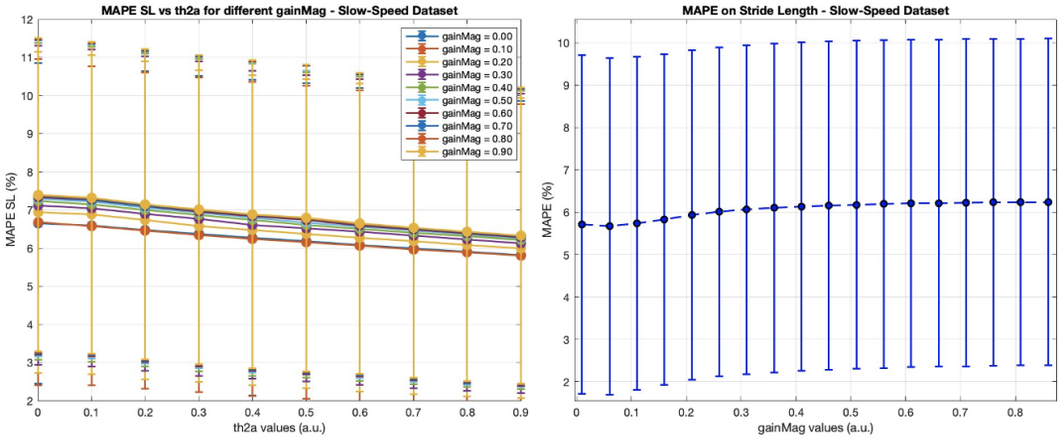

Fig. 4.2 Effect the governing parameters of VAC on MAPE for Stride Length estimation in the Slow-Speed Dataset. The left figure shows the variation of MAPE across different values of th2a for multiple gainMag settings, where a cross-tuning was performed on both parameters, with error bars representing standard deviations. The right figure illustrates the trend of MAPE as a function of gainMag, where the best th2a value was kept fixed, and a zoom-in was applied to the gainMag values for a more detailed analysis.

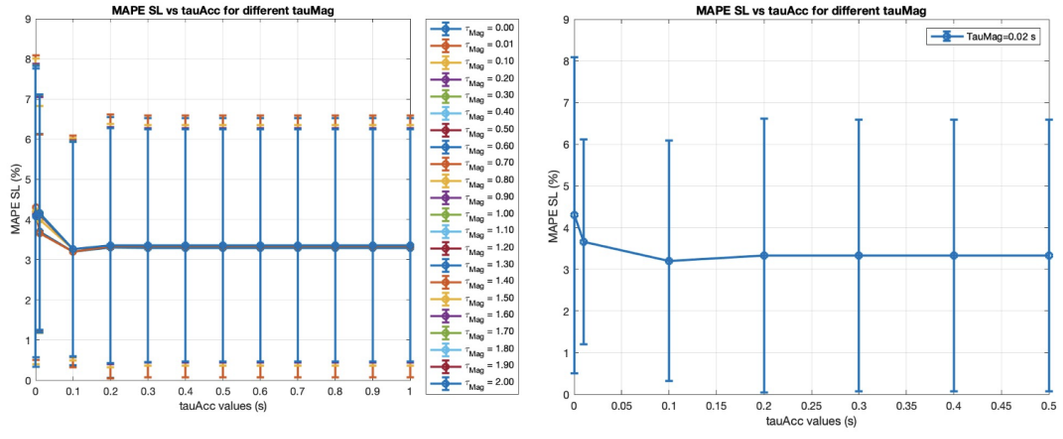

Fig. 4.3 Effect the governing parameters of SEL on MAPE for Stride Length estimation in the Slow-Speed Dataset. The left figure shows the variation of MAPE across different values of τ_{acc} for multiple τ_{mag} settings, where a cross-tuning was performed on both parameters, with error bars representing standard deviations. The right figure illustrates the trend of MAPE as a function of τ_{acc}, where the best τ_{mag} value was kept fixed, and a zoom-in was applied to the gainMag values for a more detailed analysis.

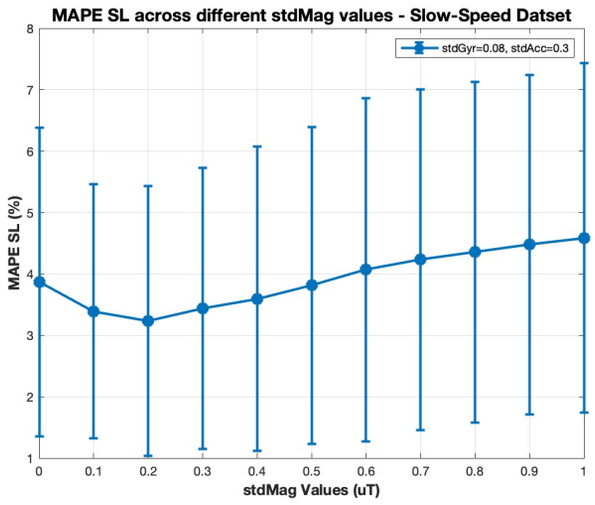

Fig. 4.4 The image shows the trend of the error as stdMag varies, while the other two parameters were previously fine-tuned using a double cross-fine tuning process, similarly to the other algorithms.

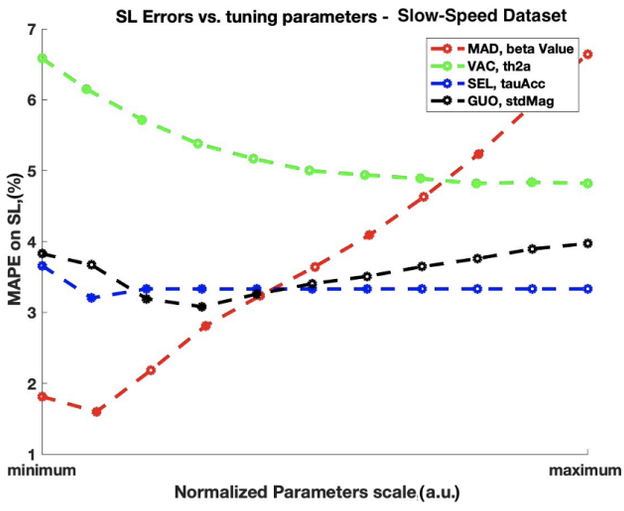

	p value
MAD	< 0.01*
VAC	< 0.01*
SEL	< 0.01*
GUO	< 0.01*

*significant difference

Fig. 4.5 SL errors on the Slow-speed dataset, varying with the most relevant parameter for each algorithm. On the left, the results of the statistical test indicate whether the chosen parameter influences the estimates.

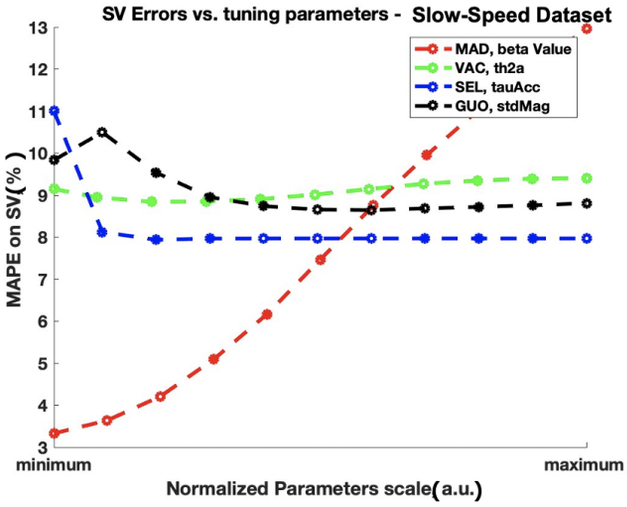

	p value
MAD	< 0.01*
VAC	0.08
SEL	< 0.01*
GUO	< 0.01*

*significant difference

Fig. 4.6 SV errors on the Slow-speed dataset, varying with the most relevant parameter for each algorithm. On the left, the results of the statistical test indicate whether the chosen parameter influences the estimates.

Moderate-Speed Dataset

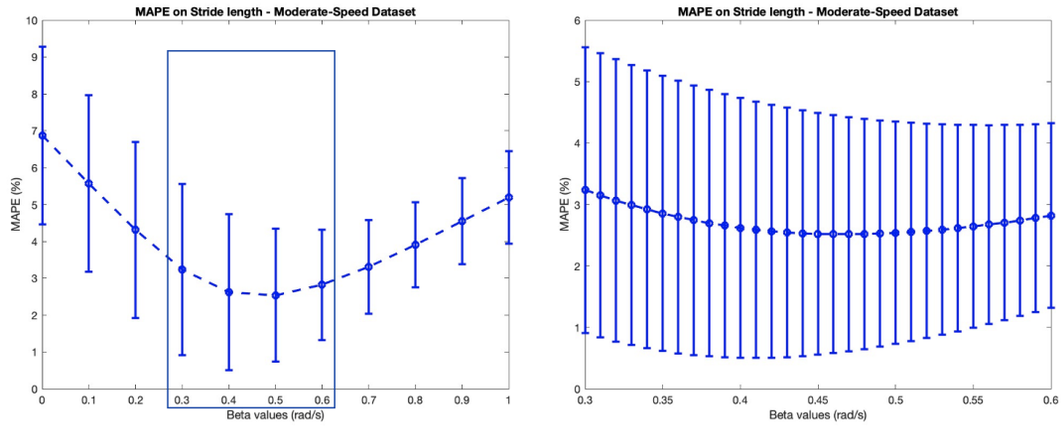

Fig. 4.7 Fine-tuning of the governing parameter of MAD over the Moderate-Speed Dataset. The figure on the left shows the overall view of the MAPE across different β values, covering the whole interval. The figure on the right shows the errors varying within a smaller interval. It can be observed that the standard deviation is lower for medium-high β values, suggesting that medium β values lead to more stable and reliable estimates.

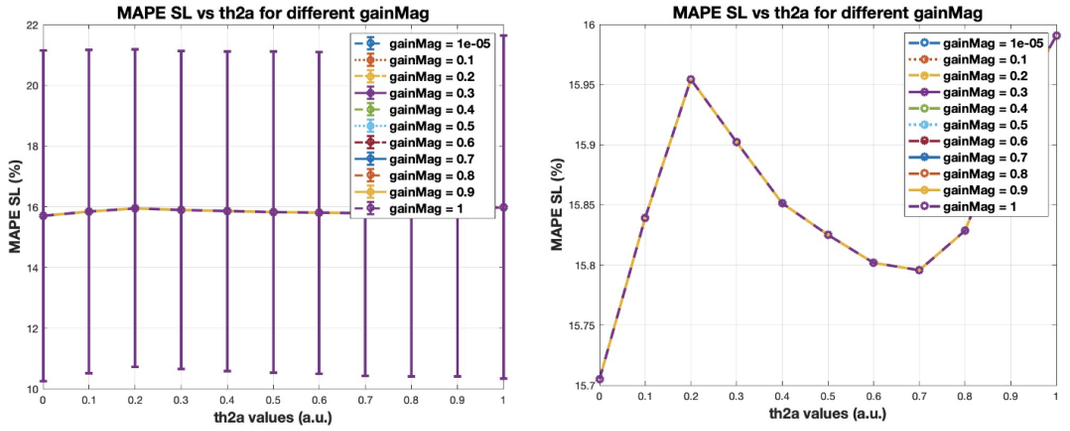

Fig. 4.8 Fine-tuning of the governing parameters of VAC for the Moderate-Speed Dataset. The $gain_{mag}$ parameter showed no influence on the mean absolute percentage errors; therefore, the value proposed by [19] was used. Instead, the chosen value of $th2_a$ is 0.7 rather than 0, as 0 has no significance given the fixed value of $th1_a$ at 0.05.

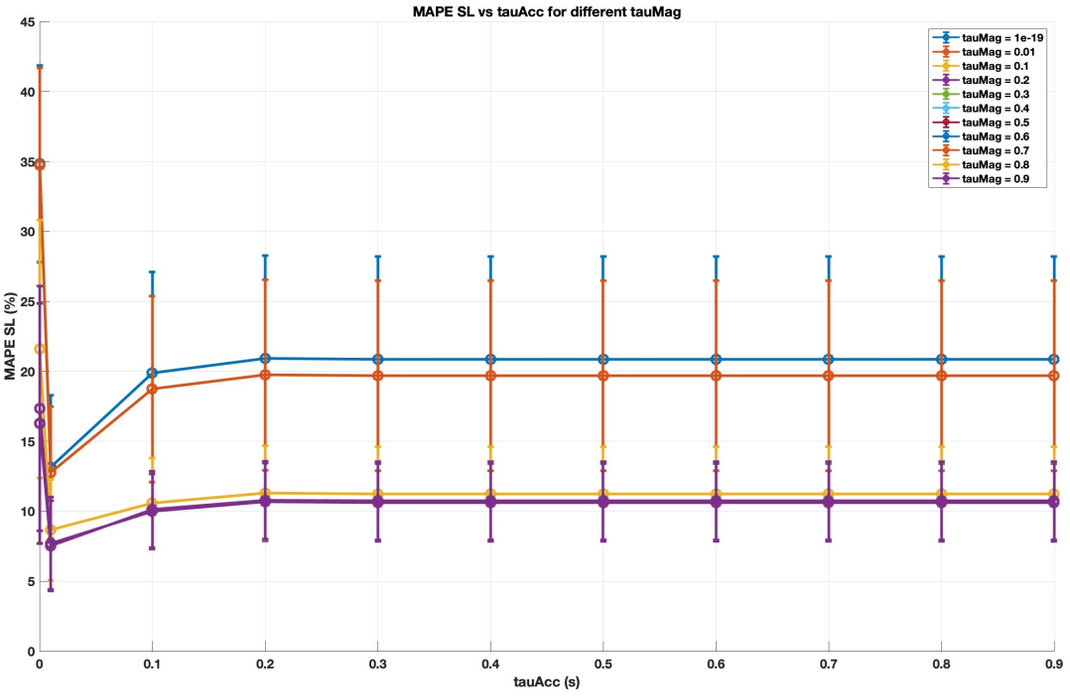

Fig. 4.9 Fine-tuning of the governing parameters of SEL for the Moderate-Speed Dataset.

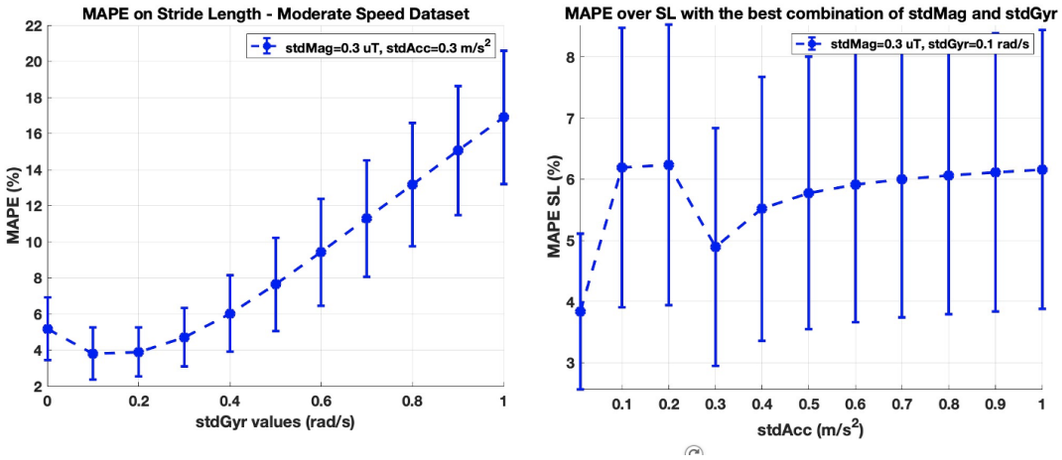

Fig. 4.10 On the left, the variation of the percentage error on SL is shown as a function of stdGyr, using the stdMag and stdAcc values that provide the best performance. On the right, with stdGyr and stdMag fixed, the effect of stdAcc variation on the error is analyzed. The most influential parameter is stdGyr, while stdAcc and stdMag have a lesser impact on the estimation of spatio-temporal parameters. The tuning of stdMag is not reported, as it was found to be the least influential parameter.

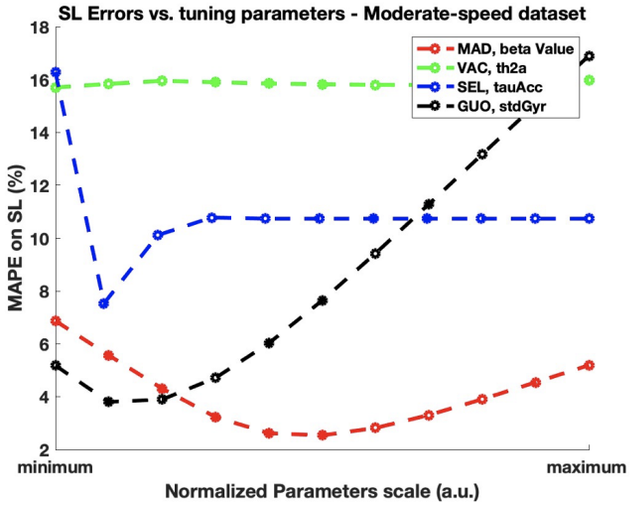

	p value
MAD	< 0.01*
VAC	0.71
SEL	< 0.01*
GUO	< 0.01*

*significant difference

Fig. 4.11 SL errors on the moderate-speed dataset, varying with the most relevant parameters for each algorithm. On the left, the results of the statistical test indicate whether the parameter influences the estimates.

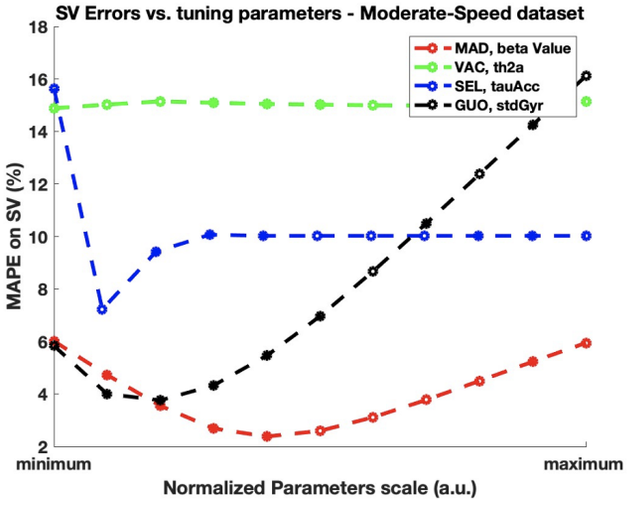

	p value
MAD	< 0.01*
VAC	0.88
SEL	< 0.01*
GUO	< 0.01*

*significant difference

Fig. 4.12 SV errors on the moderate-speed dataset, varying with the most relevant parameters for each algorithm. On the left, the results of the statistical test indicate whether the parameter influences the estimates.

For these datasets, at these three constant speeds, the algorithm proposed by Madgwick et al. [16] was selected as the most suitable for the purpose of the study. This choice was made both because it provides the best results in terms of error for both spatio-temporal parameters of interest (errors equal to or lower than 2.6% for SL and 4% for SV) and because it requires only a single parameter to be tuned.
Although Figures 4.5 and 4.11 show that the results are statistically dependent on the value of the chosen parameter, these two characteristics led to the selection of MAD as the most valuable algorithm for further analysis.

4.1.2 Selection of a Fixed Optimal Value of the Parameter(s) of Methods for Estimation Orientation across Speeds

Once the most suitable algorithm for estimating the parameters of interest in the specific application was selected, in this case, the algorithm by Madgwick et al. [16], the optimal parameters for each dataset were determined. As shown in Table 4.3, the optimal value differs between the low-speed dataset and the moderate-speed dataset. As already observed in the various figures illustrating the tuning process, the estimation of spatio-temporal parameters varies significantly with changes in the governing parameters of the algorithm. For all algorithms (considering intervals of 0.1 rad/s),

at each speed, there is a statistical difference in the estimates as the parameter varies, except for VAC at low speed, which, however, is characterized by high error and standard deviation. The statistical test performed in this case is the Kruskal-Wallis test, since the obtained distributions are not normal and more than three groups need to be compared.

After making these observations, the next step is to define a range of beta parameter values that can be used across different speeds and hardware configurations without requiring any prior tuning. To achieve this, the two available datasets were used, selecting an interval where the error on SL remained below 4 % and showed no statistical difference between estimates (p-value > 0.01). The proposed and tested range includes beta values between 0.29 and 0.34 rad/s, while the unique proposed beta value is 0.3 rad/s.

In Figure 4.13 , the trend of the curves for different speeds can be observed, along with the proposed range. Moreover, Figure 4.14 shows the boxplot of the mean absolute percentage error over SL, obtained with a beta value of 0.3 rad/s, when the distributions are not statistically different from each other. In Table 6, the results obtained using the single proposed beta value are shown.

In general, it can be stated that for both datasets, SL errors are higher than the optimal ones but always remain below the defined tolerance bound of 4 %.

Table 4.3 Performance evaluation for different sub-optimal beta values across datasets expressed as median value ± InterQuartile Range (IQR).

Sub-optimal Beta value (rad/s)	**Dataset**	**MAPE SV (%)**	**MAPE SL (%)**	**Number of strides**	**Unreliable strides (%)**	**Computation time for 1 stride (s)**
0.076	8 km/h	4.12 ± 1.89	1.87 ± 1.77	16911	0	0.020 ± 0.001
0.076	10 km/h	2.98 ± 0.92	1.25 ± 0.75	15372	0	0.020 ± 0.010
0.510	14 km/h	2.63 ± 1.52	2.53 ± 1.77	21430	0	0.010 ± 0.001

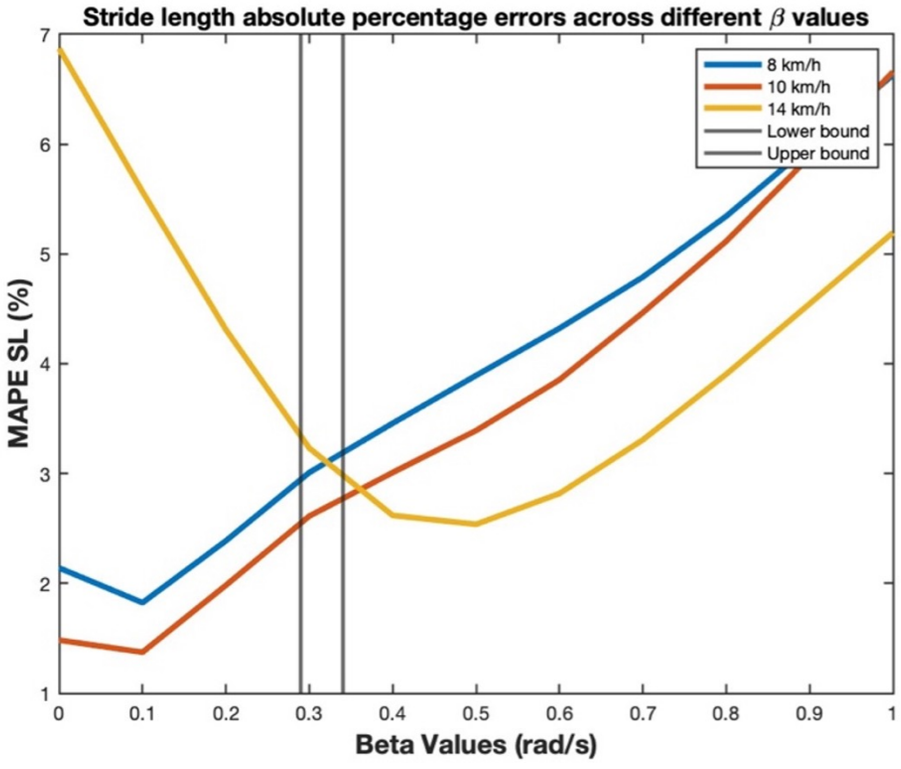

Fig. 4.13 Different error distributions across various beta values for different speeds. The vertical lines indicate the boundaries within which the error distributions show no statistically significant difference between speeds.

Table 4.4 Performance evaluation for different datasets with the unique beta value proposed, expressed as median value ± IQR.

Sub-optimal Beta blue!50 **value (rad/s)**	**Dataset**	**MAPE SV, %**	**MAPE SL, %**	**Number of strides**	**Unreliable strides (%)**	**Computation time for 1 stride (s)**
0.3	8 km/h	7.11 ± 3.64	3.01 ± 1.44	16911	0	0.020 ± 0.001
0.3	10 km/h	2.50 ± 1.71	2.61 ± 1.39	15372	0	0.020 ± 0.010
0.3	14 km/h	2.85 ± 2.11	3.21 ± 1.55	21430	0	0.010 ± 0.001

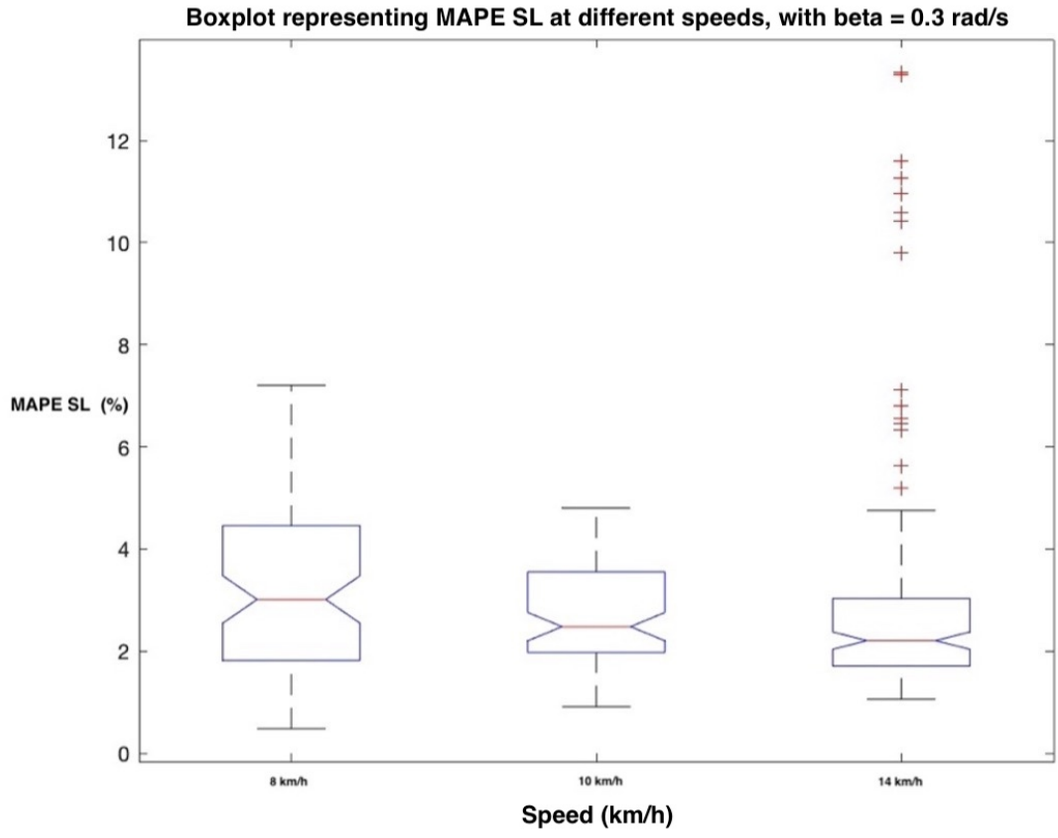

Fig. 4.14 Boxplots for MAPE SL at different running speeds with a unique beta value used. These distributions are not statistically speed-dependent.

Through this process, the feasibility of using an automatic method for estimating SL at different speeds and with different hardware has been verified. However, the proposed approach consists of multiple implementation steps, each introducing an error that propagates. At this stage, the approach was therefore evaluated without the error propagation introduced by the automatic method for selecting the initial and final contact instants [55] and the ZUPT method [49] for selecting the integration instants. In this case, the contact instants obtained from stereophotogrammetry and pressure insoles were used, and the integration instants were set at 50 % of the interval between the detected IC and FC.

The tuning presented in Section 4.1.1 was performed again on both datasets for the selected algorithm, using the reference instants. Figures 4.15 and 4.16 show the tuning results compared with those presented in Section 4.1.1, while Tables 4.5, 4.6 and 4.7 present the results with the sub-optimal beta values for each method at

different speeds.

The ultimate goal of this step was to define a wider range for different users, to be proposed regardless of hardware, implemented methods, and speeds. To achieve this, another interval (between 0.5 rad/s and 0.65 rad/s) was identified where SL errors were below 4 % and showed no statistical difference (p-value < 0.01) between estimates at different speeds from reference-determined contacts and integration instants, as shown in Figure 4.17.

Finally, these two intervals were merged, considering, for all the obtained curves, the area under the 4 % SL error acceptability constraint. In this case, a general interval between $\beta = 0.3$ rad/s and $\beta = 0.52$ rad/s was selected. The result is graphically represented in Figure 4.18.

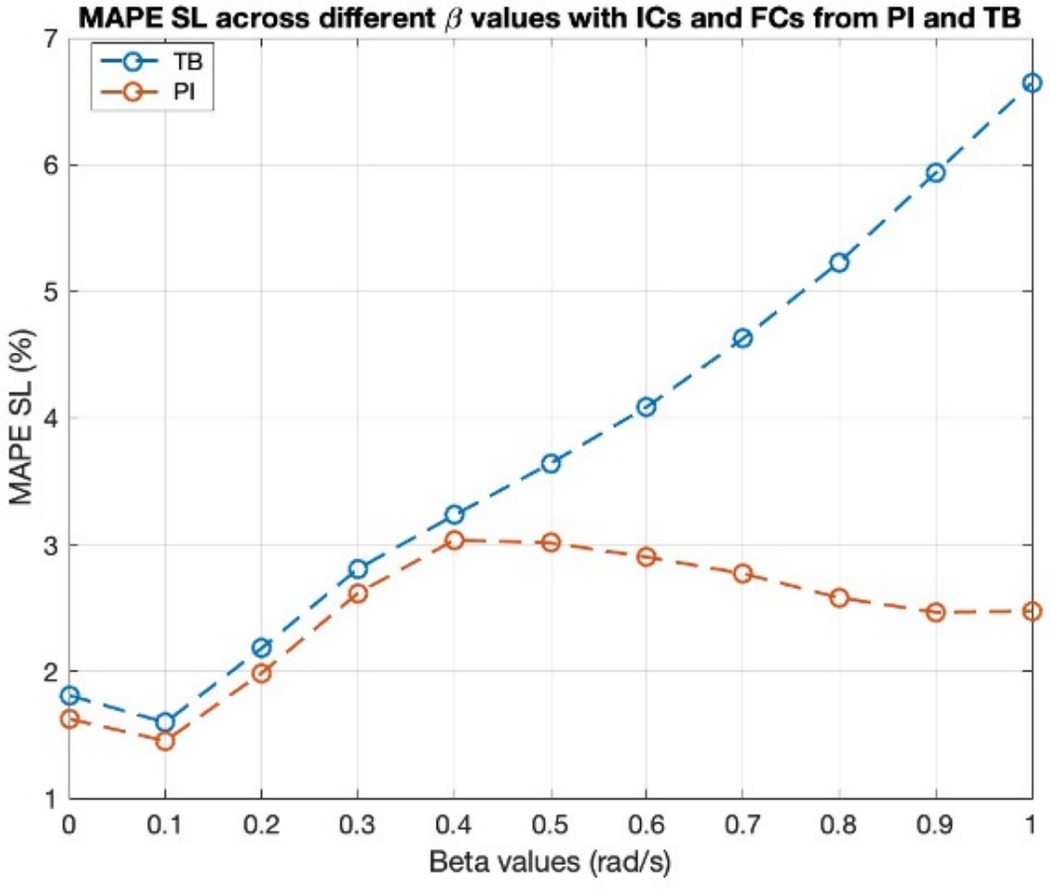

Fig. 4.15 Tuning performed over slow-speed dataset both with contacts defined from template-based method and from reference system.

Table 4.5 Performance evaluation with the sub-optimal beta values both for results from template-based (TB) ICs and FCs detection method and for pressure insoles-based (PI) method. All the results are proposed as median value ± IQR.

Sub-optimal Beta value (rad/s)	Speed	Condition	MAPE SV, %	MAPE SL, %
0.076	8 km/h	TB	4.12 ± 1.89	1.87 ± 1.77
0.100	8 km/h	PI	3.98 ± 1.43	2.02 ± 1.22

Table 4.6 Performance evaluation with the sub-optimal beta values both for results from template-based (TB) ICs and FCs detection method and for pressure insoles-based (PI) method.All the results are proposed as median value ± IQR.

Sub-optimal Beta value (rad/s)	Speed	Condition	MAPE SV, %	MAPE SL, %
0.076	10 km/h	TB	2.98 ± 0.92	1.25 ± 0.75
0.100	10 km/h	PI	2.44 ± 1.22	1.38 ± 0.88

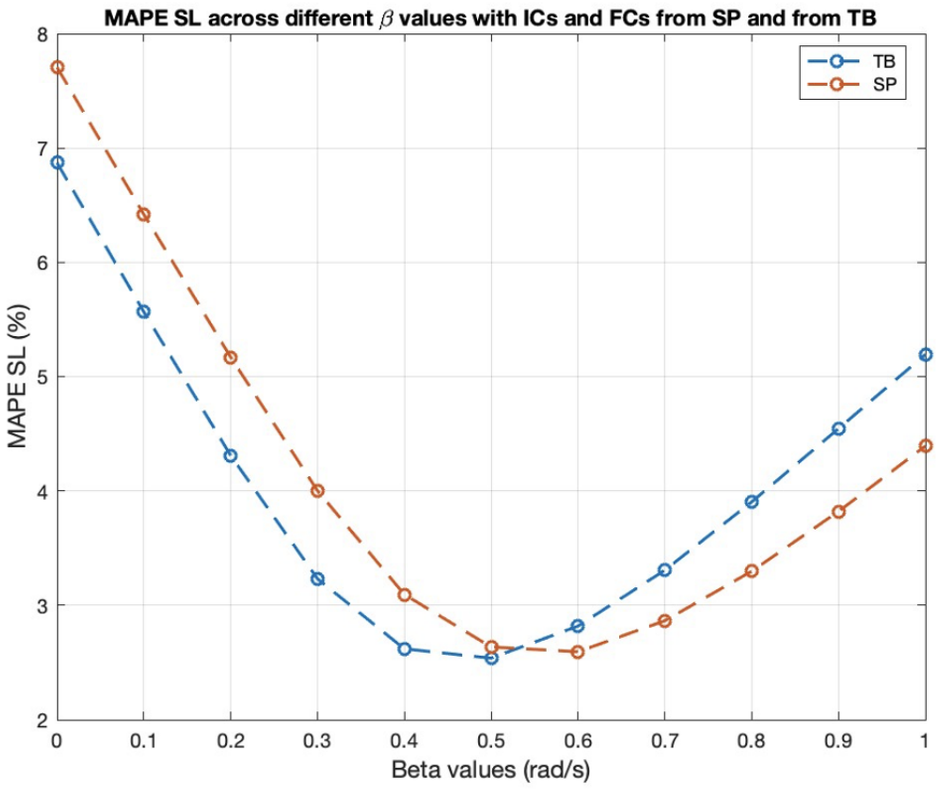

Fig. 4.16 Tuning performed over moderate-speed dataset both with contacts defined from template-based method and from reference system.

Table 4.7 Performance evaluation with the sub-optimal beta values both for results from template-based (TB) ICs and FCs detection method and for stereophotogrammetry-based (SP) method. All the results are proposed as median value ± IQR.

Sub-optimal Beta value (rad/s)	**Speed**	**Condition**	**MAPE SV, %**	**MAPE SL, %**
0.51	14 km/h	TB	2.63 ± 1.52	2.53 ± 1.77
0.60	14 km/h	SP	3.11 ± 1.27	2.59 ± 1.50

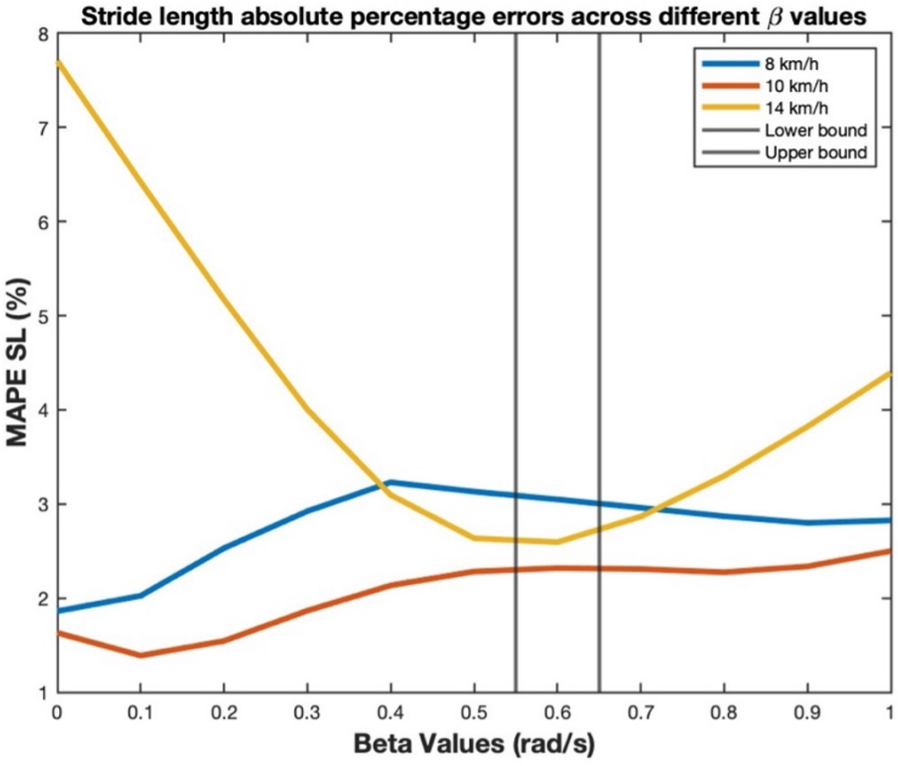

Fig. 4.17 Different error distributions across various beta values for different speeds for contacts and integration instants from reference systems. The vertical lines indicate the boundaries within which the error distributions show no statistically significant difference between speeds.

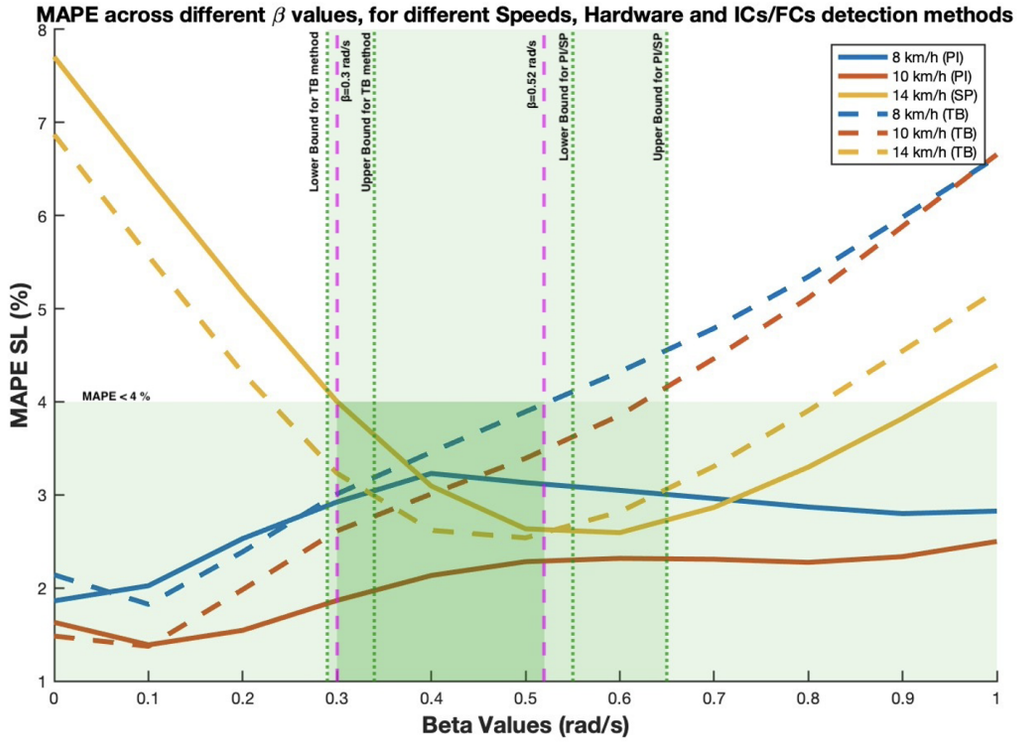

Fig. 4.18 Percentage errors on SL across different β values for different speeds, hardware, and ICs/FCs detection methods. This final figure shows the acceptance area under 4 %, as well as the lower and upper bounds within which the estimates are not speed-dependent, both for reference detection methods (SP, PI) and for TB. Additionally, the pink dashed lines indicate the range between 0.3 rad/s and 0.52 rad/s, chosen as a general interval to be proposed regardless of hardware, implemented methods, and speed.

As a general statement, it can be observed that the results in term of MAPE over SL and SV are comparable to those obtained with the template-based method (TB) and the parametric ZUPT detector method. It can be also observed that the optimal beta value is always higher than the one chosen with the TB method (0.08 rad/s compared to 0.1 rad/s and 0.51 rad/s compared to 0.6 rad/s). This allowed us to conclude that increasing the accuracy in selecting integration instants does not affect the SL error but rather impacts the optimal β values. Therefore, it was necessary to investigate why this occurs and whether it depends on the fact that the reference-selected instant is characterized by an acceleration closer to zero.
Indeed, this could justify the choice of a higher β value, since increasing β gives more weight to the correction based on the accelerometer and, if present, the magnetometer, at the expense of the estimation based on the gyroscope.

First, the accelerometric norm was calculated for each trial at each speed. It was observed that, in general, the integration instants selected by the TB method anticipate those from the reference system by an average of 5 samples. An example is provided in Figure 4.19.
Furthermore, it was observed that the accelerometric norm was not lower at the reference-selected instant. However, it was found that the mean value of the accelerometric norm was instead lower when considering the average between two consecutive integration instants. The graphical result for a specific subject and trial is shown in Figure 4.20.

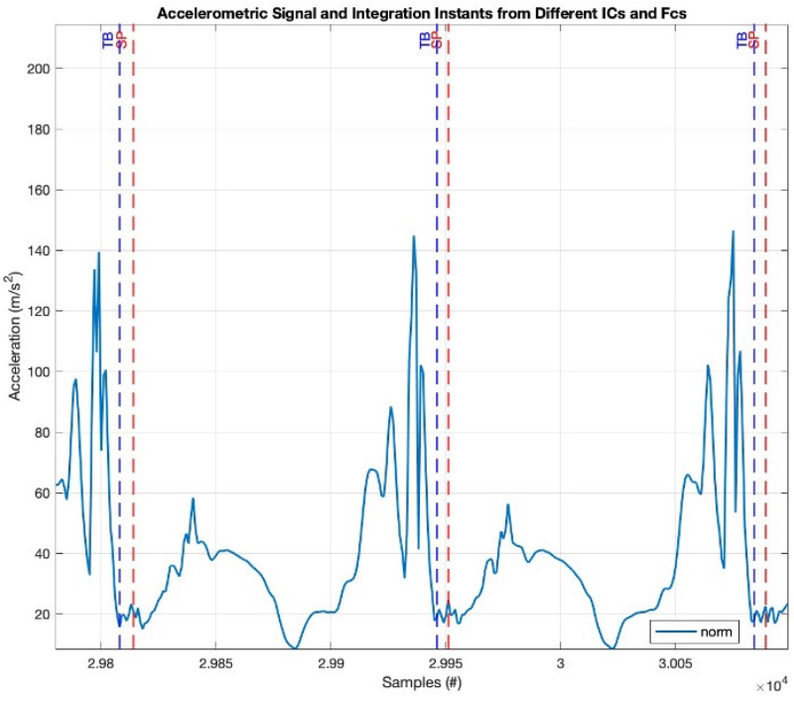

Fig. 4.19 Accelerometric norm of a subject running at 14 km/h. This figure highlights the differences in integration instant selection between the two methods.

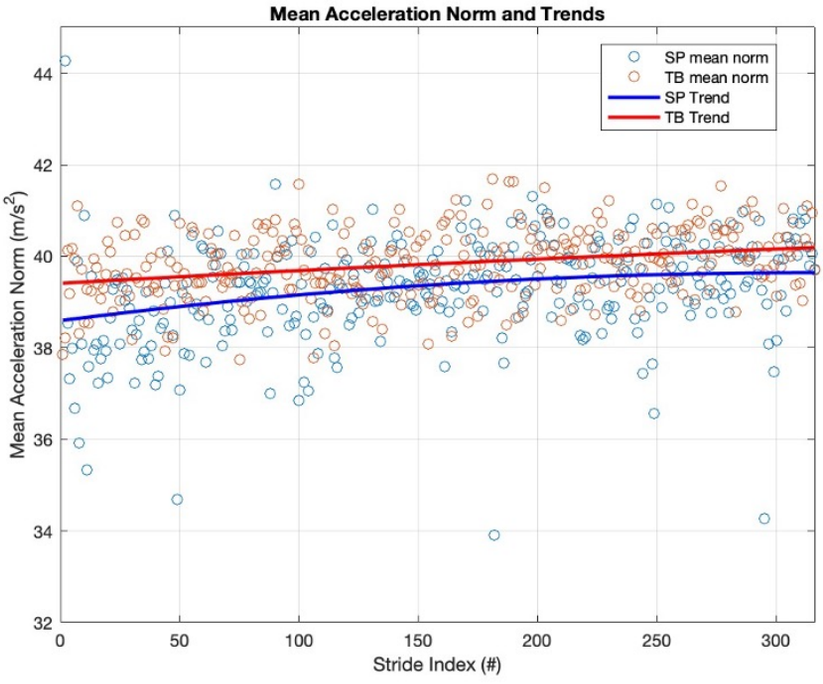

Fig. 4.20 Mean of accelerometric norm stride-by-stride for a subject running at 14 km/h.

4.1.3 Influence of Quaternion Initialization

Once a suitable range for estimating SL and SV across different running speeds, hardware, and estimation methods was defined and proposed, the influence of stride-by-stride re-initialization, as suggested by Valenti [17], at each zero velocity instant (or integration instant) was analyzed. This analysis aimed to determine whether the drift introduced by the gyroscope has a greater impact on estimation errors compared to stride-by-stride re-initialization, where selecting integration instants close to zero can be imprecise due to the dynamic nature of the movement. The following section presents two examples: one where drift remains limited even without re-initialization (Figure 4.21) and another where re-initialization is crucial for reducing drift (Figure 4.23).

In the first case, stride-by-stride quaternion re-initialization appears to worsen the quaternion estimation throughout the trial, reducing its reproducibility and periodicity, as observed in Figure 4.22. Conversely, when drift is high without re-initialization, the stride-by-stride approach helps stabilize the estimates (Figure 4.24). To assess whether re-initialization is optimal in both cases, the computed displace-

ments with and without stride-by-stride re-initialization were compared to reference displacements obtained from stereophotogrammetry. It was observed that, regardless of whether re-initialization worsened the quaternion estimation or effectively reduced drift, the estimation of displacement and step length (SL) improved (Figures 4.25 and 4.26). This led us to conclude that, in general, re-initialization enhances the estimates. Therefore, for the remainder of the analysis, this technique was adopted across all datasets and proposed methods.

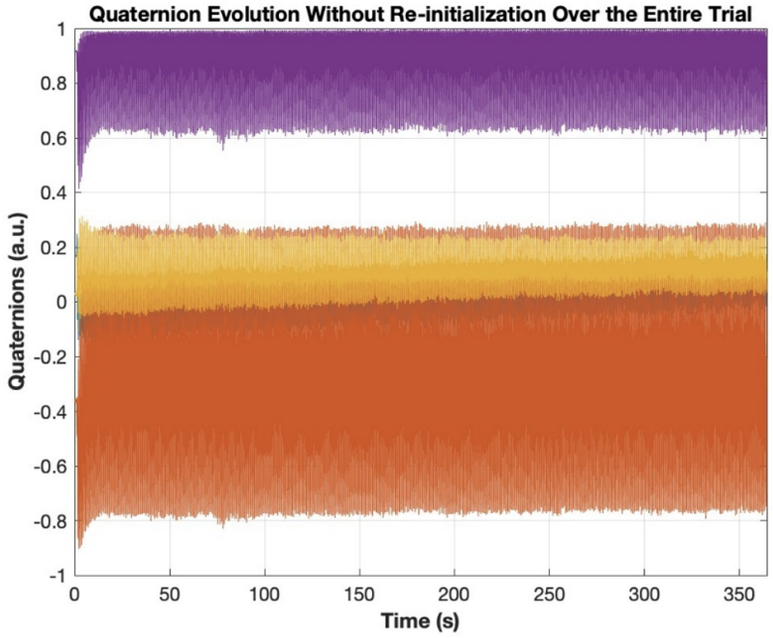

Fig. 4.21 Quaternion evolution without re-initialization over an entire trial.

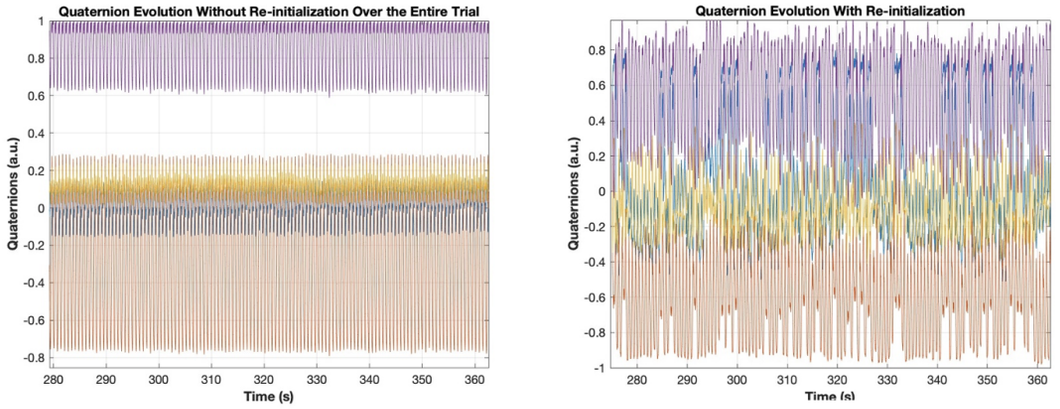

Fig. 4.22 Quaternion evolution without re-initialization on the left, quaternion evolution with re-initialization on the right.

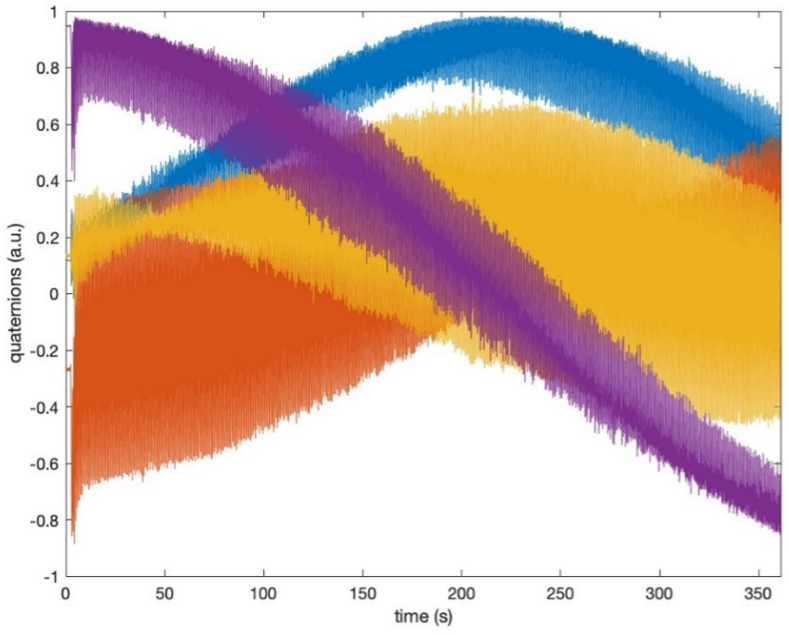

Fig. 4.23 Quaternion evolution without re-initialization over an entire trial.

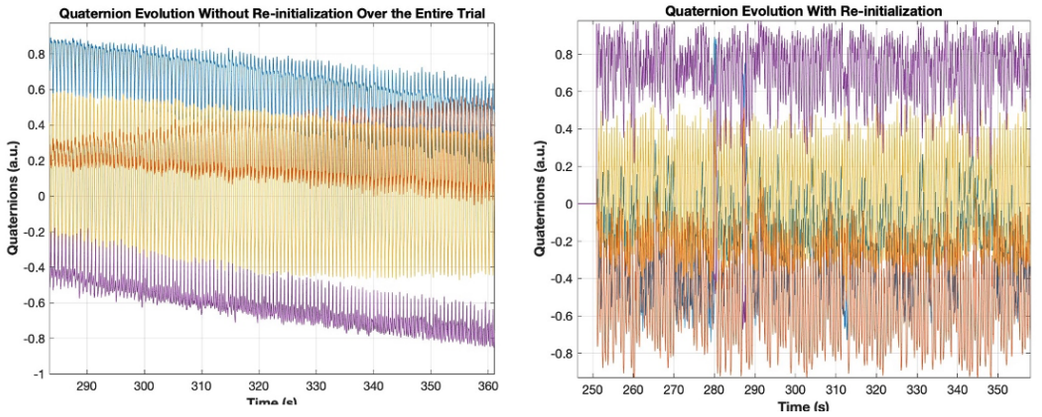

Fig. 4.24 Quaternion evolution without re-initialization on the left, quaternion evolution with re-initialization on the right.

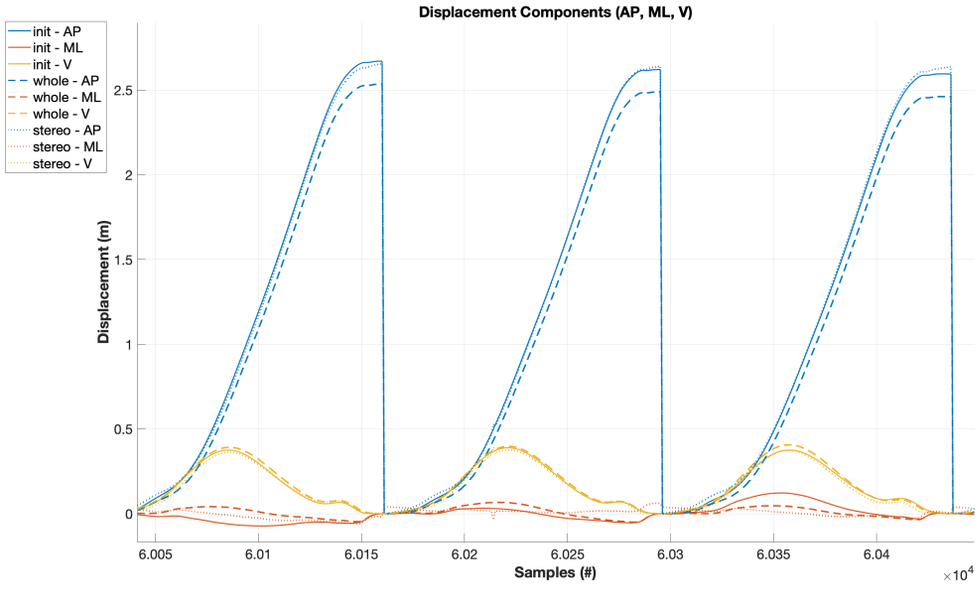

Fig. 4.25 Displacements along the three axes computed with (continuous line) and without (dashed line) reinitialization, compared to the reference (dotted line). Case where whole-trial quaternions remain stable without reinitialization.

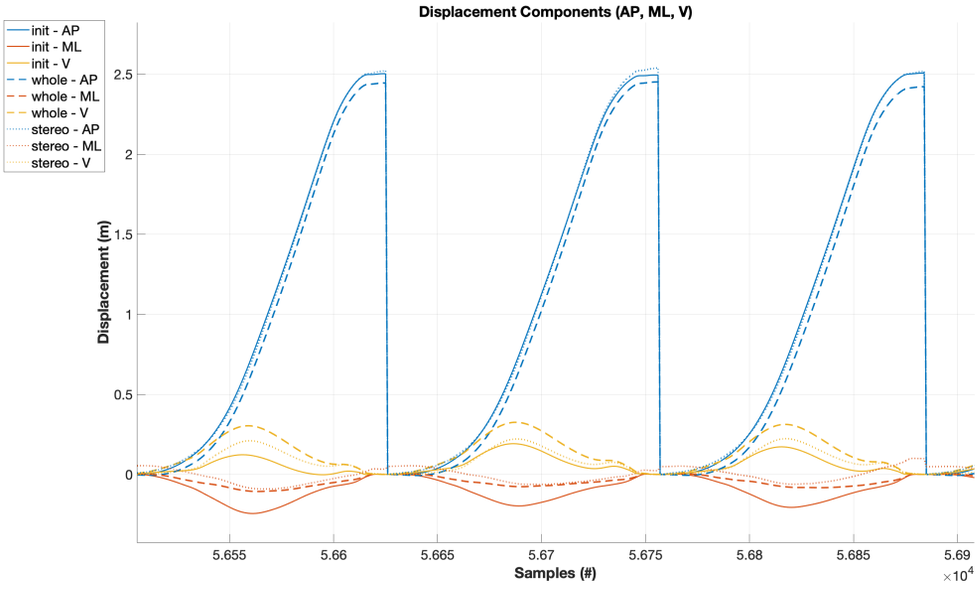

Fig. 4.26 Displacements along the three axes computed with (continuous line) and without (dashed line) reinitialization, compared to the reference (dotted line). Case where whole-trial quaternions has a drift without reinitialization.

4.2 Stride Length and Stride Velocity Results using the Proposed Framework

In the following sections, the results obtained from the framework implementation, which automatically selects the optimal β parameter stride-by-stride without prior tuning, are presented. The performance variations depending on the different implemented objective functions (described in Section 3.3) and the number of optimized variables is discussed below.

4.2.1 Cost Function Minimizing Stride-by-Stride Stride Length and Stride Velocity Errors

In this section, the results obtained using the cost function that minimizes SL and SV errors stride-by-stride are presented. Firstly, performance across the two datasets was evaluated using a single optimization variable. These initial tuning steps were carried out to assess the feasibility of the method and determine the best optimization configuration. Specifically, the maximum number of iterations per stride was set to 1000 and the number on multistart was set to 10, as increasing these values did not lead to significant improvements but instead worsened performance in terms of computational time. Once the optimization framework parameters were properly set and the results were obtained in terms of SL and SV errors, the number of discarded strides, and the computational time for a single optimization variable, the next step was to investigate whether increasing the number of variables (by integrating the sensor bias parameters) could further improve performance without excessively deteriorating computational efficiency.

One Optimization Variable

Table 4.8 shows the results obtained across different datasets. Once it was confirmed that the performance yielded significantly better results in terms of SV estimation and comparable results for SL, the analysis was extended to ensure that the reduction in errors did not lead to a deterioration of the physical output in terms of displacement signal reconstruction. Additionally, the stride-by-stride distribution of beta values was analyzed to assess whether all assumed beta values were admissible.

Table 4.8 Performance evaluation across different datasets with the 1 optimized variable framework proposed. All the results are proposed as median value ± IQR.

Dataset	MAPE SV (%)	MAPE SL (%)	Number of strides	Unreliable strides (%)	Computation time for 1 stride (s)
8 km/h	0.8 ± 0.6	2.6 ± 2.4	16911	0	0.3 ± 0.1
10 km/h	0.8 ± 0.4	3.6 ± 4.3	15372	0	0.3 ± 0.1
14 km/h	0.8 ± 0.3	1.6 ± 0.5	21430	0	0.3 ± 0.1

Slow-Speed Dataset

Figures 4.27 and 4.28 show the occurrences of beta across the entire low-speed dataset and the distribution of beta for each subject. It can be observed that the majority of beta values fall within the range of 0–0.1 rad/s. The distribution decreases progressively but increases again in the 0.9–1 rad/s range. The analysis of the admissibility of the strides in this range is presented in Section 4.2.2. Furthermore, it can be observed that the distribution of the governing parameter is homogeneous across different subjects.

On the other hand, Figures 4.29 and 4.30 show the differences in error distributions between the pipeline that uses a single beta value and the pipeline with the framework. It can be observed that, for both metrics, lower errors are achieved with the framework, while the standard deviation associated with errors in the stride-by-stride optimization method remains high but constant.

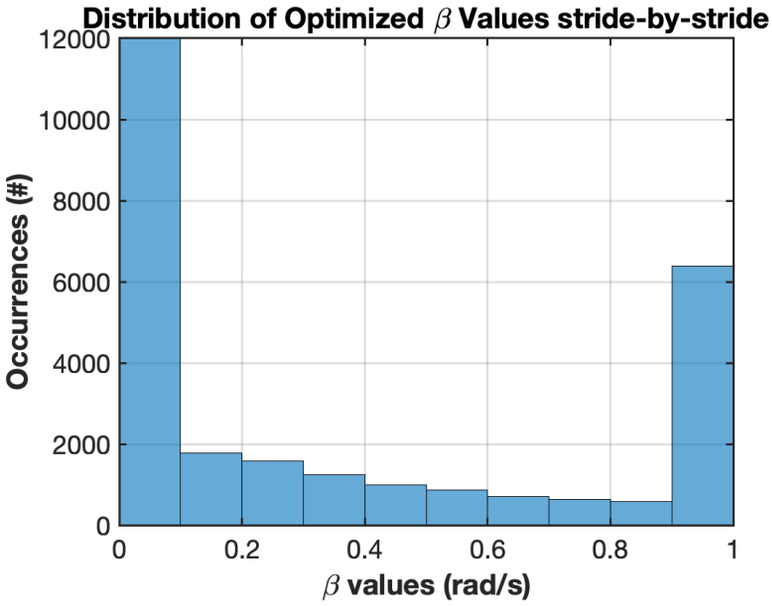

Fig. 4.27 Occurrences of stride-by-stride beta values for the entire slow-speed dataset.

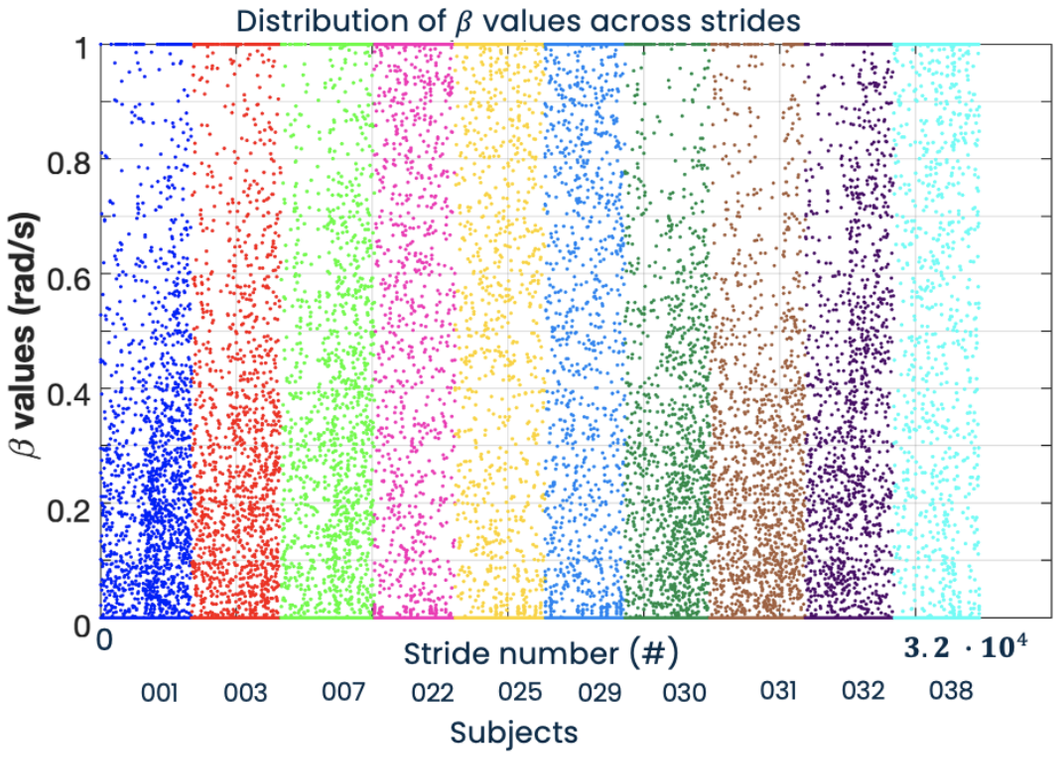

Fig. 4.28 Beta Distribution for each subject of the slow-speed dataset.

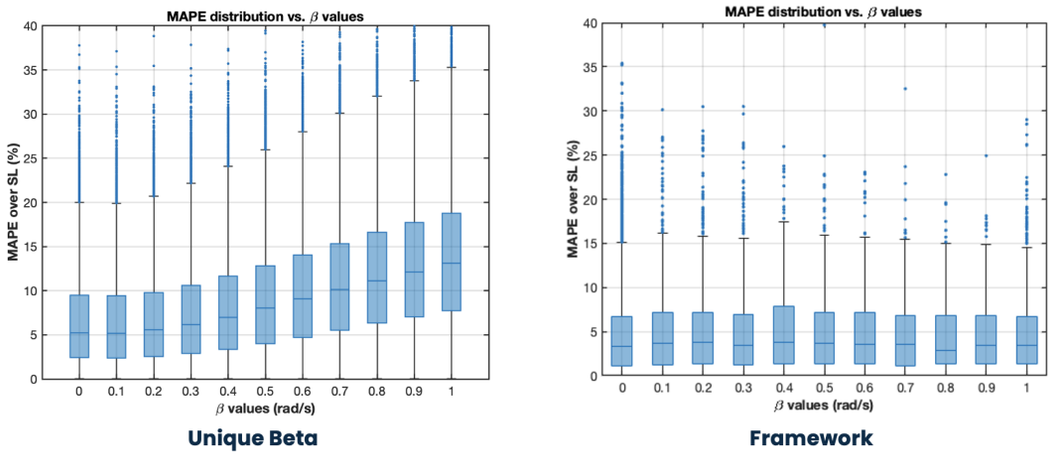

Fig. 4.29 The left graph shows the distributions of SL errors as a function of beta when using a single beta value across the entire dataset, while the right graph illustrates the error distribution as a function of beta when using the framework.

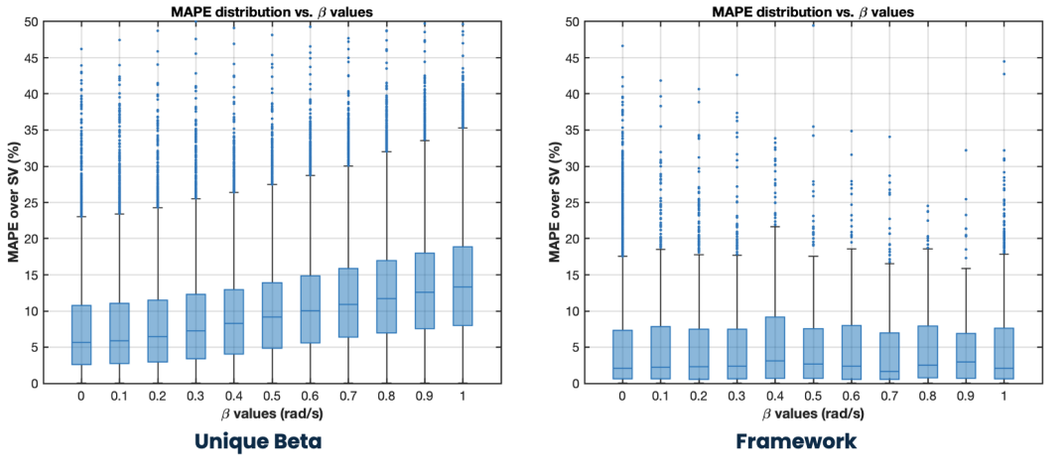

Fig. 4.30 The left graph shows the distributions of SV errors as a function of beta when using a single beta value across the entire dataset, while the right graph illustrates the error distribution as a function of beta when using the framework.

Moderate-Speed Dataset

As for the Slow-Speed Dataset, the occurrences of beta across the Moderate-Speed dataset and the distributions divided for subject are reported in Figures 4.31 and 4.32. In this case, the distribution of β values reaches its peak within the range of 0.3 to 0.4 rad/s. Similarly, an increase in occurrences is also observed in the 0.9 to 1 rad/s range.

Regarding the error distributions shown in Figures 4.33 and 4.34, this dataset also exhibits lower errors for both metrics, with contained standard deviations.

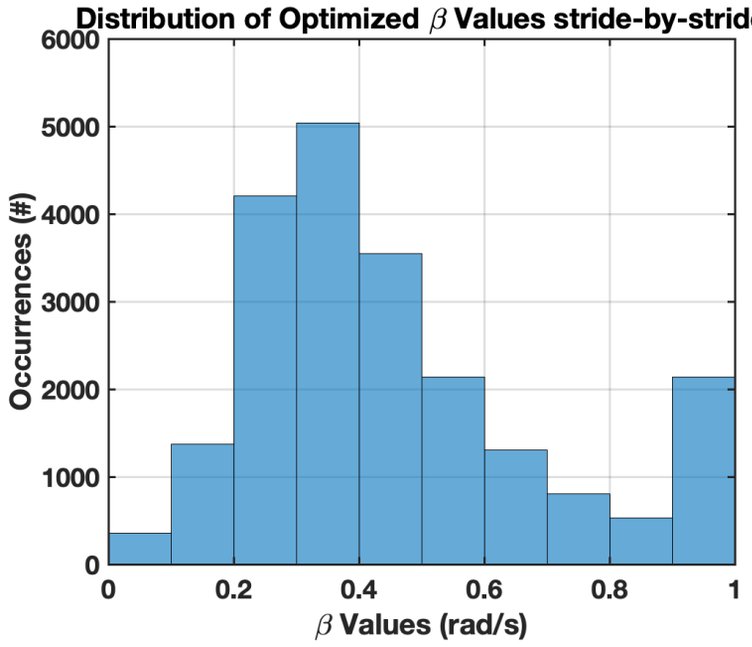

Fig. 4.31 Occurrences of stride-by-stride beta values for the enire moderate-speed dataset.

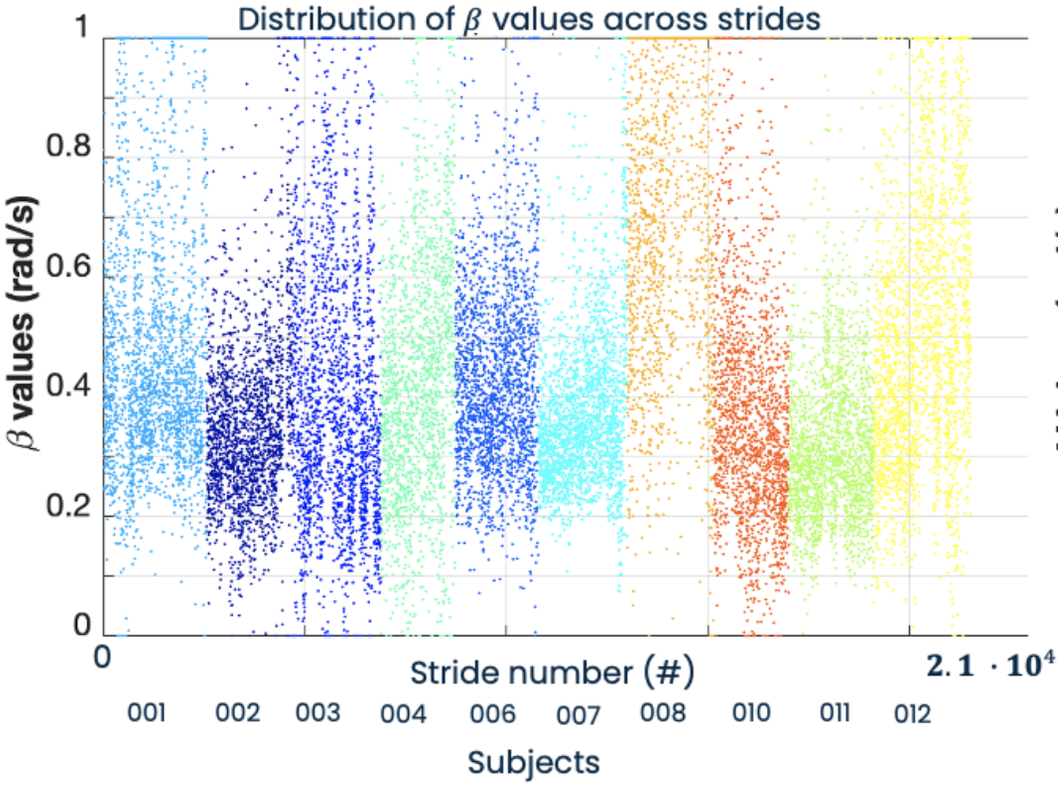

Fig. 4.32 Beta Distribution for each subject of the moderate-speed dataset.

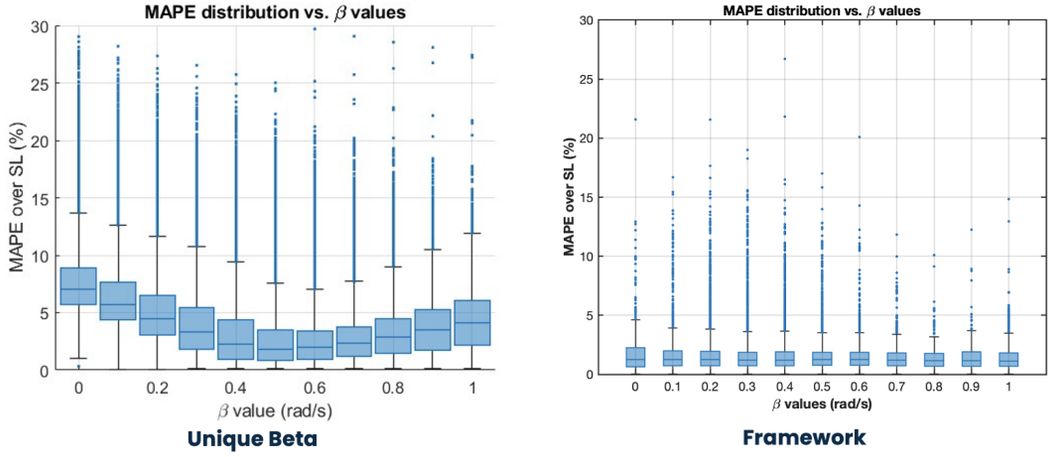

Fig. 4.33 The left graph shows the distributions of SL errors as a function of beta when using a single beta value across the entire dataset, while the right graph illustrates the error distribution as a function of beta when using the framework.

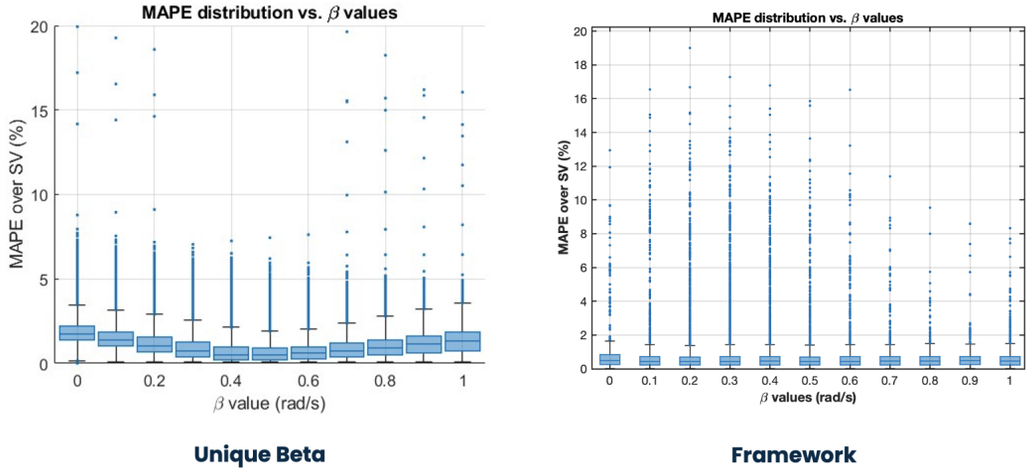

Fig. 4.34 The left graph shows the distributions of SV errors as a function of beta when using a single beta value across the entire dataset, while the right graph illustrates the error distribution as a function of beta when using the framework.

Seven Optimization Variables

Table 4.9 shows the results obtained across different datasets with seven different optimization variables. A comparison with Table 4.8 reveals that the results on the low-speed dataset lead to a significant improvement in SL, reducing the error by 1.7% for running at 8 km/h and 2.7% for running at 10 km/h. At 14 km/h, the error remains comparable between the optimization with one and seven variables. However, this comes at the cost of a significant deterioration in computational performance, reaching up to one second of processing time per single stride.

Table 4.9 Performance evaluation across different datasets with the 7 optimized variables framework proposed. All the results are proposed as median value $\pm$ IQR.

Dataset	**MAPE SV (%)**	**MAPE SL (%)**	**Number of strides**	**Unreliable strides (%)**	**Computation time for 1 stride (s)**
8 km/h	0.2 ± 0.1	0.9 ± 0.4	16911	0	1.18 ± 0.12
10 km/h	0.3 ± 0.1	0.9 ± 0.3	15372	0	1.18 ± 0.12
14 km/h	0.2 ± 0.3	1.5 ± 0.4	21430	1	0.96 ± 0.05

Slow-Speed Dataset

Figures 4.35 and 4.36 show the occurrences of beta values across the entire low-speed dataset and the distribution of beta for each subject. It can be observed that the majority of beta values fall within the range of 0–0.1 rad/s. The distribution decreases progressively but increases again in the 0.9–1 rad/s range, reaching almost the same number of occurrences of the range 0-0.1 rad/s. Furthermore, it can be observed that the distribution of the governing parameter is homogeneous across different subjects.

A further analysis was conducted on the six other variables to assess whether their variations influence the estimates. Figures 4.37 and 4.38 illustrate their distribution across subjects. It can be observed that the accelerometer bias (Figure 4.38) is influential, as it is evenly distributed across subjects over the entire admissibility range, which was defined a priori based on the observation of static acceleration after gravity removal. In contrast, the gyroscope bias (Figure 4.37) is less evenly distributed within the admissibility range.

On the other hand, Figures 4.39 and 4.40 show the differences in error distributions between the pipeline that uses a single beta value and the pipeline with the framework. It can be observed that, for both metrics, lower errors are achieved with the framework together with lower standard deviations, ensuring more accurate estimates.

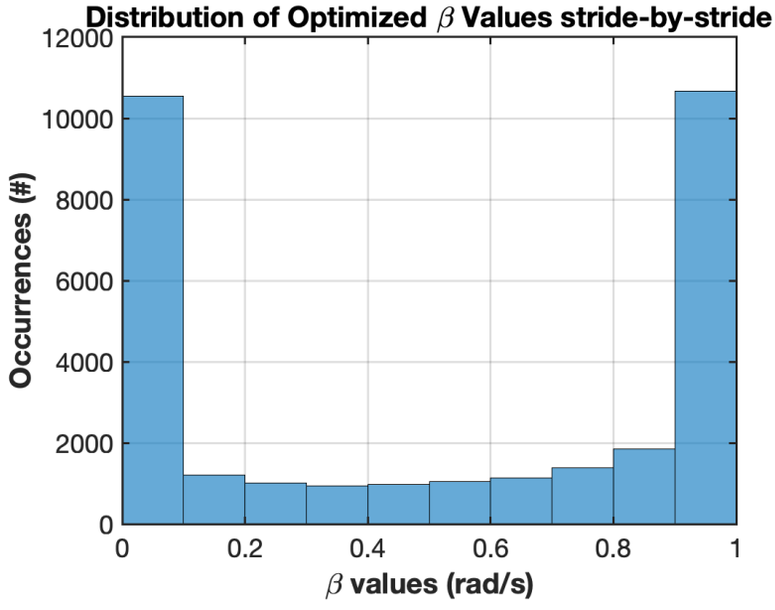

Fig. 4.35 Occurrences of stride-by-stride beta values for the entire slow-speed dataset.

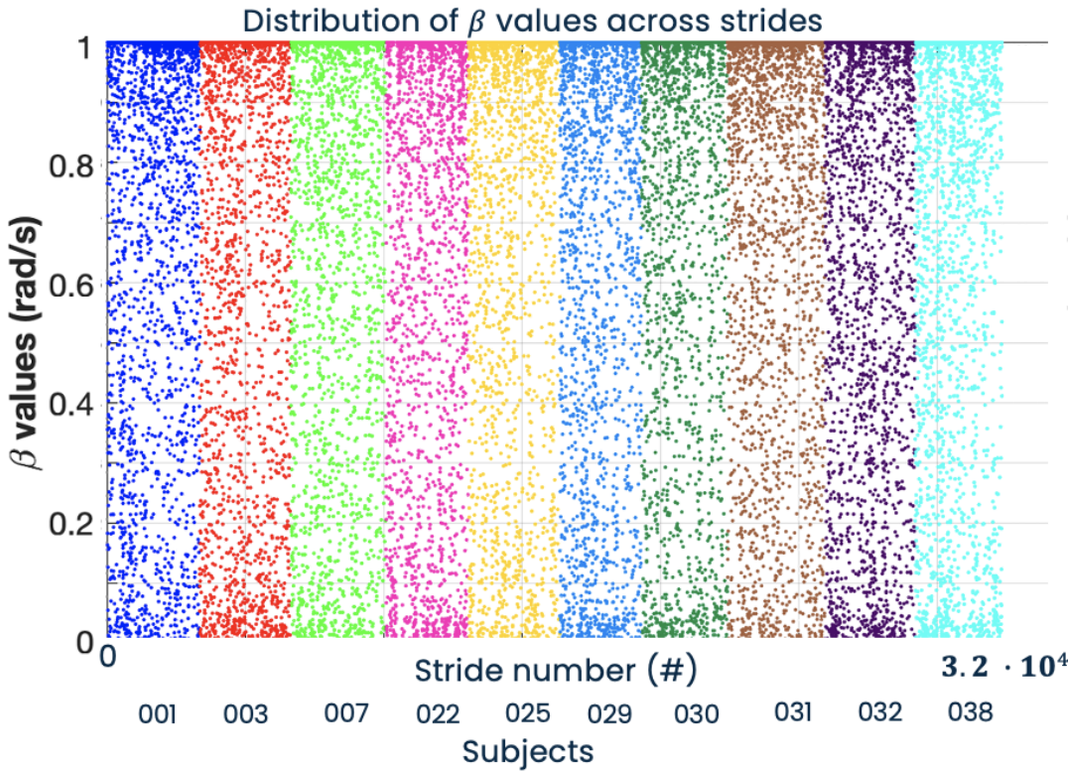

Fig. 4.36 Beta Distribution for each subject of the slow-speed dataset.

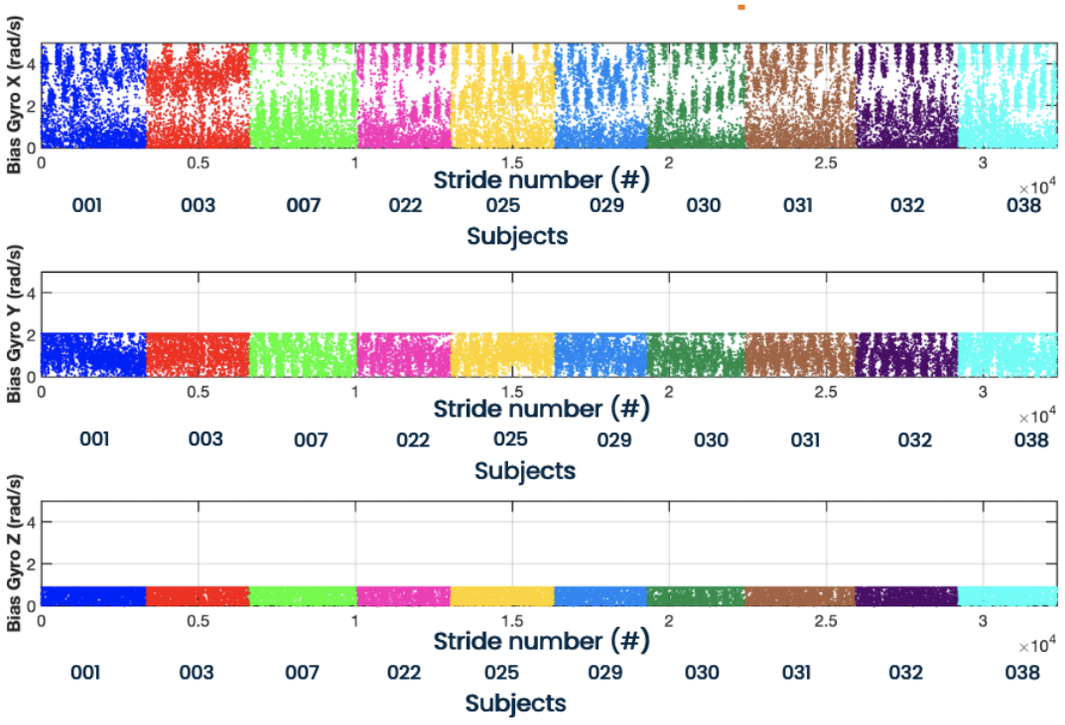

Fig. 4.37 Gyroscope bias distributions across subjects for the whole slow-speed dataset.

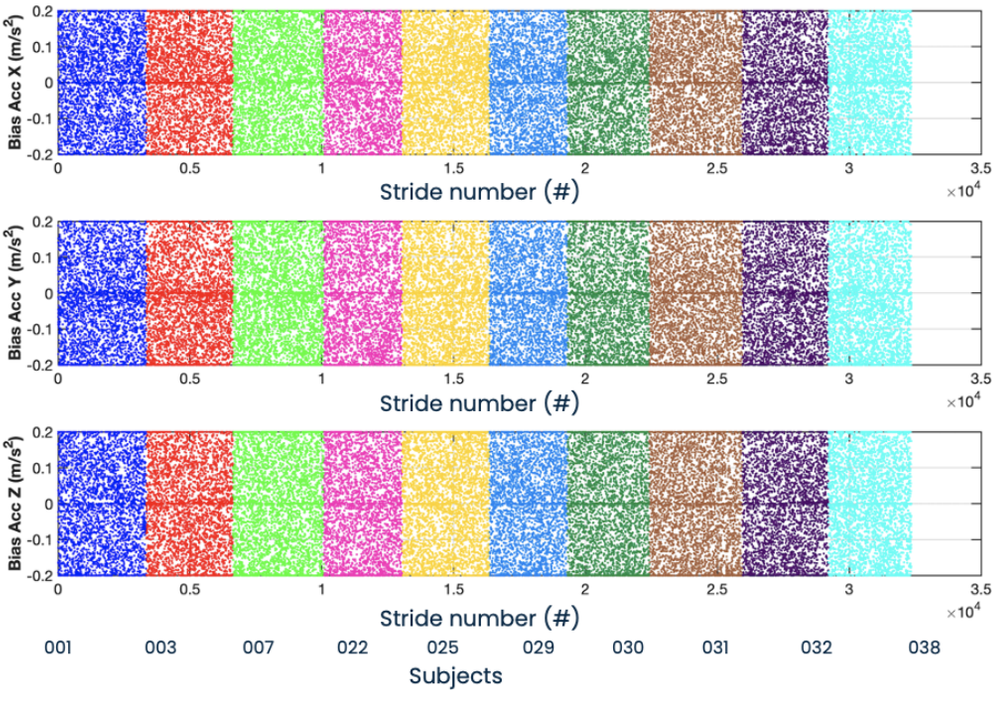

Fig. 4.38 Accelerometer bias distributions across subjects for the whole slow-speed dataset.

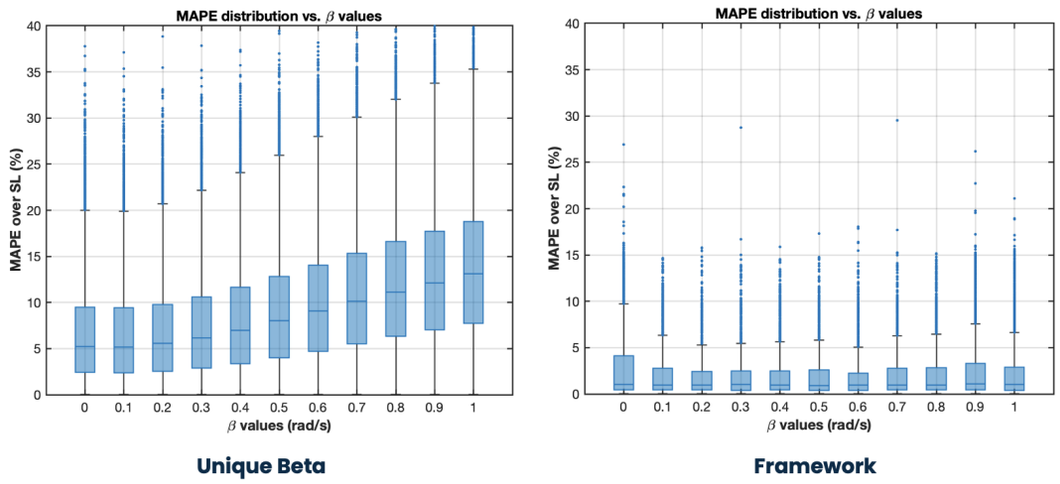

Fig. 4.39 The left graph shows the distributions of SL errors as a function of beta when using a single beta value across the entire dataset, while the right graph illustrates the error distribution as a function of beta when using the framework.

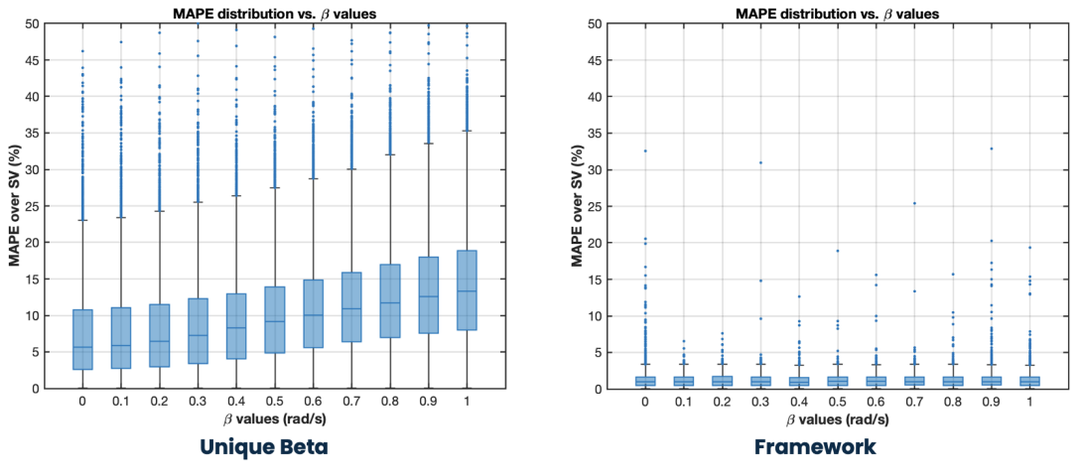

Fig. 4.40 The left graph shows the distributions of SV errors as a function of beta when using a single beta value across the entire dataset, while the right graph illustrates the error distribution as a function of beta when using the framework.

Moderate-Speed Dataset

As for the Slow-Speed Dataset, the occurrences of beta across the Moderate-Speed dataset and the distributions divided for subject are reported in Figures 4.31 and 4.32. In this case, the distribution of β values reaches its peak within the range of 0.3 to 0.5 rad/s. Similarly, an increase in occurrences is also observed in the 0.9 to 1 rad/s range.

The analysis conducted on the six additional variables to be optimized confirms that, even for this dataset, the accelerometer bias has a greater influence than the gyroscope bias.
Also in this case, it can be observed that the errors on SL and SV are lower than those obtained with the single beta, characterized by contained and stable standard deviations.

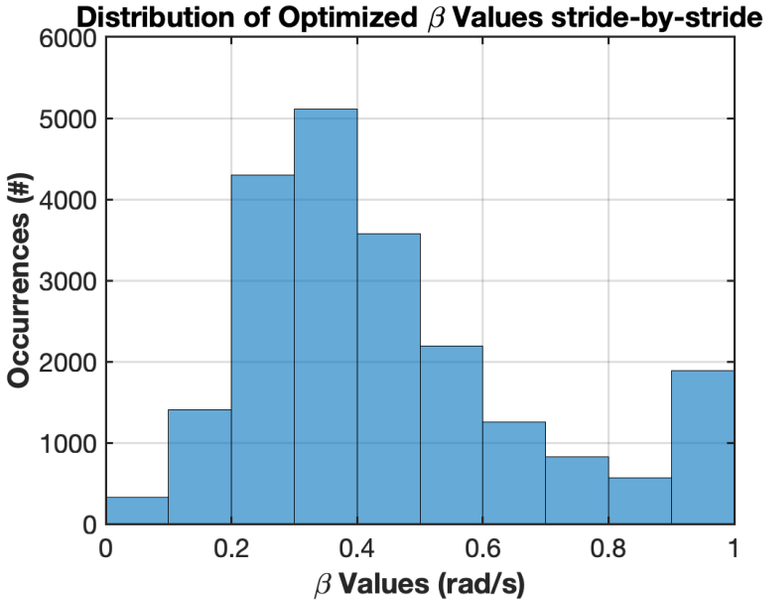

Fig. 4.41 Occurrences of stride-by-stride beta values for the entire moderate-speed dataset.

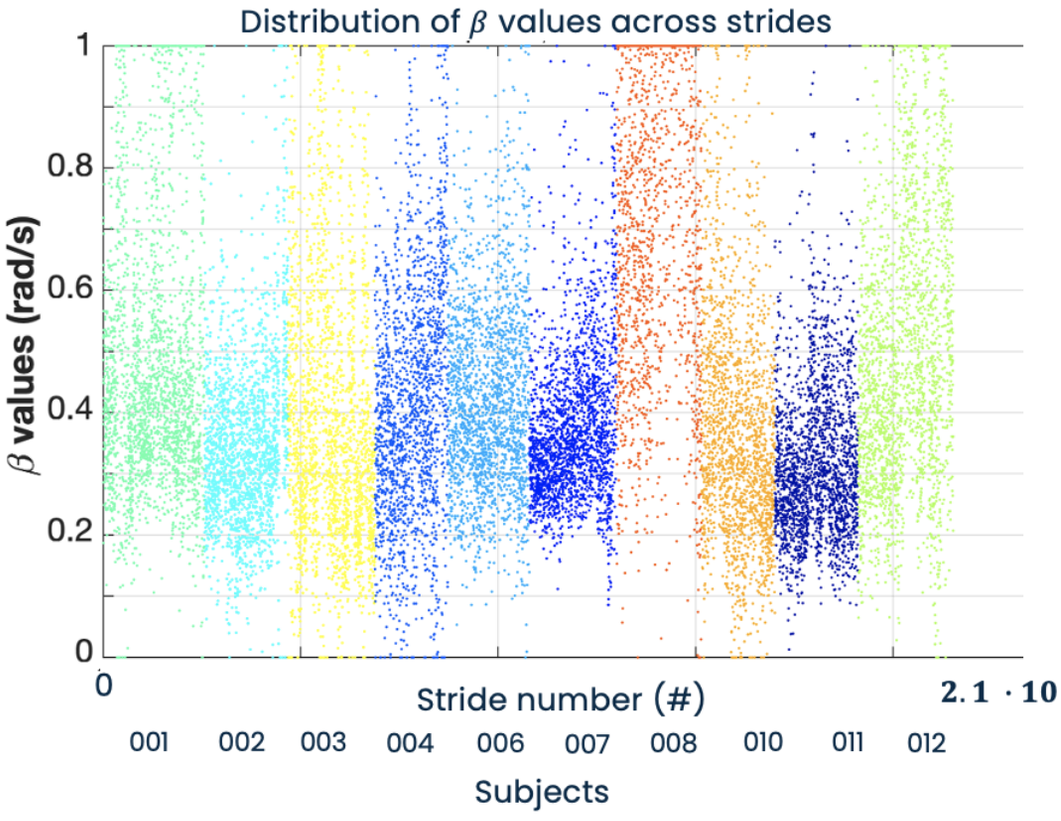

Fig. 4.42 Beta Distribution for each subject of the moderate-speed dataset.

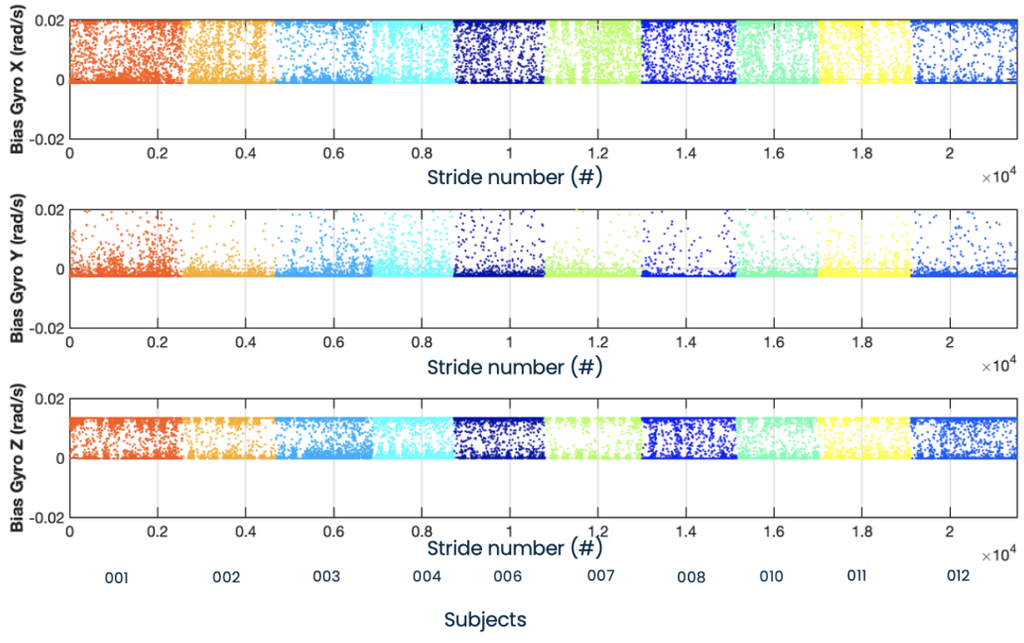

Fig. 4.43 Gyroscope bias distributions across subjects for the whole moderate-speed dataset.

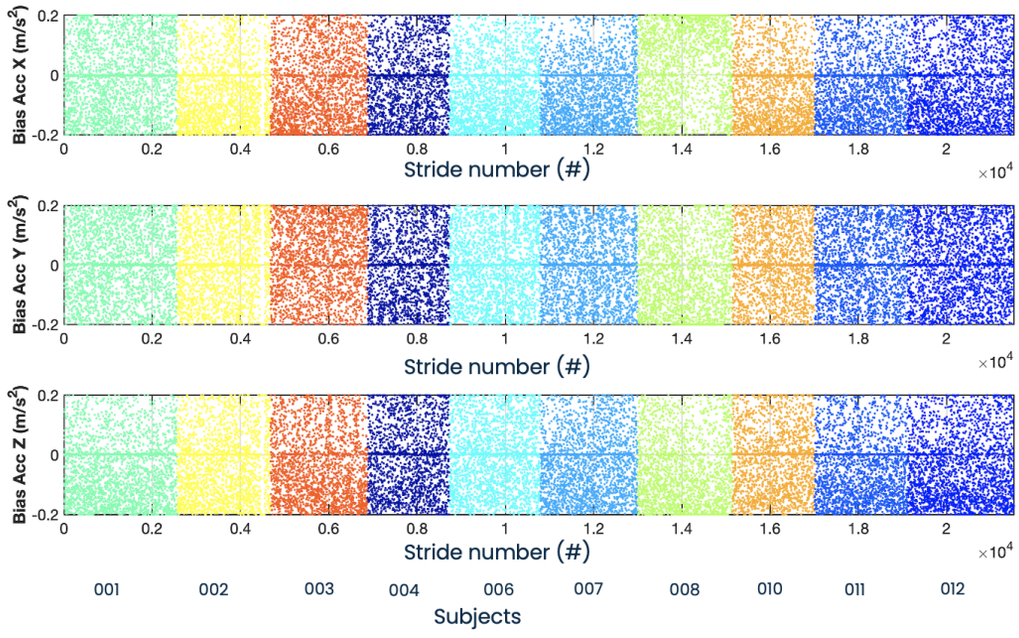

Fig. 4.44 Accelerometer bias distributions across subjects for the whole moderate-speed dataset.

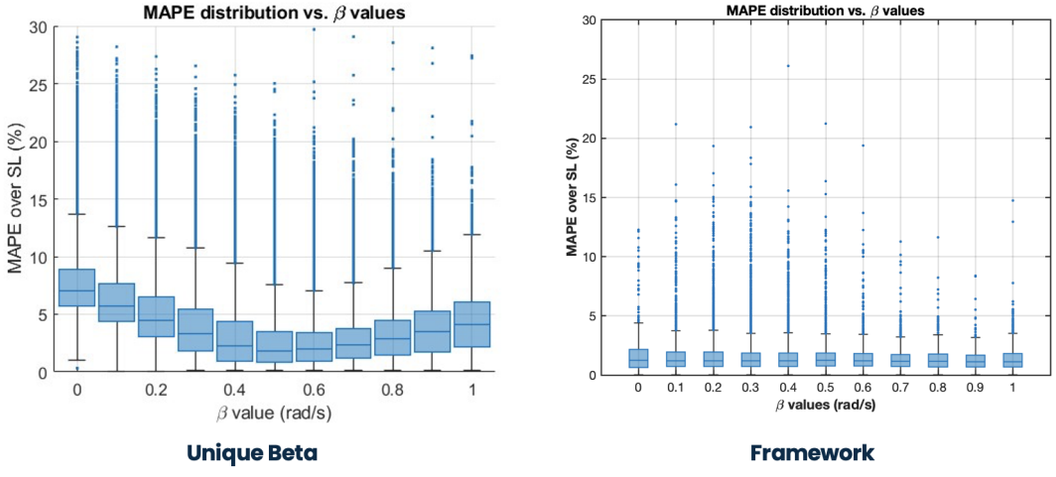

Fig. 4.45 The left graph shows the distributions of SL errors as a function of beta when using a single beta value across the entire dataset, while the right graph illustrates the error distribution as a function of beta when using the framework.

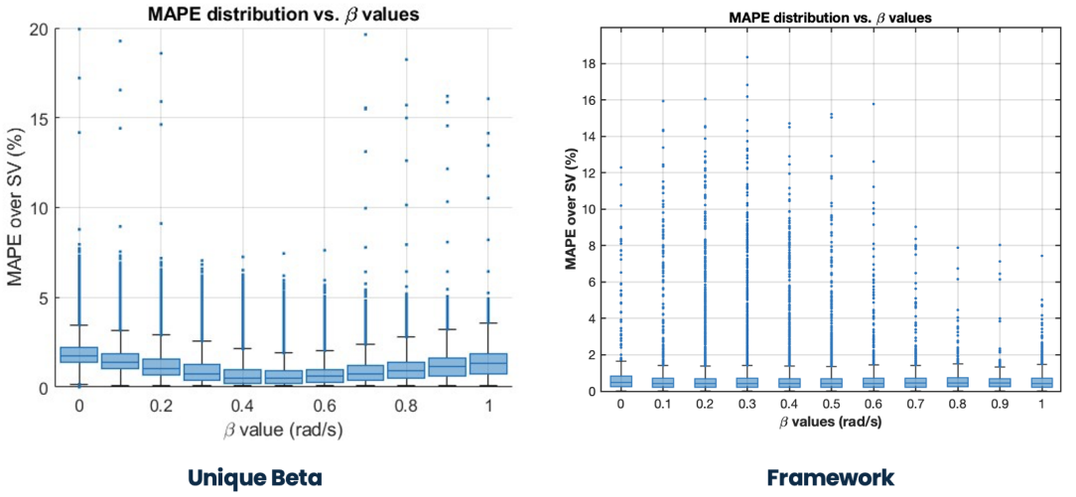

Fig. 4.46 The left graph shows the distributions of SV errors as a function of beta when using a single beta value across the entire dataset, while the right graph illustrates the error distribution as a function of beta when using the framework.

4.2.2 Admissibility of Strides When β Reaches its Upper or Lower Bound

This section presents the results of the exploratory analysis aimed at verifying that, although the β values associated with each stride vary significantly, the biomechanical meaning of the reconstructed displacement remains unaffected. Specifically, the analysis focuses on the two extreme cases of the governing parameter: 0 rad/s and 1 rad/s. Figures 4.47 and 4.49 show some specific strides over a single subject, highlighting some strides were beta=1 rad/s and 0 rad/s.

In general, it is observed that for extreme β values, the AP component of the signal closely matches the displacement obtained from the reference. However, the ML and V components exhibit significant errors, both in comparison to the reference and to the results obtained with a single β. In particular, the medio-lateral component appears to be forced into two waveform patterns that differ significantly from the correct ones.

In general, however, the errors obtained with the selected β values (1 rad/s for Figure 4.48 and 0 rad/s for Figure 4.50) are minimal within the framework, particularly at critical strides, compared to the corresponding results obtained with a single β.

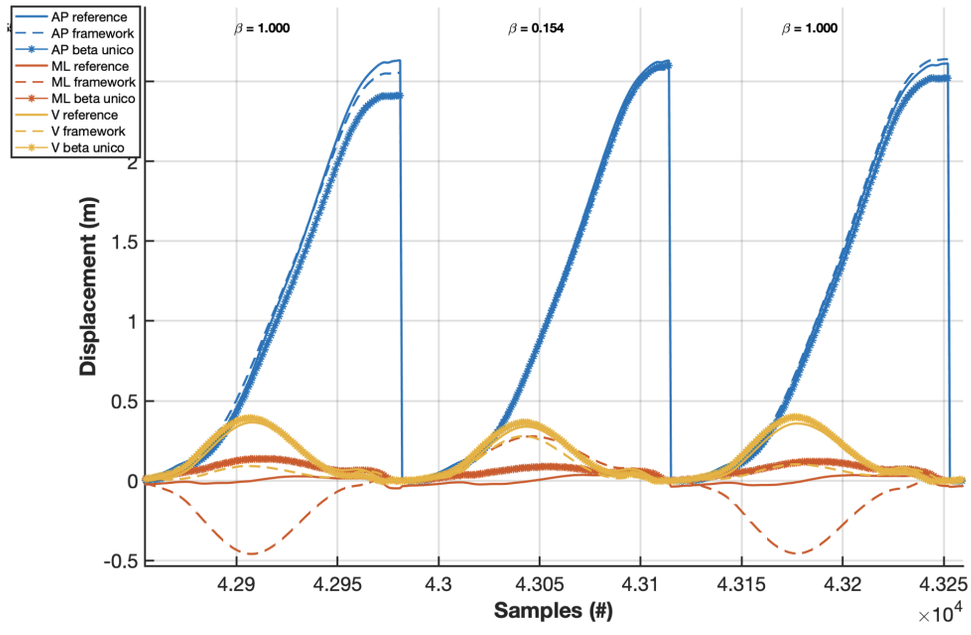

Fig. 4.47 Displacement along the three axes, obtained from the SP reference (continuous line), the calculation with a single β (dotted line), and the framework (dashed line), for a specific trial of a single subject running at 14 km/h. This plot highlights strides where the β value is equal to 1 rad/s.

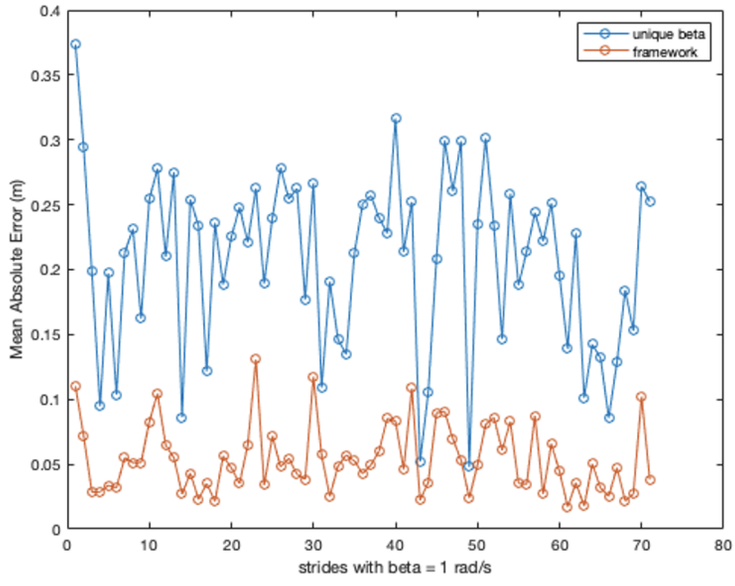

Fig. 4.48 Mean Errors computed on a specific trial for the same subject considered in Figure 4.47. This figure highlights the significant errors reduction when the chosen β value is 1 rad/s.

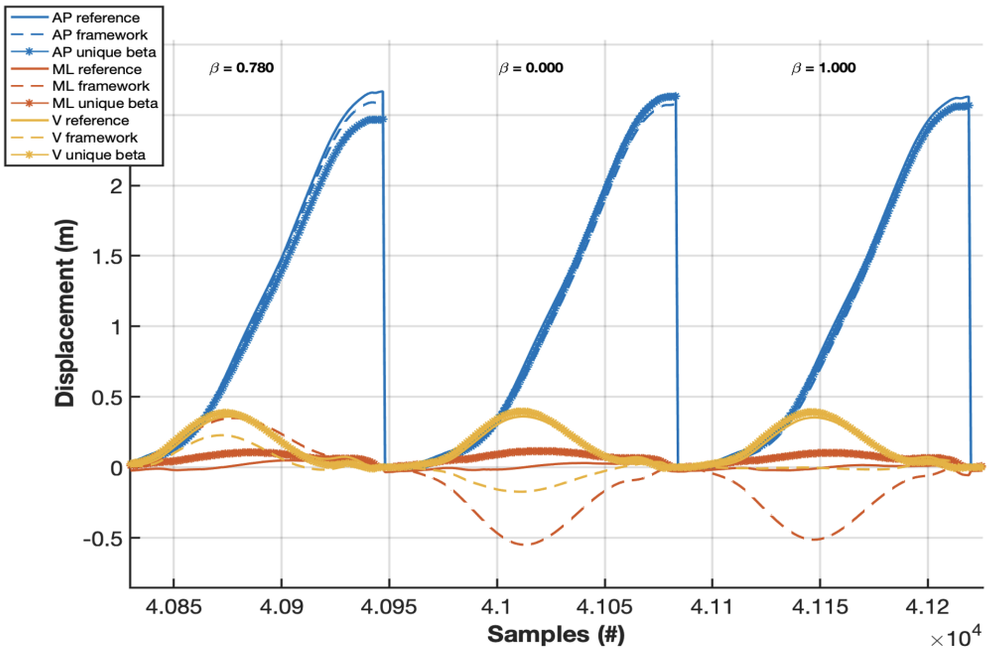

Fig. 4.49 Displacement along the three axes, obtained from the SP reference (continuous line), the calculation with a single β (dotted line), and the framework (dashed line), for a specific trial of a single subject running at 14 km/h. This plot highlights a stride where the β value is equal to 0 rad/s.

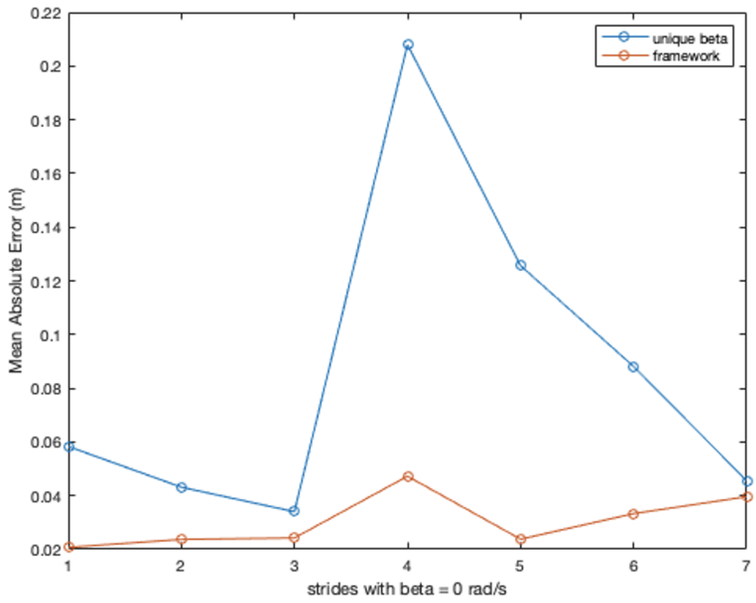

Fig. 4.50 Mean Errors computed on a specific trial for the same subject considered in Figure 4.49. This figure highlights the significant errors reduction when the chosen β value is 0 rad/s.

4.2.3 Cost Functioin Exploiting Biomechanical Constraints

The results obtained from the tests conducted on both datasets are presented below, using the framework with one and seven variables. In this case, the objective function is independent from the gold standard measurements and instead relies on biomechanical constraints specific to running motion, as explained in Section 3.3.2. Tables 4.10 and 4.11 present the results obtained from tests conducted on both datasets using the framework with one and seven variables, respectively. In general, the errors observed in the slow-speed dataset are quite acceptable for SV, while they increase up to 5.5% for SL. Conversely, for the moderate-speed dataset, the error exceeds 4% for both parameters. Although these results are worse than the best ones obtained with a single beta value, they highlight a potential margin for improvement in the method. This is because these tests are preliminary and do not include validation steps or alternative evaluations of the objective function.
Figures 4.51, 4.52, 4.53 and 4.54 show errors distribution for each dataset and framework without gold standard proposed.

Table 4.10 Performance evaluation across different datasets with the one optimized variable framework proposed. All the results are proposed as median value $\pm$ IQR.

Dataset	MAPE SV (%)	MAPE SL (%)	Number of strides	Unreliable strides (%)	Computation time for 1 stride (s)
8 km/h	1.9 ± 2.4	5.1 ± 6.5	16911	0	0.13 ± 0.03
10 km/h	1.8 ± 2.3	5.0 ± 6.5	15372	0.03	0.13 ± 0.03
14 km/h	4.0 ± 1.6	4.7 ± 2.2	21430	0	0.22 ± 0.01

Table 4.11 Performance evaluation across different datasets with the 7 optimized variables framework proposed. All the results are proposed as median value $\pm$ IQR.

Dataset	MAPE SV (%)	MAPE SL (%)	Number of strides	Unreliable strides (%)	Computation time for 1 stride (s)
8 km/h	1.1 ± 0.9	3.7 ± 3.1	16911	0	0.65 ± 0.21
10 km/h	1.9 ± 1.4	5.4 ± 3.4	15372	0	0.65 ± 0.21
14 km/h	4.1 ± 1.7	4.9 ± 2.2	21430	1	0.38 ± 0.10

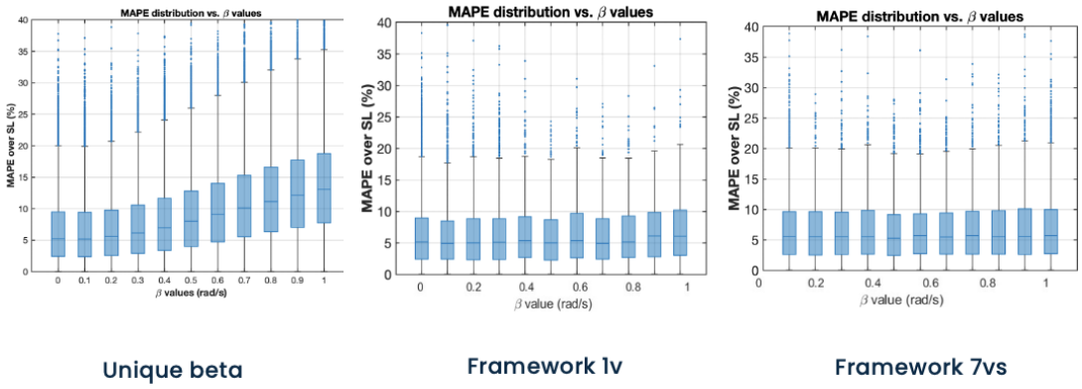

Fig. 4.51 This figure shows the error distributions obtained for SL using a single beta across the entire slow-speed dataset (on the left) and with the framework with 1 variable (in the center) and 7 variables (on the right) when the objective function does not involve reference measurements.

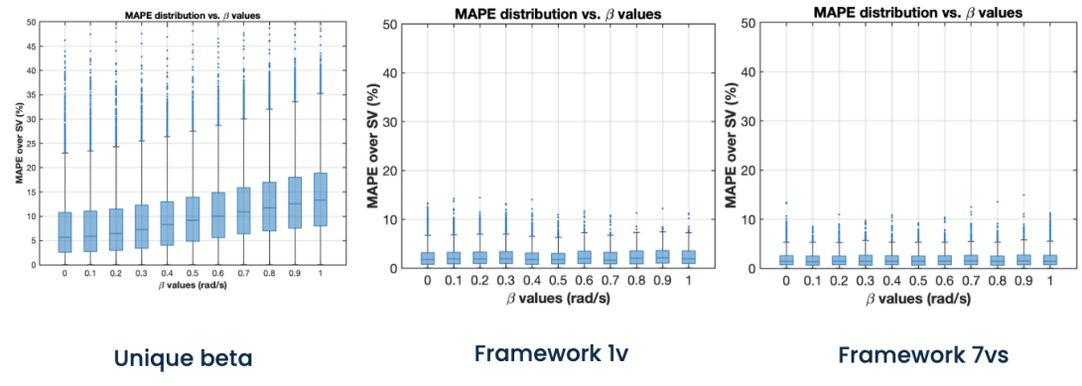

Fig. 4.52 This figure shows the error distributions obtained for SV using a single beta across the entire slow-speed dataset (on the left) and with the framework with 1 variable (in the center) and 7 variables (on the right) when the objective function does not involve reference measurements.

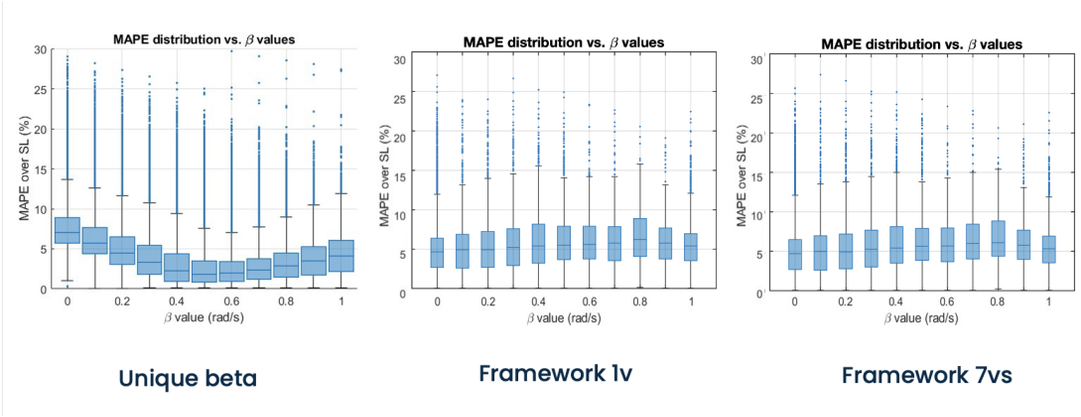

Fig. 4.53 This figure shows the error distributions obtained for SL using a single beta across the entire moderate-speed dataset (on the left) and with the framework with 1 variable (in the center) and 7 variables (on the right) when the objective function does not involve reference measurements.

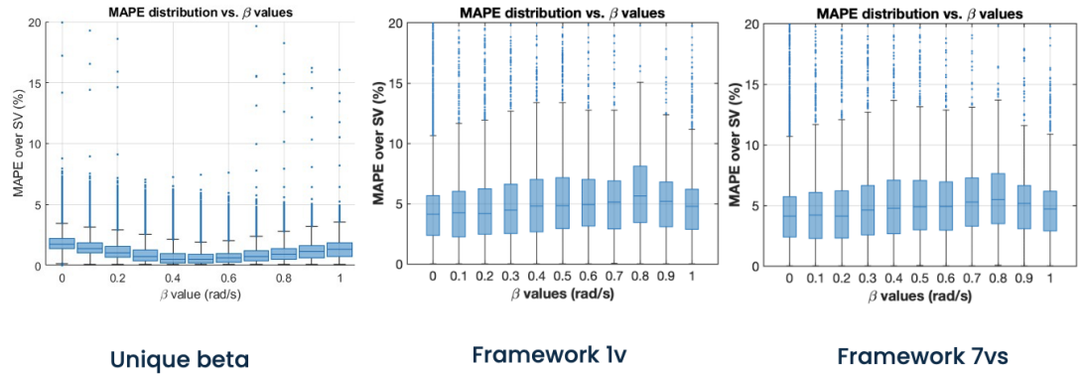

Fig. 4.54 This figure shows the error distributions obtained for SV using a single beta across the entire moderate-speed dataset (on the left) and with the framework with 1 variable (in the center) and 7 variables (on the right) when the objective function does not involve reference measurements.

Chapter 5

Discussion

This chapter discusses the results obtained during the development of the thesis, which were presented in Chapter 4. First, the results related to the tuning of the parameter characterizing the Madgwick algorithm will be analyzed, aiming to propose a single optimal value for both datasets under study and a range within which the results are speed, method, and hardware independent.
Subsequently, the results concerning the implemented optimization framework will be discussed, with the ultimate goal of proposing a new method for estimating spatio-temporal parameters that is fully automatic and does not require prior tuning.

5.1 Influence of Different Sensor Fusion Algorithms over Stride Length and Stride Velocity Estimates

Initially, the influence of different sensor fusion algorithms on SL and SV estimations was evaluated. This was done by tuning the key parameters of each algorithm across both datasets (as shown in Figures 4.1, 4.2, 4.3, and 4.4 for the slow-speed dataset, and Figures 4.7, 4.8, 4.9, and 4.10 for the moderate-speed dataset). The results showed that only the algorithm implemented by Madgwick [16] achieved a percentage error below 4 % for both metrics and across all datasets, within a very narrow range of values.
Furthermore, Madgwick's algorithm is the only one with a single parameter to be set, which represents an additional advantage. The presence of a single governing

parameter enhances the interpretability of the algorithm and simplifies the tuning process.
However, as observed in Figures 4.5, 4.6, 4.11, and 4.12, the Madgwick algorithm, similarly to all other tested algorithms (except for Valenti's), is highly sensitive to parameter selection, significantly affecting the estimations and, consequently, the errors. The influence of parameter variation was demonstrated by performing a statistical test on the distributions of SL and SV across different parameter values. Specifically, the Kruskal-Wallis test was used, as the obtained distributions were not normally distributed.
The results obtained led to the conclusion that, although MAD is highly sensitive to parameter selection, resulting in errors ranging from approximately 2% to a worst-case value of around 7% for SL, and from 3% up to about 13% in the worst-case scenario for SV, its ease of parameter tuning, combined with the lower errors compared to the other tested algorithms, makes it the most suitable choice for the application under study.
The Valenti algorithm was discarded because, despite its low sensitivity to parameter variation, it exhibited significantly higher errors than MAD and the other tested algorithms.
Once it was determined that MAD was the most suitable algorithm for orientation estimation in running applications, the optimal values were selected for each dataset. Subsequently, a sub-optimal trade-off value was chosen to ensure errors remained below 4% for each dataset. The results obtained are acceptable in terms of percentage error and allow for an accurate reconstruction of the foot trajectory, as observed in the various plots depicting the reconstructed three-dimensional displacement of the foot in Figures 4.25 and 4.26.
In addition to the analyses conducted using a single beta value for all the datasets under examination, the study was extended to propose a range of values that could be adapted to different speeds, hardware, and conditions. To this end, the tuning results from both datasets were combined, using the proposed method, which defines the initial instants with the TB method and the integration intervals with ZUPT, as well as the contact instants provided by the reference system (SP and PI), in order to minimize error propagation.
From the intersection of the obtained curves (Figures 4.13 and 4.17), two distinct intervals are identified, both yielding stride length errors below 4% and showing no speed dependency: 0.29–0.34 rad/s for the state-of-the-art pipeline and 0.5–0.65

rad/s for the pipeline implemented based on the reference intervals. By combining these six curves (Figure 4.18), an acceptability range (SL error below 4%) is obtained, spanning from 0.3 to 0.52 rad/s.

5.2 Performance of the Implemented Optimization Framework

Since the first part of the analysis confirmed that the proposed interval remains very narrow, given the significant influence of speed, conditions, and hardware on the estimates, and that a single parameter for an entire dataset may be insufficient due to the high variability of magneto-inertial signals, an alternative approach was considered. Specifically, a method was introduced to automatically select the parameter stride by stride, eliminating the need for specific tuning (dependent on reference measurements) and reducing dependency on speed and hardware.
A former analysis with the aim of verifying the feasibility of the method was conducted using firslty one only variable to optimize (the value of the β parameter) and then seven optimization variables with an objective function minimizing the errors over SL and SV. Naturally, this represents an optimal yet impractical condition, as the ultimate goal is to obtain accurate parameter estimates without relying on reference measurements. However, it is important to highlight that this approach introduces an innovative method, making feasibility verification a crucial step.
Results shown in Tables 4.8 and 4.9 and in Figures 5.1, 5.3, 5.2 and 5.4 demonstrate how the introduction of an optimization framework generally improve all the estimates. In particular, it was observed that for the slow-speed dataset, the estimates further improved when using a seven-variable framework (from 2.6 % at 8 km/h and 3.6 % at 10 km/h over SL to 0.9 % and from 0.8 % over SV for both speeds to 0.3 %). Conversely, for the moderate-speed dataset, introducing additional variables had no effect other than further increasing computational time.
However, those promising results refer only to error metrics. Therefore, the 3D foot displacement signal output was also considered to verify the reliability of the reconstruction. Indeed, as shown in Figures 4.27, 4.28, 4.31, 4.32, 4.35, 4.36, 4.41 and 4.42, the distribution of beta values appears homogeneous across subjects but is also widely spread across all admissible beta values.
As previously explained in Section 4.2.2, the signal reconstruction is generally ac-

curate for any chosen beta value, except in some cases where the anteroposterior component is highly precise, but the mediolateral and vertical components are incorrect. This mainly occurs because the objective function minimizes only errors, completely neglecting constraints related to the other components.
Finally, a preliminary test of the implemented framework with an objective function independent of reference measurements was conducted on both datasets, as this represents the final pipeline form to be proposed. The results, presented in Tables 4.10 and 4.11 and Figures 4.51,4.52, 4.53, and 4.54, show that, in general, the obtained errors are higher than those obtained using a single beta value for the entire dataset but remain comparable. These results should, of course, be considered as preliminary and require further improvements and refinements.

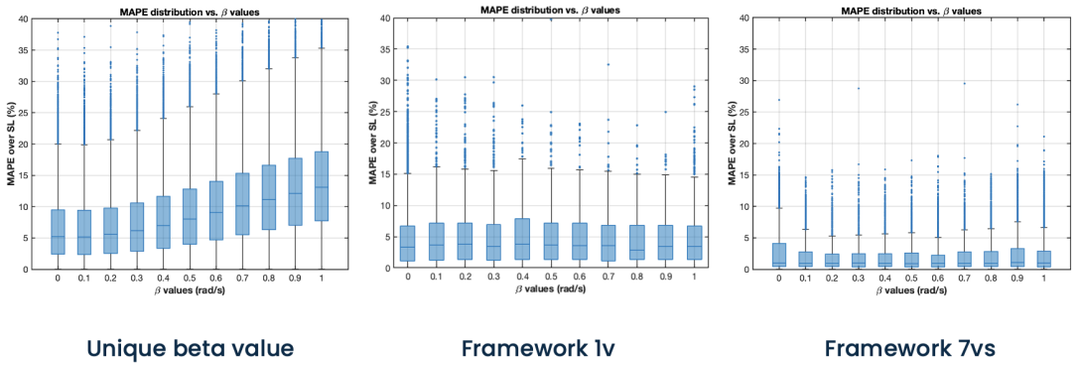

Fig. 5.1 This figure shows the error distributions obtained for SL using a single beta across the entire slow-speed dataset (on the left) and with the framework with 1 variable (in the center) and 7 variables (on the right).

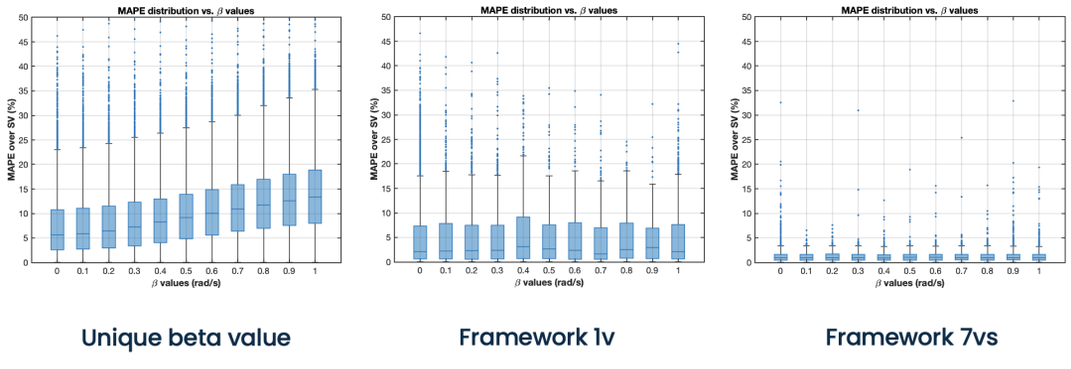

Fig. 5.2 This figure shows the error distributions obtained for SV using a single beta across the entire slow-speed dataset (on the left) and with the framework with 1 variable (in the center) and 7 variables (on the right).

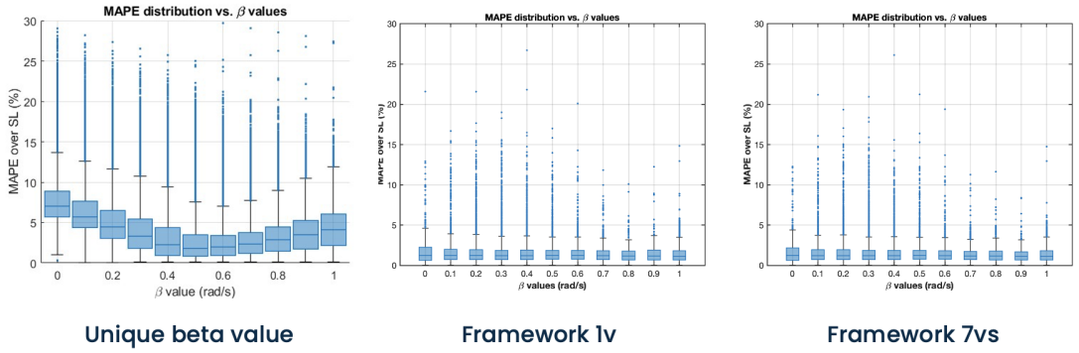

Fig. 5.3 This figure shows the error distributions obtained for SL using a single beta across the entire moderate-speed dataset (on the left) and with the framework with 1 variable (in the center) and 7 variables (on the right).

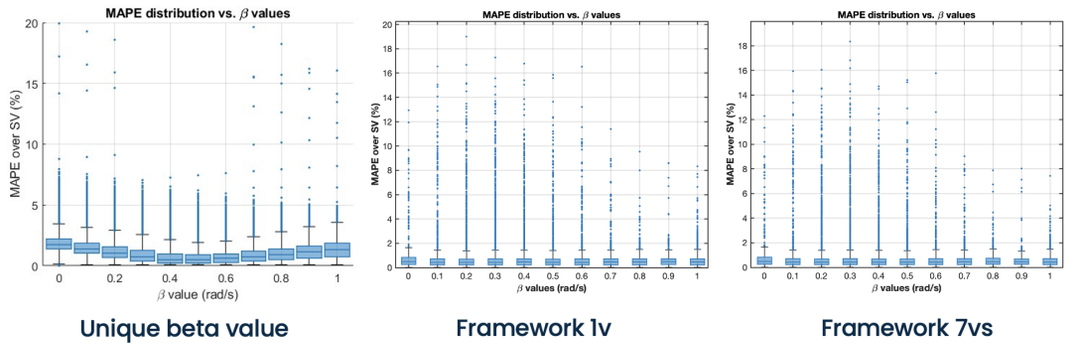

Fig. 5.4 This figure shows the error distributions obtained for SV using a single beta across the entire moderate-speed dataset (on the left) and with the framework with 1 variable (in the center) and 7 variables (on the right).

5.3 Final Comparison between State-of-The-Art Optimized Pipeline and Implemented Optimization Framework

At the conclusion of this work, it is essential to summarize the results obtained and discuss their implications to assess the validity of the method and potential future developments.

In the first part of the thesis, the effects of different orientation estimation algorithms on the spatiotemporal parameters of running were analyzed. Among the proposed

algorithms, MAD was identified as the most appropriate, as it not only delivers the best performance but also requires the definition of only one parameter. However, an incorrect setting of this parameter can lead to a significant increase in error, ranging from a minimum of approximately 2% to a maximum of 8%. This aspect is particularly critical, as selecting the optimal parameter value is a complex process and computationally expensive. Moreover, even when correctly chosen, the parameter was found to be speed-, hardware-, and method-dependent, making it difficult to define a universal value or range that could be used by third parties without the need for fine-tuning.

To address this limitation, the second phase of the thesis focused on introducing an innovative method capable of determining the parameter value stride-by-stride, making it independent of speed, hardware, and method, while also eliminating the need for an initial tuning phase. This approach yielded more accurate results, as shown in Tables 5.1, 5.2, and 5.3. In general, the best results were obtained by applying the seven-variable framework to both datasets. For this reason, this implementation is proposed as the most suitable for future developments.

However, one of the main limitations of the method is its computational cost. Specifically, computation time increases by approximately 15 times with the one-variable implementation and further triples with the seven-variable framework (Table 5.4). Although this increase is significant, it is important to note that the comparison does not take into account the fine-tuning phase required in the single-parameter β configuration. This phase is particularly lengthy and computationally expensive, as it requires multiple tests across the entire dataset to determine the optimal parameter value.

Moreover, regarding the implemented framework that does not rely on any reference data, the results can be considered promising. Not only is this a preliminary outcome, but it is also the only method among those presented that does not use reference measurements to select the parameter to be applied. In this case, the β values are chosen beforehand, and the reference measurements are used exclusively for computing the performance metrics.

Finally, Figure 5.5 provides a graphical comparison of the implemented and selected methods. Once again, it is evident that the 3D displacement reconstruction based on the framework sometimes introduces distortions in the medio-lateral (ML) and vertical (V) components of the signal. This issue highlights another key aspect that should be addressed in future developments of the method.

Table 5.1 Overall results for 8 km/h trials. All the results are proposed as mean value ± IQR.

	Optimal β value	**β trade-off**	**Framework 1v (GS)**	**Framework 7v (GS)**	**Framework 1v (no GS)**	**Framework 7v (no GS)**
MAPE SL (%)	1.9 ± 1.8	3.0 ± 1.4	2.6 ± 2.4	0.9 ± 0.3	5.1 ± 6.5	3.7±3.1
MAPE SV (%)	4.1 ± 1.9	7.1 ± 3.6	0.8 ± 0.6	0.2 ± 0.1	1.9 ± 2.4	1.1±0.9

Table 5.2 Overall results for 10 km/h trials. All the results are proposed as mean value ± IQR.

	Optimal β value	**β trade-off**	**Framework 1v (GS)**	**Framework 7v (GS)**	**Framework 1v (no GS)**	**Framework 7v (no GS)**
MAPE SL (%)	1.2 ± 0.7	2.6 ± 1.4	3.6 ± 4.3	0.9 ± 0.3	5.0±6.5	5.4±3.4
MAPE SV (%)	3.0 ± 0.9	2.5 ± 1.7	0.8 ± 0.4	0.3 ± 0.1	1.8±2.3	1.9±1.4

Table 5.3 Overall results for 14 km/h trials. All the results are proposed as mean value ± IQR.

	Optimal β value	**β trade-off**	**Framework 1v (GS)**	**Framework 7v (GS)**	**Framework 1v (no GS)**	**Framework 7v (no GS)**
MAPE SL (%)	2.5 ± 1.8	3.2 ± 1.5	1.6 ± 1.1	1.5 ± 0.5	4.7 ± 2.2	5.3 ± 2.5
MAPE SV (%)	2.6 ± 1.5	2.8 ± 2.1	0.8 ± 1.0	0.2 ± 0.1	4.0 ± 1.6	4.7 ± 2.3

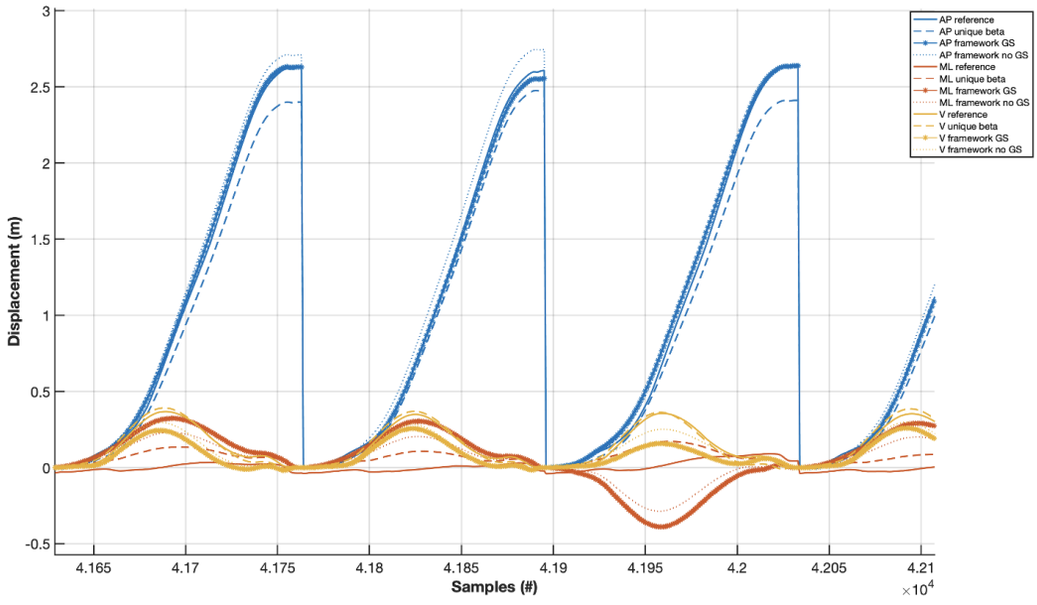

Fig. 5.5 Feasibility analysis of the implemented methods. Visual comparison of the reconstructed three-dimensional trajectory of the foot. The reconstruction from stereophotogrammetry is shown with a solid line, the reconstruction using a single beta with a dashed line, the reconstruction with the implemented framework using 7 variables and an objective function leveraging biomechanical constraints with a starred line, and the same framework with an objective function minimizing errors with a dotted line.

Dataset	**Computation time for 1 stride (s)**		
	Unique beta value	**Framework 1v**	**Framework 7vs**
8 km/h	0.020 ± 0.001	0.300 ± 0.100	1.180 ± 0.120
10 km/h	0.020 ± 0.001	0.300 ± 0.100	1.180 ± 0.120
14 km/h	0.020 ± 0.001	0.300 ± 0.100	0.960 ± 0.005

Table 5.4 Comparison of different computation times referring to the optimization of a single stride.

Chapter 6

Conclusions

The aim of this thesis was twofold. Firstly, to investigate whether it was possible to reduce errors in the computation of spatio-temporal parameters in running analysis by improving a state-of-the-art pipeline used to estimate foot displacement from MIMUs signals. This was achieved by selecting the optimal sensor fusion algorithm for orientation estimation and properly tuning it across different datasets. This step led to stride length estimation errors of 1.6% and 2.5%, and stride velocity errors of 3.5% and 2.6% for the slow-speed and moderate-speed datasets, respectively.
Secondly, an alternative method was explored to further improve these estimates. This was accomplished by implementing an optimization framework capable of defining the optimal governing parameters of the chosen sensor fusion algorithm (Madgwick et al. [16]) stride-by-stride, eliminating the need for a prior tuning phase. This novel approach showed promising results, achieving errors of 0.9% and 1.5% for stride length and 0.3% and 0.2% for stride velocity. However, these results were obtained using reference parameters derived from stereophotogrammetry and pressure insoles.
Further tests conducted without reference parameters yielded acceptable errors (equal to or below 6%), though there is still room for improvement. Future work should focus on refining the objective function by incorporating biomechanical constraints to develop a final method for running analysis that is personalized, speed-independent, and hardware-independent.
Moreover, to ensure the accurate reconstruction of the 3D displacement signal of the foot, it would be appropriate to include the medio-lateral and vertical components

within the objective function. This would allow for a precise reconstruction not only of the anteroposterior component but of the entire displacement signal.

References

[1] Sheila A Dugan and Krishna P Bhat. Biomechanics and analysis of running gait. *Physical Medicine and Rehabilitation Clinics*, 16(3):603–621, 2005.

[2] Thomas Stöggl and Tobias Wunsch. Biomechanics of marathon running. *Marathon running: Physiology, psychology, nutrition and training aspects*, pages 13–45, 2016.

[3] Lilifield Physio. Forefoot vs midfoot vs rearfoot running?, 2020. Accessed: 2024-11-11.

[4] Abhinandan Aggarwal, Rohit Gupta, and Ravinder Agarwal. Design and development of integrated insole system for gait analysis. In *2018 Eleventh International Conference on Contemporary Computing (IC3)*, pages 1–5. IEEE, 2018.

[5] STT Systems. 3dma - 3d optical motion capture and analysis, 2024. Accessed: 2024-11-25.

[6] Kathleen A Lamkin-Kennard and Marko B Popovic. Sensors: Naturaland synthetic sensors. *Biomechatronics*, pages 81–107, 2019.

[7] Treadmetrix. Single belt instrumented treadmill. Accessed: 20 November 2024.

[8] Giulia Pacini Panebianco, Maria Cristina Bisi, Rita Stagni, and Silvia Fantozzi. Analysis of the performance of 17 algorithms from a systematic review: Influence of sensor position, analysed variable and computational approach in gait timing estimation from imu measurements. *Gait & posture*, 66:76–82, 2018.

[9] Suresh Thenozhi, Wen Yu, and Ruben Garrido. A novel numerical integrator for structural control and monitoring. pages 680–686, 08 2012.

[10] Zakriya Mohammed, Ibrahim (Abe) Elfadel, and Mahmoud Rasras. Monolithic multi degree of freedom (mdof) capacitive mems accelerometers. *Micromachines*, 9:602, 11 2018.

[11] Waqas Amin Gill, Ian Howard, Ilyas Mazhar, and Kristoffer McKee. A review of mems vibrating gyroscopes and their reliability issues in harsh environments. *Sensors*, 22(19):7405, 2022.

[12] Vittorio MN Passaro, Antonello Cuccovillo, Lorenzo Vaiani, Martino De Carlo, and Carlo Edoardo Campanella. Gyroscope technology and applications: A review in the industrial perspective. *Sensors*, 17(10):2284, 2017.

[13] Parag Narkhede, Shashi Poddar, Rahee Walambe, George Ghinea, and Ketan Kotecha. Cascaded complementary filter architecture for sensor fusion in attitude estimation. *Sensors*, 21(6):1937, 2021.

[14] Yuren Chen, Xinyi Xie, Bo Yu, Yi Li, and Kunhui Lin. Multitarget vehicle tracking and motion state estimation using a novel driving environment perception system of intelligent vehicles. *Journal of advanced transportation*, 2021(1):6251399, 2021.

[15] Francesca Salis, S Bertuletti, T Bonci, U Della Croce, C Mazzà, and A Cereatti. A method for gait events detection based on low spatial resolution pressure insoles data. *Journal of Biomechanics*, 127:110687, 2021.

[16] Sebastian Madgwick et al. An efficient orientation filter for inertial and inertial/magnetic sensor arrays. *Report x-io and University of Bristol (UK)*, 25:113–118, 2010.

[17] Roberto G Valenti, Ivan Dryanovski, and Jizhong Xiao. Keeping a good attitude: A quaternion-based orientation filter for imus and margs. *Sensors*, 15(8):19302–19330, 2015.

[18] Thomas Seel and Stefan Ruppin. Eliminating the effect of magnetic disturbances on the inclination estimates of inertial sensors. *IFAC-PapersOnLine*, 50(1):8798–8803, 2017.

[19] Marco Caruso, Angelo Maria Sabatini, Marco Knaflitz, Marco Gazzoni, Ugo Della Croce, and Andrea Cereatti. Orientation estimation through magneto-inertial sensor fusion: A heuristic approach for suboptimal parameters tuning. *IEEE Sensors Journal*, 21(3):3408–3419, 2020.

[20] Napier Chris. *Scienza della corsa: Migliorare la tecnica e l'allenamento, prevenire gli infortuni*. Gribaudo, 2020.

[21] Duck-chul Lee, Angelique G Brellenthin, Paul D Thompson, Xuemei Sui, I-Min Lee, and Carl J Lavie. Running as a key lifestyle medicine for longevity. *Progress in cardiovascular diseases*, 60(1):45–55, 2017.

[22] Valentina Camomilla, Elena Bergamini, Silvia Fantozzi, and Giuseppe Vannozzi. Trends supporting the in-field use of wearable inertial sensors for sport performance evaluation: A systematic review. *Sensors*, 18(3):873, 2018.

[23] Gian Luigi Canata, Henrique Jones, Werner Krutsch, Patricia Thoreux, and Alberto Vascellari. The running athlete: A comprehensive overview of running in different sports. 2022.

[24] Roger A Mann, Donald E Baxter, and Lowell D Lutter. Running symposium. *Foot & ankle*, 1(4):190–224, 1981.

[25] Tom F Novacheck. The biomechanics of running. *Gait & posture*, 7(1):77–95, 1998.

[26] Rachel Mason, Liam T Pearson, Gillian Barry, Fraser Young, Oisin Lennon, Alan Godfrey, and Samuel Stuart. Wearables for running gait analysis: A systematic review. *Sports Medicine*, 53(1):241–268, 2023.

[27] Eline Van der Kruk and Marco M Reijne. Accuracy of human motion capture systems for sport applications; state-of-the-art review. *European journal of sport science*, 18(6):806–819, 2018.

[28] Logan Wade, Laurie Needham, Polly McGuigan, and James Bilzon. Applications and limitations of current markerless motion capture methods for clinical gait biomechanics. *PeerJ*, 10:e12995, 2022.

[29] Lizeth H Sloot, MM Van der Krogt, and Jaap Harlaar. Self-paced versus fixed speed treadmill walking. *Gait & posture*, 39(1):478–484, 2014.

[30] F Alton, L Baldey, S Caplan, and MC Morrissey. A kinematic comparison of overground and treadmill walking. *Clinical biomechanics*, 13(6):434–440, 1998.

[31] Brian K Higginson. Methods of running gait analysis. *Current sports medicine reports*, 8(3):136–141, 2009.

[32] Arslan Ahmad, Muhammad Ibraheem, Mohsin Ahsen, Khawar Shah, and Umer Shahid. Design and implementation of robotic arm that copies the human arm. 2017.

[33] Elena Martini, Tommaso Fiumalbi, Filippo Dell'Agnello, Zoran Ivanić, Marko Munih, Nicola Vitiello, and Simona Crea. Pressure-sensitive insoles for real-time gait-related applications. *Sensors*, 20(5), 2020.

[34] Abdul Hadi Abdul Razak, Aladin Zayegh, Rezaul K Begg, and Yufridin Wahab. Foot plantar pressure measurement system: A review. *Sensors*, 12(7):9884–9912, 2012.

[35] Zoran Djurić. Mechanisms of noise sources in microelectromechanical systems. *Microelectronics Reliability*, 40(6):919–932, 2000.

[36] Marco Caruso, Angelo Maria Sabatini, Daniel Laidig, Thomas Seel, Marco Knaflitz, Ugo Della Croce, and Andrea Cereatti. Analysis of the accuracy of ten algorithms for orientation estimation using inertial and magnetic sensing under optimal conditions: One size does not fit all. *Sensors*, 21(7):2543, 2021.

[37] Tariqul Islam, Md Saiful Islam, Md Shajid-Ul-Mahmud, et al. Comparison of complementary and kalman filter based data fusion for attitude heading reference system. In *AIP Conference Proceedings*, volume 1919. AIP Publishing, 2017.

[38] Jack B Kuipers. *Quaternions and rotation sequences: a primer with applications to orbits, aerospace, and virtual reality*. Princeton university press, 1999.

[39] James Diebel et al. Representing attitude: Euler angles, unit quaternions, and rotation vectors. *Matrix*, 58(15-16):1–35, 2006.

[40] Zheming Wu, Zhenguo Sun, Wenzeng Zhang, and Qiang Chen. Attitude and gyro bias estimation by the rotation of an inertial measurement unit. *Measurement Science and Technology*, 26(12):125102, oct 2015.

[41] Walter Stockwell. Angle random walk. *Application Note. Crossbow Technologies Inc*, pages 1–4, 2003.

[42] Rudolph Emil Kalman. A new approach to linear filtering and prediction problems. 1960.

[43] Dan Simon. Kalman filtering. *Embedded systems programming*, 14(6):72–79, 2001.

[44] Maria Isabel Ribeiro. Kalman and extended kalman filters: Concept, derivation and properties. *Institute for Systems and Robotics*, 43(46):3736–3741, 2004.

[45] Elena Bergamini, Gabriele Ligorio, Aurora Summa, Giuseppe Vannozzi, Aurelio Cappozzo, and Angelo Maria Sabatini. Estimating orientation using magnetic and inertial sensors and different sensor fusion approaches: Accuracy assessment in manual and locomotion tasks. *Sensors*, 14(10):18625–18649, 2014.

[46] Isaac Skog, John-Olof Nilsson, and Peter Händel. Evaluation of zero-velocity detectors for foot-mounted inertial navigation systems. In *2010 International Conference on indoor positioning and indoor navigation*, pages 1–6. IEEE, 2010.

[47] Angelo M Sabatini. Quaternion-based extended kalman filter for determining orientation by inertial and magnetic sensing. *IEEE transactions on Biomedical Engineering*, 53(7):1346–1356, 2006.

[48] Markus Zrenner, Stefan Gradl, Ulf Jensen, Martin Ullrich, and Bjoern M Eskofier. Comparison of different algorithms for calculating velocity and stride length in running using inertial measurement units. *Sensors*, 18(12):4194, 2018.

[49] Beatrice Utzeri. Analysis of spatio-temporal parameters during running at different speeds using foot-mounted magneto-inertial sensors. Master's thesis, Politecnico di Torino, 2023.

[50] GP Bailey and R Harle. Assessment of foot kinematics during steady state running using a foot-mounted imu. *Procedia Engineering*, 72:32–37, 2014.

[51] Mounir Zok, Claudia Mazzà, and Ugo Della Croce. Total body centre of mass displacement estimated using ground reactions during transitory motor tasks: Application to step ascent. *Medical engineering & physics*, 26(9):791–798, 2004.

[52] Rachele Rossanigo. Development of methods for the evaluation of mobility and physical activity through wearable sensors. 2024.

[53] Francesca Salis, Stefano Bertuletti, Kirsty Scott, Marco Caruso, Tecla Bonci, E Buckley, Ugo Della Croce, Claudia Mazzà, and Andrea Cereatti. A wearable multi-sensor system for real world gait analysis. In *2021 43rd Annual International Conference of the IEEE Engineering in Medicine & Biology Society (EMBC)*, pages 7020–7023. IEEE, 2021.

[54] OPAL. *Mobility Lab User Guide*, 2020.

[55] Rachele Rossanigo, Marco Caruso, Elena Dipalma, Cristine Agresta, Lucia Ventura, Franca Deriu, Andrea Manca, Taian M Vieira, Valentina Camomilla, and Andrea Cereatti. A speed-invariant template-based approach for estimating running temporal parameters using inertial sensors. *IEEE Access*, 2025.

[56] Proceedings xxiii congresso siamoc 2023. Atti di convegno, Roma, 2023.

[57] Rachele Rossanigo, Marco Caruso, Francesca Salis, Stefano Bertuletti, Ugo Della Croce, and Andrea Cereatti. An optimal procedure for stride length estimation using foot-mounted magneto-inertial measurement units. In *2021 IEEE International Symposium on medical measurements and applications (MeMeA)*, pages 1–6. IEEE, 2021.

[58] Robert Mahony, Tarek Hamel, and Jean-Michel Pflimlin. Nonlinear complementary filters on the special orthogonal group. *IEEE Transactions on automatic control*, 53(5):1203–1218, 2008.

[59] Siwen Guo, Jin Wu, Zuocai Wang, and Jide Qian. Novel marg-sensor orientation estimation algorithm using fast kalman filter. *Journal of Sensors*, 2017(1):8542153, 2017.

[60] Angelo Maria Sabatini. Estimating three-dimensional orientation of human body parts by inertial/magnetic sensing. *Sensors*, 11(2):1489–1525, 2011.

[61] Gabriele Ligorio and Angelo M Sabatini. A novel kalman filter for human motion tracking with an inertial-based dynamic inclinometer. *IEEE Transactions on Biomedical Engineering*, 62(8):2033–2043, 2015.

[62] Roberto G Valenti, Ivan Dryanovski, and Jizhong Xiao. A linear kalman filter for marg orientation estimation using the algebraic quaternion algorithm. *IEEE Transactions on Instrumentation and Measurement*, 65(2):467–481, 2015.

[63] Verena Elisabeth Kremer. Quaternions and slerp. In *Embots. dfki. de/doc/seminar ca/Kremer Quaternions. pdf*, 2008.

[64] Jorge Nocedal and Stephen J Wright. *Numerical optimization*. Springer, 1999.

[65] Samira Francesca. *Analyzing human lower limb kinematics during walking: a challenging study with minimal inertial sensor configuration*. PhD thesis, Politecnico di Torino, 2023.

[66] A Machetti, R Rossanigo, M Caruso, G Martinez, L Ventura, A Manca, F Deriu, and A Cereatti. Comparison of inertial-based filters for orientation estimation in indoor and outdoor running. *Gait & Posture*, 114:S28–S29, 2024.

[67] Daniel Parker, Jennifer Andrews, and Carina Price. Validity and reliability of the xsensor in-shoe pressure measurement system. *PloS one*, 18(1):e0277971, 2023.

[68] APDM Wearable Technologies. *MobilityLab v1 User Guide*, 2025. Accessed: 2025-01-03.

[69] R MARGARIA, P AGHEMO, and E ROVELLI. La lunghezza dei passi in funzione della velocita nella marcia e nella corsa. *ATTI DELLA ACCADEMIA NAZIONALE DEI LINCEI RENDICONTI-CLASSE DI SCIENZE FISICHE-MATEMATICHE & NATURALI*, 40(2):194, 1966.

Appendix A

Preliminary results of running analysis in running-related sports: insights from instrumented softball players

The primary objective of extending the optimized pipelines developed in the thesis project is to broaden their application beyond level running in standardized environments with gold-standard references.
The aim would be to study not only level running in standardized environments, but also non-constrained settings for different applications, such as analysis during running competitions for elite and amateur runners and analysis in other running-related sports.
A preliminary running analysis on softball players has been conducted concurrently with the development of the optimization framework presented in Chapter 3 and is briefly discussed below.

A.1 Dataset presentation

Several training sessions of the University of Washington's softball team (Washington Huskies) and a full game were recorded with inertial sensors placed on the dorsum

of the shoes and on the lower back along with X-sensors in-shoes pressures sensors with a sampling frequency of 100 Hz [67]. Between 1 and 4 players were equipped with sensors in each session. The placement of the sensors is depicted in Figures A.1 and A.2.

The inertial units used are OPAL MIMUs sensors, with an accelerometer range of $\pm 16\,g$, gyroscope range up to $\pm 2000^\circ/\mathrm{s}$, a magnetometer range of ± 8 Gauss, and a sampling frequency of 250 Hz [68].

Furthermore, every session was filmed with GoPro cameras (sampling rate of 30 Hz), positioned above home plate, first base and third base. The view from the camera above the home plate is shown in Figure A.3.

Fig. A.1 MIMUs placement on shoes dorsum, under the white tape; the black support refers to the pressure insole system.

Fig. A.2 MIMU placement on the lower back, under the white tape.

Fig. A.3 Home plate view from the camera used to record the analyzed session.

A.2 Analysis

Before proceeding with the gestures analysis of interest, it was necessary to synchronize the videos with the signals obtained from OPAL.
Specifically, each subject was ordered to spin around their vertical axis (performing one or more rotations depending on the session) following and preceding a standing phase; this movements combination is easily identifiable on the gyroscope signal (Figure A.4). Once the sequence was located on the signal, the starting point of the video could be accurately aligned with the signal.
After temporally synchronizing the video and signal, the analysis of the running trials could commence.
The gestures in the segmented videos were different between them, covering each stage of the game; some involved hitting the ball, some running from one base to another and others the rescue of the ball from the players in defense position.
For the thesis project, this preliminary analysis focuses exclusively on the runs between different bases. For clarity, Figure A.5 provides a schematic representation of a softball field, highlighting the locations of the bases.
The analysis was conducted using the grid search method optimized pipeline presented in Chapter 3. As a consequence of the observations conducted in this work,

the selected SFA for orientation estimation is MAD [16], with a β value of 0.51 rad/s. The choice of the same β value as that of the dataset at 14 km/h was dictated by the fact that the speed reached during the softball game is higher than the velocities analyzed in the datasets of this thesis. We selected the β value that optimized SL estimates in the dataset with the highest speed, rather than a trade-off value.
Furthermore, after verifying the absence of ferromagnetic disturbances in the signals, it is important to note that, unlike the dataset at 14 km/h, the magnetometer was used to determine the orientation of the sensor.

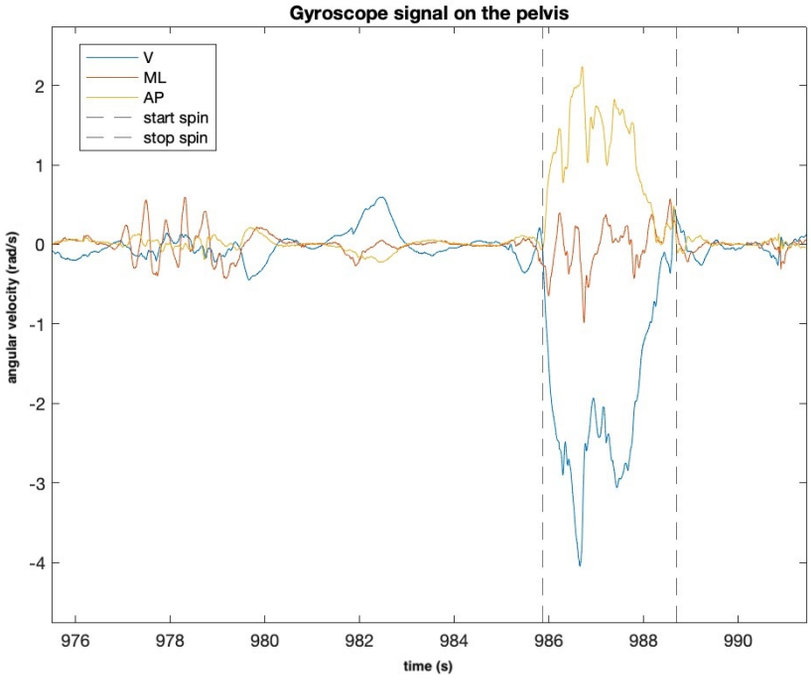

Fig. A.4 Spin detection on the gyroscope signal of a subject for a session; the spin is located between two short standing phases and is characterized by a major prominence in rotation around the vertical axis.

A.3 Results and Discussion

Nine trials were analyzed: three involved running from home plate to first base, while six focused on running from first base to second base. For each trial, strides from both feet were considered, resulting in a total of 116 strides analyzed.
Each trial was processed to calculate velocity and displacement estimates stride by

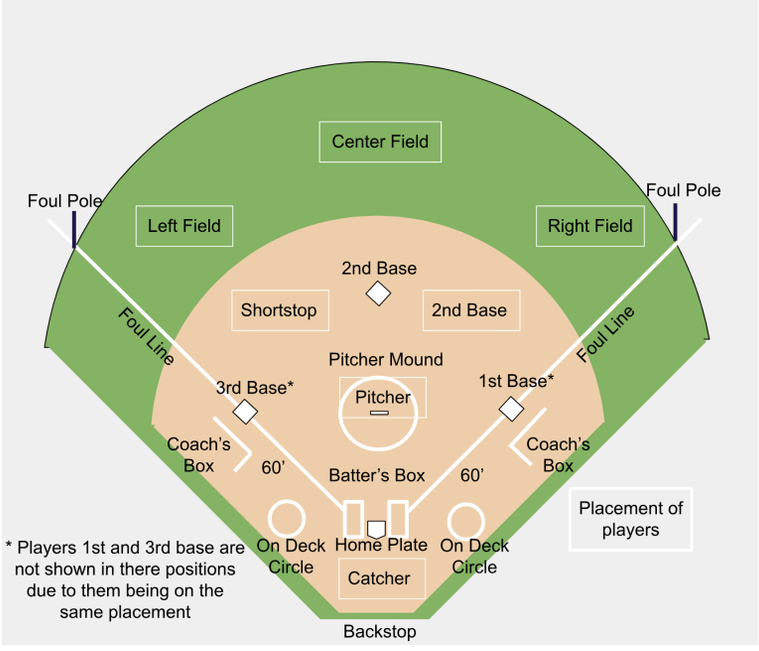

Fig. A.5 Schematic representation of positionings and players in the softball games, from *Wikimedia Commons* (https://commons.wikimedia.org/wiki/File:Softball_Diagram_with_Players_Placement.svg).

stride in every direction (AP, ML,V). Furthermore, we calculated Stride Lengths and Stride Velocities as presented in Section 2.5; however, the absence of reference measurements made it impossible to computate error metrics.

Nevertheless, the use of videos as a reference enabled a qualitative evaluation of velocities and displacements for each trial.

Generally, each run between two bases is characterized by an initial phase of acceleration followed by a deceleration phase near the approaching base. This results in an increase in speed, followed by a rapid decrease; the same pattern is observed for stride lengths (SLs) [69].

All analyzed trials confirmed this trend for both velocity and displacement reconstructions in the direction of progression. Results for a trial on the left foot are shown in Figures A.6 and A.7.

These results, though preliminary, show that running analysis can be interestingly used also in running-related sports. Signals from MIMUs can be used also for other analysis and this can be an important application, both for elite and amateur players.

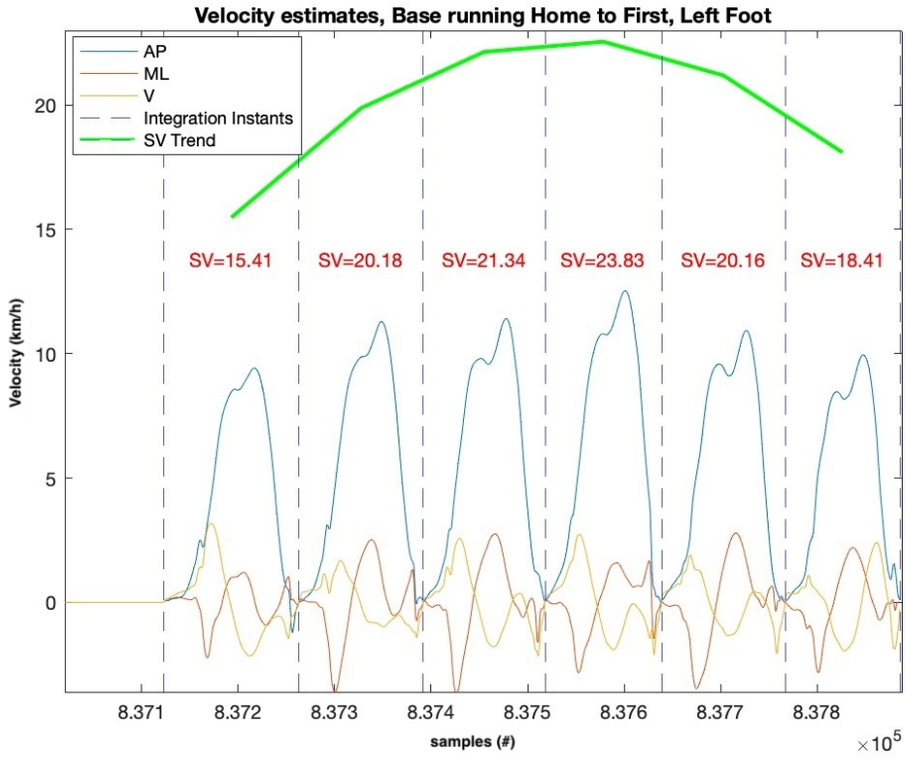

Fig. A.6 Velocity Estimates for a trial, left foot; defined by 6 strides. The trend line (green line) shows that the SV increases to a peak and then decreases.

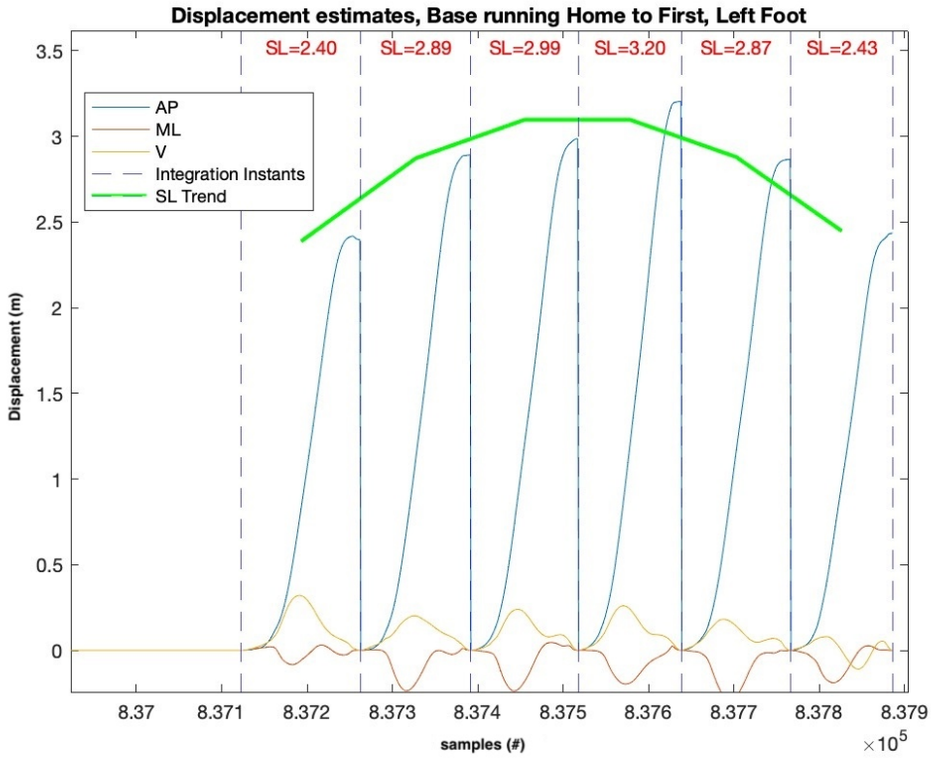

Fig. A.7 Displacement Estimates for a trial, left foot; defined by 6 strides. The trend line (green line) shows that the SL increases to a peak and then decreases.